

Doctoral Dissertation

(Shinshu University)

Negativity and its capacity
in Jackiw-Teitelboim gravity

March, 2025

Department of Science and Technology,
Materials Science and Engineering Division

Takeshi Tachibana

Abstract

In this thesis, we explore some aspects of quantum entanglement in quantum gravity. In particular, we investigate the refined Rényi negativity in Jackiw-Teitelboim (JT) gravity. The refined Rényi negativity is a one-parameter generalization of the entanglement negativity which is a measure of entanglement in general mixed states. The parameter introduced is called the replica number. JT gravity is a two-dimensional toy model of quantum gravity and is described by a certain double-scaled random matrix model. Several types of “replica wormholes” contribute to the refined Rényi negativity, which plays the essential role in our study.

The aim of our work is to provide a deeper understanding of the entanglement structure of the Hawking radiation. To this end, we consider the matrix model of JT gravity with dynamical branes, which serves as a toy model of an evaporating black hole. We identify the degrees of freedom of the Hawking radiation with the branes in this model. The model provides an effective method to investigate the back-reaction of the Hawking radiation. The replica wormholes appear as the connected parts of the ensemble average of the matrix integral. We compute the refined Rényi negativity for a bipartite system of the Hawking radiation.

We find that the refined Rényi negativity monotonically decreases due to the back-reaction at late time of the black hole evaporation. The decreasing behavior is understood in the same way as the “Page curve” of the entanglement entropy. Moreover, we define a novel quantity which we call “capacity of negativity,” as a derivative of the refined Rényi negativity with respect to the replica number. We find that the capacity of negativity exhibits two peaks as a function of time. The peaks indicate the phase transitions of the entanglement structure of the Hawking radiation, which comes from the exchange of dominance of different types of replica wormholes.

Acknowledgements

First I am sincerely grateful to Kazumi Okuyama for his invaluable guidance during my time at Shinshu university. He taught me a lot not only on physics but also on the attitude to work on physics. He is the best adviser I could have asked for.

I would like to thank my other teachers. I learned a lot on physics and mathematics from Satoru Otake and Yoshiharu Kawamura in the theoretical particle physics group. I also thank Kazuhiko Takano for his advices and encouragement in the seminars on geometry for general relativity.

I am especially thankful to Tatsuma Nishioka for correspondence. He kindly provided his Mathematica file on the capacity of entanglement. I also thank Tomonori Ugajin for his lectures on the recent progress in the black hole information paradox at Nagoya university in 2022.

This work was supported by JST SPRING, Grant Number JPMJSP2144 (Shinshu University). I am thankful to the financial support and opportunities to interact with other doctoral students. I am especially thankful to Yasuhide Yoshitake for his encouragement at Shinshu Tamonjuku.

I would like to thank my friends at Shinshu university and other institutes including Hiroki Mizuno, Qiran Zhang, Wakano Sakamoto, Eiji Kodaira, Yasunari Nishikawa, Takuya Okada, Kentaro Koizumi, Kaito Nagatomo, Norihisa Shimizu, Akihisa Takamatsu, Ryusuke Aida, Harukaze Matsuzawa, Shintaro Nagase, Yusuke Taki, Taishi Kawamoto, Yu-ki Suzuki, Masataka Watanabe, Masamichi Miyaji, and Marcelo Oyarzo. They were always very warm towards me and I spent invaluable time with them. I learned a lot on topology from Hiroki Mizuno, and it was a great fun of me.

Finally, I would like to thank my family, Satoshi, Kazumi, Hajime, Tsutomu, and Kanoko Tachibana for their support to keep my life in Kyoto and Shinshu. I also thank all people who have supported me until today.

Contents

1	Introduction	5
2	Matrix model of JT gravity	12
2.1	JT gravity and random matrix	13
2.1.1	Path integral of JT gravity	13
2.1.2	Random matrix model	20
2.2	Two-dimensional topological gravity	25
2.2.1	JT gravity as a topological gravity	25
2.2.2	Generalized partition function	28
2.2.3	Leading order eigenvalue density	30
2.3	JT gravity with dynamical branes	33
2.3.1	Correlator with FZZT anti-branes	33
2.3.2	Back-reaction of branes	36
3	Black hole information paradox	40
3.1	PSSY model	42
3.1.1	Semiclassical description	42
3.1.2	Matrix model description	48
3.1.3	Resolvent trick	52
3.1.4	Entanglement spectrum	54
3.2	Page curve from dynamical branes	55
3.2.1	Matrix integral with FZZT anti-branes	56
3.2.2	Analytic proof of monotonicity	58
4	Negativity in JT gravity	61
4.1	Basics of entanglement negativity	62
4.1.1	Partial transpose	62

4.1.2	Rényi generalization	63
4.2	Negativity spectrum in JT gravity	65
4.2.1	Dominant saddles	66
4.2.2	Ensemble average	70
4.2.3	Resolvent trick	73
4.2.4	Negativity spectrum	76
4.3	Refined Rényi negativity	78
4.4	Capacity of negativity	80
4.4.1	Microcanonical ensemble	81
4.4.2	Capacity of negativity	83
5	Discussion	86
	Bibliography	89

Chapter 1

Introduction

In this chapter, we explain the backgrounds of our work and give a brief summary of this thesis. Our work is motivated by the recent progress in the black hole information paradox and quantum gravity. In this thesis, we particularly focus on the applications of the matrix model of JT gravity to the black hole information paradox.

The black hole information paradox is a long-standing puzzle whether the time evolution of black holes is unitary or not. Such a problem arises when we consider the black holes with quantum effects, namely the Hawking radiation. The information paradox is formulated by calculating the entanglement entropy of the Hawking radiation. Recently, the information paradox is partially resolved by applying novel computational methods developed in the study of quantum gravity. The new findings include some important ingredients such as “island” and “replica wormholes.” In particular, the replica wormholes play the essential roles in our study.

On the other hand, JT gravity is a two-dimensional toy model of quantum gravity. Recently, the matrix model description of JT gravity was discovered and has been applied to many important problems in quantum gravity, such as the quantum chaos, the factorization problem, and the black hole information paradox. Our work is based on the recent developments of the matrix model of JT gravity. Namely, the aspect of JT gravity as a specific example of the two-dimensional topological gravity is essential.

Black hole information paradox

We first review the recent progress in the black hole information paradox. See also [1] for a recent review and for further references. Black holes are extremely massive objects and thought to be formed by the gravitational collapse of massive stars [2]. Classically, black holes can only gain their masses and the area of the event horizon can only increase [3]. However, black holes lose their masses by emitting thermal radiation and will finally evaporate out if we consider the quantum effects of matter on the classical black hole background. This effect is called the Hawking radiation [4]. The Hawking radiation consists of entangled pairs of particles, one of the pair goes inside the black hole while the other escapes to infinity. If the black hole completely evaporates, only the Hawking radiation outside the black hole will remain. We show a schematic picture of the process of the black hole evaporation in Figure 1.1.

Hawking [5] pointed out the possibility that the black hole evaporation would violate the unitarity. This is the original black hole information paradox. If the time evolution is unitary, an initial pure state must evolve to a final pure state. However, the final state of the black hole seems to be a thermal mixed state even though we start from an initial pure state. The paradox is formulated by calculating the entanglement entropy of the Hawking radiation. Hawking expected that the entanglement entropy of the Hawking radiation keeps growing until the black hole completely evaporates out (shown as the green curve in Figure 1.2). This calculation indicates that the final state of the total system is the thermal mixed state. Thus, the black hole evaporation seems to violate the unitarity.

Page [6, 7] found a necessary condition for the time evolution of black holes to be unitary. He found that the entanglement entropy follows the “Page curve” as a function of time if the time evolution of black holes is unitary. The entanglement entropy first increases and turns to decrease at a time called the “Page time” (shown as the blue curve in Figure 1.2). As seen from Figure 1.2, the entanglement entropy is bounded by the thermodynamic entropy of the black hole after the Page time. The thermodynamic entropy is called the Bekenstein-Hawking entropy [8] which is proportional to the area of the event horizon of the black hole. The late time decreasing behavior comes from the decreasing area of the event horizon as the black hole evaporates

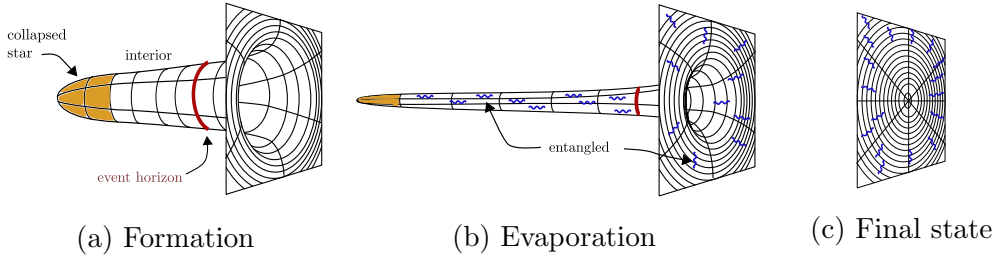


Figure 1.1: Schematic picture of black hole evaporation [1]. (a) Black hole is formed by gravitational collapse. (b) Black hole creates entangled pairs of particles. (c) Black hole evaporates out and Hawking radiation remains.

by emitting the Hawking radiation. This effect is called the “back-reaction” of the Hawking radiation. However, Page’s discussion was limited in a non-gravitational toy model which approximates the state of the total system by a random pure state. How to obtain the Page curve in gravitating systems has been a long-standing problem.

Island formula and replica wormholes

The recent studies revealed how to calculate the entanglement entropy following the Page curve in semiclassically gravitating systems. The entanglement entropy of the Hawking radiation at a constant time can be calculated by the following “island formula” [9, 10, 11]

$$S = \min_I \left\{ \text{ext}_I \left[\frac{A(\partial I)}{4G_N} + S_{\text{matter}}(I \cup R) \right] \right\}, \quad (1.1)$$

where I and R are subregions of the Cauchy surface at the time. The region I is called the “island” which locates inside the black hole. The region R is the “radiation” region where we collect the Hawking radiation outside the black hole. The first term comes from the area of the codimension-two surface which is the boundary of the island I . The second term comes from the Hawking radiation in the region $I \cup R$. From the island formula (1.1), the Page curve is reproduced as follows: (i) there is no island contribution at early time, and the entanglement entropy is just given by the contribution from the increasing Hawking radiation in the region R , (ii) the island covers a large region inside the black hole at late time, and the first term approaches the Bekenstein-Hawking entropy while the second term goes to zero. The

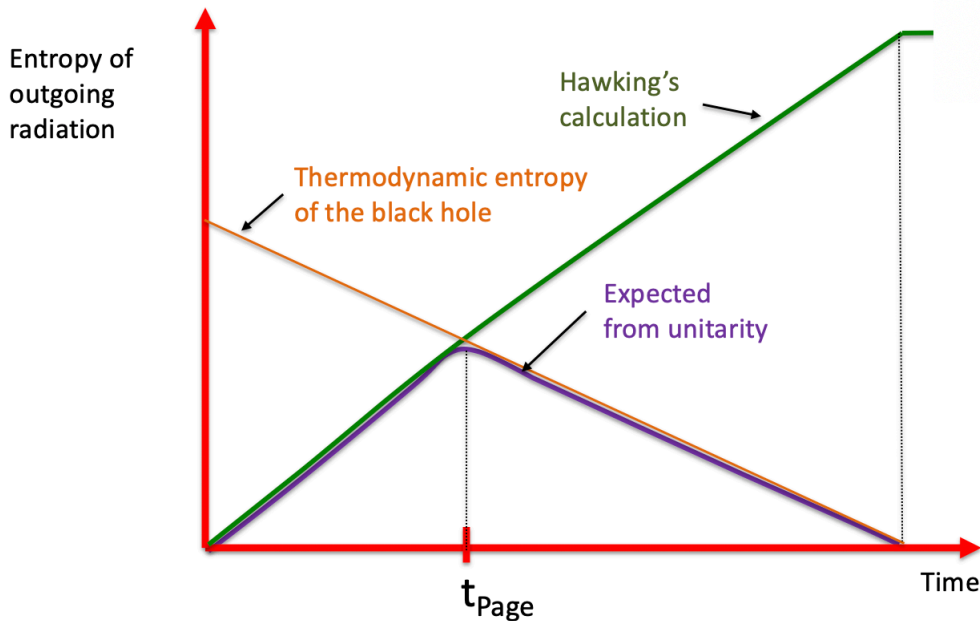


Figure 1.2: A schematic picture of the Page curve [1]. If the time evolution of the black hole is unitary, the entanglement entropy of the Hawking radiation follows the Page curve described by the blue curve in the figure.

second term goes to zero at late time since the Hawking radiation in R is purified by the interior partner in I . The island formula is developed in recent study of quantum gravity, in particular the AdS/CFT correspondence.

The recent studies also revealed the connection between the spacetime topology and the quantum entanglement. The island formula can be obtained by using the replica trick in gravitational systems [12]. It was found that geometric objects called the “replica wormholes” play the essential role to obtain the island formula [13, 14]. The replica trick is a trick to calculate the entanglement entropy by preparing the copies of the original system. The replica wormholes are geometric objects connecting the different copies. They appear as the nontrivial saddles in the gravitational path integral. The transition of the Page curve can be understood by the exchange of dominance between the different types of replica wormholes. The “disconnected” saddle dominates before the Page time while the “connected” one dominates after the Page time. These two saddles are invariant under the exchange of the replicas. This symmetry is called the replica symmetry.

This thesis

In this thesis, we investigate the entanglement negativity in a toy model of an evaporating black hole. It was found by Dong, McBride, and Weng [15] that the entanglement negativity can probe more elaborate entanglement structure of the Hawking radiation than the entanglement entropy. Interestingly, certain replica wormholes which break the replica symmetry can dominate in the calculation of the entanglement negativity. The dominant replica wormhole corresponds to a certain phase of the entanglement structure of the Hawking radiation. The aim of our work is to refine the previous work and provide a deeper understanding of the relation between the replica wormholes and the entanglement structure of the Hawking radiation.

In particular, we explore the refined Rényi negativity which is a one-parameter generalization of the entanglement negativity. The parameter introduced is called the replica number. We find that the refined Rényi negativity monotonically decreases at late time of the black hole evaporation. This decreasing behavior is similar to the decreasing behavior of the Page curve. Moreover, we define a novel quantity which we call “capacity of negativity” as a derivative of the refined Rényi negativity with respect to the replica number. We find that the capacity of negativity exhibits two peaks as a function of time, which comes from the exchange of dominance of different types of replica wormholes. Thus, the capacity of negativity is a valuable indicator of the phase transitions of the entanglement structure.

Summary and organization

In this section, we give a brief summary of the remainder of this thesis.

Chapter 2

We review the random matrix model of JT gravity [16] and its extension [17] with dynamical Fateev-Zamolodchikov-Zamolodchikov-Teschner (FZZT) anti-branes [18, 19]. The aim of this chapter is to obtain the leading eigenvalue density $\rho_0(E)$ of the matrix model, which is deformed from the original one by the insertion of the FZZT anti-branes. We call this effect the “back-reaction of branes.” The eigenvalue density $\rho_0(E)$ is related to the partition

function $Z(\beta)$ of JT gravity by the following Laplace transformation

$$Z(\beta) = \int_{E_0}^{\infty} dE e^{-\beta E} \rho_0(E), \quad (1.2)$$

where E_0 is the minimal energy such that $\rho_0(E)$ is supported for $E \geq E_0$. As we will review in section 2.2, JT gravity is a kind of two-dimensional topological gravity which is described by a certain double-scaled random matrix model with infinitely many couplings $\{t_k\}$. One can compute $Z(\beta)$ from a generating function $F(\{t_k\})$ defined in the topological gravity. In this formalism, adding FZZT anti-branes amounts to the shift of the couplings $\{t_k\}$ in (2.124), and one can compute $Z(\beta)$ from $F(\{t_k\})$ with the resulting couplings. Finally, $\rho_0(E)$ is given by the following expression:

$$\rho_0(E) = \frac{1}{\sqrt{2\pi g_s}} \left(\int_{E_0}^E dv \frac{I_0(2\sqrt{v})}{\sqrt{E-v}} - \frac{t}{E+\xi} \sqrt{\frac{E-E_0}{2(E_0+\xi)}} \right), \quad (1.3)$$

where t denotes the 't Hooft coupling which is proportional to the number of branes. It reduces to the original eigenvalue density $\rho_0^{\text{JT}}(E)$ by setting $t = 0$,

$$\rho_0^{\text{JT}}(E) = \frac{\sinh(2\sqrt{E})}{\sqrt{2\pi g_s}}. \quad (1.4)$$

In chapter 3 and 4, we investigate the back-reaction effects to the entanglement entropy and the refined Rényi negativity by using the deformed eigenvalue density (1.3) rather than the original one (1.4).

Chapter 3

We review the recent progress in the black hole information paradox. The aim of this chapter is to explain the methods employed in this study. In particular, we focus on the Penington-Shenker-Stanford-Yang (PSSY) model [14], a toy model of an evaporating black hole in JT gravity with the end of the world (EOW) branes. In the PSSY model, the Page curve of the entanglement entropy is calculated by summing over the several types of replica wormholes. The sum is efficiently calculated by solving the Schwinger-Dyson equation (3.53). The entanglement entropy approaches a constant value at late time of the black hole evaporation since the back-reaction of branes is not considered. Namely, the original eigenvalue density (1.4) is used

to calculate the path integral of JT gravity. The constant value at late time corresponds to the constant thermodynamic entropy. Thus, the black hole in this model is approximated to be eternal, but emits the Hawking radiation.

On the other hand, we also review a generalized model [20] in the matrix model of JT gravity with dynamical FZZT anti-branes. We can use the similar methods to calculate the entanglement entropy as in the PSSY model. Interestingly, the entanglement entropy monotonically decreases at late time in the generalized model by considering the back-reaction of branes. This decreasing behavior is the consequence of the deformed eigenvalue density (1.3). Thus, the generalized model is useful to explore the effects of the black hole evaporation. In chapter 4, we apply this model to the case of the refined Rényi negativity to investigate the effects of the back-reaction.

Chapter 4

We investigate the refined Rényi negativity and the capacity of negativity in JT gravity with dynamical FZZT anti-branes. We consider a bipartite system of the Hawking radiation. The aim of this chapter is to discuss our results [21]. We find that the refined Rényi negativity monotonically decreases at late time of the black hole evaporation due to the back-reaction of branes. The numerical result is shown in Figure 4.4. This decreasing behavior is similar to that of the entanglement entropy. Moreover, we find that the capacity of negativity exhibits two peaks as a function of time, which comes from the exchange of dominance of different types of replica wormholes. These peaks indicate the phase transitions of the entanglement structure between the bipartite Hawking radiation system. The numerical result is shown in Figure 4.6. Finally, we conclude this thesis and discuss some open questions in Chapter 5.

Chapter 2

Matrix model of JT gravity

In this chapter, we review the matrix model of JT gravity with dynamical branes. The aim of this chapter is to explain the formalisms used in later chapters. In particular, we focus on the aspect of JT gravity as a specific example of the two-dimensional topological gravity. The topological gravity is an intersection theory on the moduli space of Riemann surfaces and is also described by a certain double-scaled matrix model with infinitely many couplings $\{t_k\}$. JT gravity is related to the topological gravity in a particular background $t_k = \gamma_k$ in (2.52). In the topological gravity, the insertion of branes amounts to the shift of the couplings $t_k \rightarrow \tilde{t}_k$ in (2.123). We refer this effect as the “back-reaction of branes.” Correspondingly, the eigenvalue density of JT gravity is deformed as (2.127) from the original one (2.103) due to the back-reaction of branes. This deformation of JT gravity plays the essential role to model an evaporating black hole including the back-reaction of the Hawking radiation in section 3.2 and section 4.3.

This chapter is organized as follows. In section 2.1, we briefly review some known results in JT gravity. The path integral of JT gravity can be computed by gluing the building blocks: the trumpet (2.24) and the Weil-Petersson (WP) volume (2.22). In section 2.2, we review some basic formalisms of the topological gravity. In the topological gravity, quantities can be computed from a generating function $F(\{t_k\})$ defined in (2.57). In section 2.3, we review JT gravity with dynamical branes. We obtain the deformed eigenvalue density (2.127) by using the formalisms explained in section 2.2.

2.1 JT gravity and random matrix

We review some known results in JT gravity and the connection with the random matrix model. See also [22] for a recent review and references therein. JT gravity [23, 24, 25] is a two-dimensional solvable toy model of quantum gravity. The path integral of JT gravity can be exactly computed by gluing the building blocks: the trumpet (2.24) and the Weil-Petersson (WP) volume (2.22). The trumpet comes from the path integral of the Schwarzian action (2.20) which describes the boundary reparametrization degrees of freedom while the WP volume comes from the path integral of the bulk metrics. Moreover, JT gravity is also described by a certain double-scaled random matrix model [16]. The path integral of JT gravity corresponds to the matrix integral in the double-scaling limit.

2.1.1 Path integral of JT gravity

Let us review the path integral of JT gravity. The gravitational path integral is defined by the sum over all possible topologies and the sum over all possible geometries (i.e., metrics) on the manifold \mathcal{M} of each topology. Namely, for a given Euclidean action $I[g, \phi]$ of the metric g and the other fields ϕ , the partition function is defined by

$$Z = \sum_{\text{topologies}} \int_{\mathcal{M}} \mathcal{D}g \mathcal{D}\phi e^{-I[g, \phi]}, \quad (2.1)$$

where we include the dividing factor of the volume of the gauge symmetries in the integration measure. In two dimensions, it is known that the topologies of any surfaces are completely classified by the Euler characteristic. The Euler characteristic for the surface $\Sigma_{g,n}$ with genus g and n boundaries is given by

$$\chi(\Sigma_{g,n}) = 2 - 2g - n. \quad (2.2)$$

Thus, the sum over topologies in the partition function (2.1) becomes the sum over Euler characteristics in two dimensions. Note that if we consider the triangulation of the surface Σ , the Euler characteristic is given by the alternating sum of the number of vertices V , edges E , and faces F as

$$\chi(\Sigma) = V - E + F. \quad (2.3)$$

Euclidean action of JT gravity

JT gravity is a model of two-dimensional gravity coupled to a scalar field ϕ called dilaton. The dilaton is introduced as an auxiliary field without the kinetic term. The Euclidean action of JT gravity is given by

$$I_{\text{JT}}[g, \phi] = I_{\text{gravity}}[g] + I_{\text{dilaton}}[g, \phi], \quad (2.4)$$

where the pure gravity term $I_{\text{gravity}}[g]$ is given by the sum of the Einstein-Hilbert term and the Gibbons-Hawking-York [26, 27] boundary term

$$I_{\text{gravity}}[g] = -\frac{S_0}{2\pi} \left(\frac{1}{2} \int_{\Sigma} d^2x \sqrt{g} R + \int_{\partial\Sigma} dx \sqrt{h} \tilde{K} \right), \quad (2.5)$$

and the interaction term $I_{\text{dilaton}}[g, \phi]$ is given by

$$I_{\text{dilaton}}[g, \phi] = -\frac{1}{2} \int_{\Sigma} d^2x \sqrt{g} \phi (R + 2) - \int_{\partial\Sigma} dx \sqrt{h} \phi (\tilde{K} - 1). \quad (2.6)$$

Here $g_{\mu\nu}$ and h denotes the bulk metric on the surface Σ and the induced metric on the boundary $\partial\Sigma$, respectively. R and \tilde{K} are the Ricci scalar and the extrinsic curvature on the boundary, respectively. The extrinsic curvature \tilde{K} is defined by

$$\tilde{K} = g^{\mu\nu} \nabla_{\mu} n_{\nu}, \quad (2.7)$$

where n_{ν} is a unit vector normal to the boundary. The pure gravity action $I_{\text{gravity}}[g]$ is topological (i.e., non-dynamical) since it gives the Euler characteristic by the Gauss-Bonnet theorem, namely

$$-\frac{S_0}{2\pi} \left(\frac{1}{2} \int_{\Sigma} d^2x \sqrt{g} R + \int_{\partial\Sigma} dx \sqrt{h} \tilde{K} \right) = -S_0 \chi(\Sigma). \quad (2.8)$$

Thus, the variation of $I_{\text{gravity}}[g]$ with respect to the metric vanishes

$$\frac{\partial I_{\text{gravity}}[g]}{\partial g_{\mu\nu}} = 0, \quad (2.9)$$

which implies that any geometry is a solution. We impose the boundary conditions for the dilaton ϕ and the induced metric h as

$$\phi|_{\partial\Sigma} = \frac{\gamma}{\epsilon}, \quad h|_{\partial\Sigma} = \frac{1}{\epsilon^2}, \quad (2.10)$$

where γ is a constant later fixed to $\gamma \equiv 1/2\pi^2$ in our convention, and ϵ is a regulator introduced for the cutoff near the asymptotic boundary. We will later take the limit $\epsilon \rightarrow 0$.

Path integral of JT gravity

Let us consider the partition function (2.1) with the action (2.4). We consider the path integral on Riemann surfaces Σ with fixed n boundaries as

$$Z_{\text{JT}} = \sum_{g=0}^{\infty} e^{(2-2g-n)S_0} \int_{\Sigma_{g,n}} \mathcal{D}g \mathcal{D}\phi e^{-I_{\text{dilaton}}[g,\phi]}, \quad (2.11)$$

where we have replaced the sum over topologies by the sum over genus and we have used (2.8) with the Euler characteristic (2.2). Here the path integral of the dilaton can be computed as

$$\int_{\Sigma_{g,n}} \mathcal{D}\phi e^{-I_{\text{dilaton}}[g,\phi]} = \delta(R+2) e^{\frac{\gamma}{\epsilon^2} \int dx (\tilde{K}-1)}, \quad (2.12)$$

where we have chosen the integration contour parallel to the imaginary axis and imposed the boundary conditions for the dilaton and the boundary induced metric in (2.10). Now the bulk geometry is fixed to the constant negative curvature

$$R = -2, \quad (2.13)$$

which implies that the bulk geometry is locally the two-dimensional anti-de Sitter (AdS) space. Thus, we can locally adopt the Poincaré coordinate

$$ds^2 = \frac{dz^2 + dt^2}{z^2}. \quad (2.14)$$

Note that this metric is not defined at $z = 0$ which corresponds to the asymptotic boundary of the two-dimensional AdS space. Thus, we have to cut off the spacetime near the asymptotic boundary as in Figure 2.1. At the cutoff boundary we take [28]

$$z(\tau) = \epsilon t'(\tau), \quad (2.15)$$

where τ denotes the coordinate along the cutoff boundary and $'$ denotes the derivative with respect to τ . Then the metric (2.14) becomes

$$ds^2 = \left((t'')^2 + \frac{1}{\epsilon^2} \right) d\tau^2, \quad (2.16)$$

which is consistent with the boundary condition for the boundary induced metric in (2.10) as we take the limit $\epsilon \rightarrow 0$.

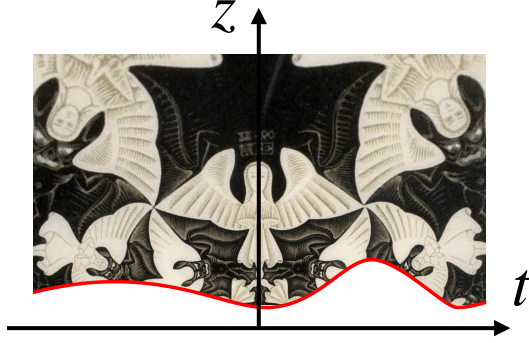


Figure 2.1: Poincaré coordinate in the two-dimensional AdS space [22]. We have to cut off the spacetime near the asymptotic boundary since the metric (2.14) is not defined at $z = 0$.

Let us go back to the partition function. By using (2.12), the partition function Z_{JT} in (2.11) becomes

$$Z_{\text{JT}} = \sum_{g=0}^{\infty} e^{(2-2g-n)S_0} \int_{\Sigma_{g,n}} \mathcal{D}g \delta(R+2) e^{\frac{\gamma}{2} \int dx (\tilde{K}-1)}. \quad (2.17)$$

Here we have to determine the dependence of the bulk metric g in the extrinsic curvature \tilde{K} . The extrinsic curvature \tilde{K} can be computed explicitly by using the metric (2.16) as

$$\tilde{K} = \frac{t'(t'^2 + z'^2 + zz'') - zz't''}{(z'^2 + t'^2)^{\frac{3}{2}}} = 1 + \epsilon^2 \text{Sch}(t, \tau) + \mathcal{O}(\epsilon^4), \quad (2.18)$$

where $\text{Sch}(t, \tau)$ is the Schwarzian derivative defined by

$$\text{Sch}(t, \tau) = \frac{t'''}{t'} - \frac{3}{2} \left(\frac{t''}{t'} \right)^2. \quad (2.19)$$

Thus, the boundary action in the partition function is given by

$$I_{\text{Sch}} = -\gamma \int d\tau \text{Sch}(t, \tau), \quad (2.20)$$

which is referred to as the Schwarzian action in the literature. Note that the Schwarzian action (2.20) is independent of the bulk metric but it depends on a field $t(\tau)$ on the boundary. Namely, the Schwarzian action describes the reparametrization $t(\tau)$ as the dynamical degrees of freedom, which is referred to as the boundary “wiggles” in the literature.

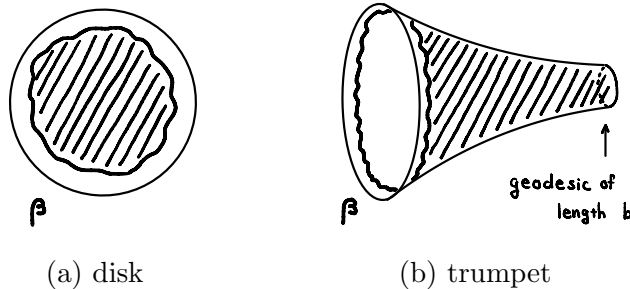


Figure 2.2: The particular cases which we have to treat separately. (a) disk for $(g, n) = (0, 1)$ and (b) trumpet for $(g, n) = (0, 2)$.

Finally, the partition function Z_{JT} in (2.17) can be computed by integrating over the bulk metric and over the boundary wiggles as

$$Z_{\text{JT}} = \sum_{g=0}^{\infty} e^{(2-2g-n)S_0} \int_{\Sigma_{g,n}} \mathcal{D}g \mathcal{D}(\text{wiggles}) e^{-I_{\text{Sch}}(\text{wiggles})}. \quad (2.21)$$

Here the integral over the bulk metric (implicitly divided by the volume of the diffeomorphisms on $\Sigma_{g,n}$) gives the volume of the bulk moduli space $\mathcal{M}_{g,n}$. The volume of $\mathcal{M}_{g,n}$ with the boundary lengths b_1, \dots, b_n is given by the Weil-Petersson (WP) volume $V_{g,n}(b_1, \dots, b_n)$ as

$$V_{g,n}(b_1, \dots, b_n) = \text{vol}(\mathcal{M}_{g,n}(b_1, \dots, b_n)). \quad (2.22)$$

Note that the WP volume is not defined for the particular cases $(g, n) = (0, 1), (0, 2)$ at which the dimension $\dim \mathcal{M}_{g,n} = 3g - 3 + n$ becomes negative. We have to treat these cases separately. The $(g, n) = (0, 1)$ case is the hyperbolic disk shown in Figure 2.2a. The Schwarzian boundary is described by the wiggly curve near the asymptotic boundary. As discussed in [16], the disk partition function with the boundary length β is given by

$$Z_{\text{disk}}(\beta) = \frac{e^{S_0 \gamma^{\frac{3}{2}}}}{(2\pi)^{\frac{1}{2}} \beta^{\frac{3}{2}}} e^{-\frac{2\pi^2 \gamma}{\beta}}. \quad (2.23)$$

The $(g, n) = (0, 2)$ case is the trumpet shown in Figure 2.2b. The trumpet has two boundaries one of which is taken to be a geodesic. As discussed in [16], the trumpet partition function is given by

$$Z_{\text{trumpet}}(\beta, b) = \sqrt{\frac{\gamma}{2\pi\beta}} e^{-\frac{\gamma b^2}{2\beta}}. \quad (2.24)$$

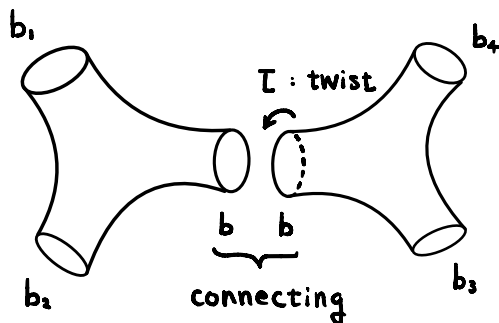


Figure 2.3: Gluing pants with length b and relative twist τ .

Let us make some comments on the WP volume. Riemann surfaces can be constructed by gluing the building blocks called “pants,” a hyperbolic surface with genus zero and three boundaries as shown in Figure 2.3. Each boundary connected with other pants is associated to two parameters, the length of the connected boundary b and the relative twist between the pants τ . It is known that the Riemann surface $\Sigma_{g,n}$ with genus g and n boundaries is divided by $3g + n - 3$ geodesics into the set of pants. Thus, there is a set of parameters $\{(b_i, \tau_i)\}, (i = 1, \dots, 3g + n - 3)$ associated to the pants decomposition. This set of coordinates is known as the Fenchel-Nielsen coordinates. From the set of coordinates the Weil-Petersson symplectic form is defined by

$$\omega = \alpha \sum_{i=1}^{3g+n-3} db_i \wedge d\tau_i, \quad (2.25)$$

and it defines the associated volume form on the moduli space of the Riemann surface. The parameter α is a numerical constant and we set $\alpha = 1$ in our convention. The WP volume $V_{g,n}(b_1, \dots, b_n)$ is given by integrating the volume form over the fundamental region of the moduli space. However, the integration is not easy to calculate directly. Instead, the WP volume can be computed recursively by using Mirzakhani’s recursion relation [29]. The WP volume can also be computed more efficiently by using the techniques in the two-dimensional topological gravity [30] which was developed based on the idea of [31].

To summarize, the partition function of JT gravity Z_{JT} in (2.21) can be computed by gluing the trumpet (2.24) and the WP volume (2.22) for general geometry with n boundaries except for the disk and trumpet. If we

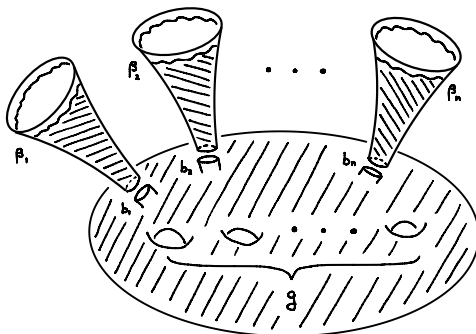


Figure 2.4: The partition function of JT gravity with n boundaries.

define the genus g part of the partition function $Z_{g,n}$ with n boundaries of the lengths β_1, \dots, β_n as

$$Z_{\text{JT}}(\beta_1, \dots, \beta_n) = \sum_{g=0}^{\infty} e^{(2-2g-n)S_0} Z_{g,n}(\beta_1, \dots, \beta_n), \quad (2.26)$$

$Z_{g,n}(\beta_1, \dots, \beta_n)$ is given by gluing the trumpets and the WP volume as

$$Z_{g,n}(\beta_1, \dots, \beta_n) = \prod_{i=1}^n \int_0^{\infty} b_i db_i Z_{\text{trumpet}}(\beta_i, b_i) V_{g,n}(\mathbf{b}). \quad (2.27)$$

This prescription is shown in Figure 2.4. As seen from Figure 2.4, we can cut off the Schwarzian boundaries by geodesics with lengths b_1, \dots, b_n and gluing them again. The integration measure comes from the Weil-Petersson symplectic form (2.25) after integrating over the twist coordinate

$$\int_0^{\infty} db \int_0^b d\tau = \int_0^{\infty} b db. \quad (2.28)$$

Our convention

In the following sections, we will use the convention in [30]. We set the parameters γ and g_s as

$$\gamma \equiv \frac{1}{2\pi^2}, \quad g_s \equiv (2\pi^2)^{\frac{3}{2}} e^{-S_0}. \quad (2.29)$$

The parameter g_s is referred to as the genus counting parameter as we will see later. We also define the rescaled trumpet and the rescaled WP volume

so that the partition function of JT gravity is given by

$$Z_{\text{JT}}(\beta_1, \dots, \beta_n) = \sum_{g=0}^{\infty} g_s^{2g-2+n} \prod_{i=1}^n \int_0^{\infty} b_i db_i Z_{\text{trumpet}}(\beta_i, b_i) V_{g,n}(\mathbf{b}), \quad (2.30)$$

where the rescaled trumpet partition function $Z_{\text{trumpet}}(\beta, b)$ is given by

$$Z_{\text{trumpet}}(\beta, b) = \frac{e^{-\frac{b^2}{2\beta}}}{\sqrt{2\pi\beta}}, \quad (2.31)$$

and the WP volume $V_{g,n}(\mathbf{b})$ is rescaled from the original one $\tilde{V}_{g,n}(\mathbf{b})$ as

$$V_{g,n}(\mathbf{b}) = (2\pi^2)^{3-3g-n} \tilde{V}_{g,n}(\mathbf{b}). \quad (2.32)$$

Correspondingly, the disk partition function is given by

$$Z_{\text{disk}}(\beta) = \frac{1}{\sqrt{2\pi g_s} \beta^{\frac{3}{2}}} e^{\beta^{-1}}. \quad (2.33)$$

2.1.2 Random matrix model

We briefly review some basic concepts of the random matrix model related to the two-dimensional quantum gravities. The random matrix model is a statistical model whose variables are matrices distributed in a certain probability distribution. Such a model was first introduced by Wishart [32] and first applied to physical problem by Wigner [33] to calculate the energy spectrum of heavy nucleus. We particularly consider $N \times N$ Hermitian matrix H which is regarded as the Hamiltonian of the system. In quantum gravity, random matrix models have been considered since 1980s. See also [34, 35, 36] for reviews and references therein. The basic idea comes from that the discretized path integral of the two-dimensional gravity in (2.1) is given by the sum over the random triangulations of Riemann surfaces which corresponds to the sum over the Feynman diagrams of random matrices:

$$\sum_{\text{topologies}} \int \mathcal{D}g \xrightarrow{\text{discretize}} \sum_{\substack{\text{random} \\ \text{triangulations}}} = \sum_{\substack{\text{Feynman diagrams} \\ \text{of random matrices}}}. \quad (2.34)$$

This picture is shown in Figure 2.5. To obtain the original continuous results of gravity from the discretized theory, we have to take the double-scaling limit. Namely, we take the limit of the size of the matrices $N \rightarrow \infty$ and fine-tune the couplings in the matrix potential $V(H)$ in a specific way.

Matrix integral

Let us define the random matrix model. A random matrix model is defined by the matrix integral which gives the probability distribution of the matrices. We define the matrix integral for $N \times N$ Hermitian matrix H by

$$Z = \int dH e^{-\text{Tr}V(H)}, \quad (2.35)$$

where $V(H)$ is a polynomial of H , called the matrix potential. The matrix potential is viewed as the action of the random matrix model. In this model, we consider the ensemble average of operators depend on H . Namely, the ensemble average of $\mathcal{O}(H)$ is defined by

$$\langle \mathcal{O} \rangle = \frac{1}{Z} \int dH e^{-\text{Tr}V(H)} \mathcal{O}(H). \quad (2.36)$$

In the matrix model of JT gravity, we are particularly interested in the following single-trace operator

$$Z(\beta) = \text{Tr}e^{-\beta H}, \quad (2.37)$$

which is called the macroscopic loop operator in the matrix model. As proved in [16], the partition function of JT gravity with single boundary of length β is equivalent to the ensemble average of the macroscopic loop operator (2.37) in a certain double-scaling limit (DSL),

$$Z_{\text{JT}}(\beta) = \langle Z(\beta) \rangle_{\text{DSL}}. \quad (2.38)$$

Similarly, the partition function of JT gravity on Riemann surfaces with fixed n boundaries of the lengths β_1, \dots, β_n corresponds to the n point connected correlator of the macroscopic loop operators as

$$Z_{\text{JT}}(\beta_1, \dots, \beta_n) = \langle Z(\beta_1) \cdots Z(\beta_n) \rangle_{\text{conn.}}. \quad (2.39)$$

On the other hand, the partition function of JT gravity $Z_{\text{JT}}(\beta_1, \dots, \beta_n)$ is also computed by gluing the trumpets and the WP volume as in (2.30). Thus, the connected correlator (2.39) is given by

$$\left\langle \prod_{i=1}^n Z(\beta_i) \right\rangle_{\text{conn.}} = \sum_{g=0}^{\infty} g_s^{2g-2+n} \prod_{i=1}^n \int_0^{\infty} b_i db_i Z_{\text{trumpet}}(\beta_i, b_i) V_{g,n}(\mathbf{b}). \quad (2.40)$$

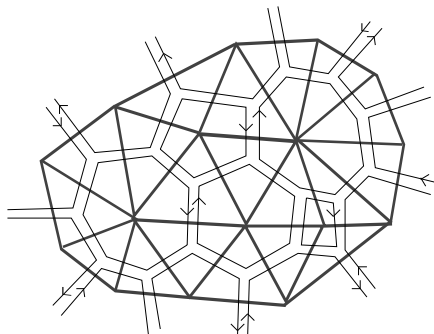


Figure 2.5: Random triangulation of a surface and the Feynman diagram of the random matrix model for three point interaction [34].

In the original paper [16], the duality between JT gravity and the random matrix model was proved up to all orders in the genus expansion. The proof was based on the correspondence between the Mirzakhani’s recursion relation for the WP volume [29] and the Eynard-Orantin’s topological recursion for the resolvent of the random matrix model [37, 38, 39]. In this thesis, we will use these results for the applications of the matrix model of JT gravity. In particular, we use the above results to evaluate the effects of the insertion of branes to the matrix model of JT gravity in section 2.2.

Genus expansion

We briefly comment on a perturbative expansion, namely the genus expansion of the matrix integral (2.35). We will see that the sum over Feynman diagrams of random matrices corresponds to the sum over topologies and geometries in the two-dimensional gravitational path integral. First, the matrix integral (2.35) is exactly solvable if the potential $V(H)$ is up to the second order in H , which is called the Gaussian matrix model or the Gaussian unitary ensemble (GUE) such as

$$V_{\text{GUE}}(H) = \frac{H^2}{2}. \quad (2.41)$$

As with the usual quantum field theory, the two point function in the Gaussian matrix model can be computed as

$$\langle H_{ij} H_{kl} \rangle_{\text{GUE}} = \delta_{il} \delta_{jk}, \quad (2.42)$$

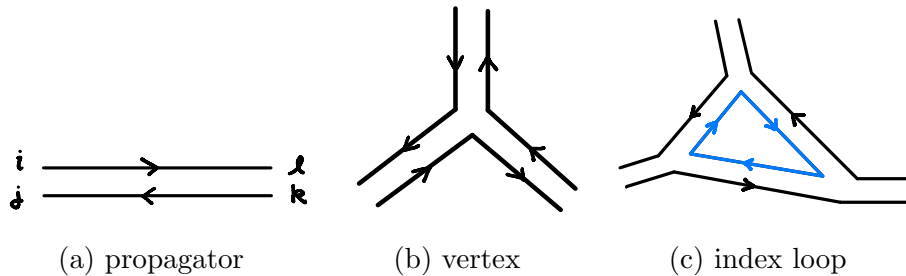


Figure 2.6: Feynman diagrams for three point interaction of the matrix model. Each double line corresponds to each propagator.

which is viewed as the propagator in the matrix model. The propagator (2.42) can be represented by a double-line diagram 2.6a. Such a double-line formalism is originally introduced by 't Hooft [40] for the analysis of the theory of strong interaction.

Let us consider a generalized matrix potential $V(H)$ including the interaction terms with couplings $\{c_k\}_{k \geq 3}$ as

$$V(H) = \frac{1}{g_s} \left(\frac{H^2}{2} + c_3 H^3 + c_4 H^4 + \dots \right), \quad (2.43)$$

where we have rescaled the matrix potential by a parameter g_s . We refer g_s as the genus counting parameter so that the genus expansion becomes manifest. In this model the propagator (2.42) is rescaled as

$$\langle H_{ij} H_{kl} \rangle = g_s \delta_{il} \delta_{jk}, \quad (2.44)$$

since the propagator is proportional to the inverse of the coefficient of the quadratic term of the action. We evaluate the matrix integral (2.35) with the potential (2.43) by expanding around the Gaussian ensemble as

$$Z = \sum_{m=0}^{\infty} \frac{1}{m!} \int dH e^{-\frac{1}{g_s} \text{Tr} \frac{H^2}{2}} g_s^{-m} [\text{Tr} (c_3 H^3 + \dots)]^m. \quad (2.45)$$

Now the matrix integral can be computed by using the Wick contraction and this expansion gives the sum over Feynman diagrams. We show an example of Feynman diagram for the three point interaction in Figure 2.5.

Let us read off the Feynman rules. As we see from (2.45), each interaction vertex is weighted by g_s^{-1} . We show an example of the interaction vertex for

the three point interaction in Figure 2.6b. From Figure 2.6c, index loops will appear and each loop is weighted by $\delta_{ii} = N$. Thus, the contribution of a Feynman diagram with V vertices, E propagators, and F index loops is given by

$$g_s^{-V+E} N^F = g_s^{-V+E-F} (g_s N)^F. \quad (2.46)$$

Here the power of g_s is nothing but the Euler characteristic in (2.3) with the appropriate identifications. Actually, if we define the genus g for the Feynman diagram by

$$2 - 2g = V - E + F, \quad (2.47)$$

g corresponds to the genus of the surface on which we can draw the diagram. For example, the genus $g = 0$ for all planar diagrams.

Similarly, let us consider the insertion of a single-trace operator. For example, let us consider the expectation value of $\text{Tr}H^3$ as

$$\begin{aligned} \langle \text{Tr}H^3 \rangle &\sim \int dH e^{-\text{Tr}V(H)} \text{Tr}H^3 \\ &\sim \sum_{m=0}^{\infty} \frac{1}{m!} \int dH e^{-\frac{1}{g_s} \text{Tr} \frac{H^2}{2}} [g_s^{-1} \text{Tr} (c_3 H^3 + \dots)]^m \text{Tr}H^3, \end{aligned} \quad (2.48)$$

where we have omitted the overall normalization factor. Now we can also compute the matrix integral by using the Wick contraction. The operator $\text{Tr}H^3$ behaves like the vertex of the three point interaction but the vertex associated to $\text{Tr}H^3$ is not weighted by g_s^{-1} . Thus, the insertion of $\text{Tr}H^3$ changes the weight of the diagram as $g_s^{-(V-1)}$. In general, n insertion of single-trace operators changes the weight of the diagram as g_s^{2g-2+n} .

Finally, we make a brief comment on the double-scaling limit of the matrix model. If we take the following 't Hooft limit

$$N \rightarrow \infty, \quad g_s \rightarrow 0, \quad \text{with } t \equiv g_s N \text{ fixed}, \quad (2.49)$$

the sum in (2.45) becomes the perturbative expansion in g_s as

$$Z = \sum_{g=0}^{\infty} g_s^{2g-2} F_g(t, c_3, c_4, \dots), \quad (2.50)$$

where we denote the coefficients by $F_g(t, c_3, c_4, \dots)$. By using $t \equiv g_s N$, this small g_s expansion can also be viewed as the N^{-1} expansion

$$Z = \sum_{g=0}^{\infty} N^{2-2g} \tilde{F}_g(t, c_3, c_4, \dots), \quad (2.51)$$

where we define $\tilde{F}_g = t^{2g-2}F_g$. From this expression, the higher genus contributions seem to be suppressed in the large N limit. On the other hand, all genus contributions should be summed over in the original gravitational path integral in (2.34). As discussed in [34], all genus contributions can be included in the genus expansion (2.51) if we tune the couplings of the matrix potential in a specific way simultaneously with the large N limit. Such a limit is called the double-scaling limit.

2.2 Two-dimensional topological gravity

In this section, we review the connection between JT gravity and the two-dimensional topological gravity [41, 42] (see [43] for a recent review) following [30]. The two-dimensional topological gravity is an intersection theory on the moduli space of Riemann surfaces and is described by a certain double-scaled random matrix model with infinitely many couplings $\{t_k\}$. As discussed in [30], JT gravity is nothing but a specific example of the topological gravity in a particular background $t_k = \gamma_k$ with

$$\gamma_0 = \gamma_1 = 0, \quad \gamma_k = \frac{(-1)^k}{(k-1)!} \quad (k \geq 2). \quad (2.52)$$

The connection with the topological gravity provides some efficient computational methods such as the Korteweg-de Vries (KdV) equations and the dynamical treatment of branes. The KdV equation is a useful tool to compute the higher genus contributions in the path integral of JT gravity but we will not review much about that (see [30] for the details). In this thesis, we focus on the basic formalisms for the dynamical treatment of branes.

2.2.1 JT gravity as a topological gravity

Let us consider the two-dimensional Riemann surfaces Σ with genus g and n marked points p_1, \dots, p_n . We are interested in the intersection numbers

$$\langle \kappa^m \tau_{d_1} \cdots \tau_{d_n} \rangle_g = \int_{\overline{\mathcal{M}}_{g,n}} \kappa^m \psi_1^{d_1} \cdots \psi_n^{d_n}, \quad m, d_1, \dots, d_n \in \mathbb{Z}_{\geq 0}, \quad (2.53)$$

which is viewed as the correlation function of the topological gravity. Here $\overline{\mathcal{M}}_{g,n}$ is the Deligne-Mumford compactification of the moduli space $\mathcal{M}_{g,n}$ of

the Riemann surface Σ and κ is the first Miller-Morita-Mumford class which is proportional to the Weil-Petersson symplectic form (2.25) as

$$\omega = 2\pi^2 \kappa. \quad (2.54)$$

The integrand ψ_i is the first Chern class of the complex line bundle whose fiber is the cotangent space to the marked point p_i and $\tau_{d_i} = \psi_i^{d_i}$. Note that (2.53) vanishes unless $m + d_1 + \dots + d_n = 3g - 3 + n$. In this theory, the Weil-Petersson (WP) volume is given by

$$V_{g,n}(\mathbf{b}) = \int_{\mathcal{M}_{g,n}} e^{\kappa + \frac{1}{2} \sum_{i=1}^n b_i^2 \psi_i} \equiv \left\langle e^{\kappa + \frac{1}{2} \sum_{i=1}^n b_i^2 \psi_i} \right\rangle_g, \quad (2.55)$$

where this formula is valid except for $V_{0,1}, V_{0,2}$. We need to consider $(g, n) = (0, 1), (0, 2)$ separately but we will not so much care about these cases unless necessary. It is convenient to introduce the generating functions for the intersection numbers (2.53) as

$$G(s, \{t_k\}) = \sum_{g=0}^{\infty} g_s^{2g-2} \left\langle e^{s\kappa + \sum_{d=0}^{\infty} t_d \tau_d} \right\rangle_g, \quad (2.56)$$

$$F(\{t_k\}) = \sum_{g=0}^{\infty} g_s^{2g-2} \left\langle e^{\sum_{d=0}^{\infty} t_d \tau_d} \right\rangle_g. \quad (2.57)$$

It is known that these generating functions are related [43, 44] by

$$G(s, \{t_k\}) = F(\{t_k + \gamma_k s^{k-1}\}) \quad (2.58)$$

with

$$\gamma_0 = \gamma_1 = 0, \quad \gamma_k = \frac{(-1)^k}{(k-1)!} \quad (k \geq 2). \quad (2.59)$$

One can compute various quantities from the generating functions, in particular the partition function of JT gravity.

Partition function of JT gravity

Let us explore the connection between JT gravity and the topological gravity by considering the partition function of JT gravity following [30]. As discussed in section 2.1, the partition function of JT gravity with single

boundary of length β is given by (2.38). It contains all genus contributions in the genus expansion as

$$\langle Z(\beta) \rangle = \langle Z(\beta) \rangle_{g=0} + \langle Z(\beta) \rangle_{g \geq 1}. \quad (2.60)$$

The genus-zero part is given by the disk partition function (2.33) as

$$\langle Z(\beta) \rangle_{g=0} = \frac{1}{\sqrt{2\pi} g_s \beta^{\frac{3}{2}}} e^{\beta^{-1}}. \quad (2.61)$$

Let us consider the higher genus ($g \geq 1$) contribution. It is given by gluing the trumpet partition function (2.31) and the WP volume (2.32) as

$$\langle Z(\beta) \rangle_{g \geq 1} = \sum_{g=1}^{\infty} g_s^{2g-1} \int_0^{\infty} b db Z_{\text{trumpet}}(\beta, b) V_{g,1}(b). \quad (2.62)$$

Here the WP volume is given by (2.55) as

$$V_{g,1}(b) = \sum_{d=0}^{3g-2} \frac{1}{(3g-2-d)! d!} \left(\frac{b^2}{2} \right)^d \langle \kappa^{3g-2-d} \psi^d \rangle_g, \quad (2.63)$$

where we have expanded the exponential and used the following property

$$\langle \kappa^k \psi^l \rangle_g = 0 \quad \text{unless} \quad k + l = 3g - 2. \quad (2.64)$$

Substituting (2.63) into (2.62) and integrating over b , the higher genus contribution becomes

$$\begin{aligned} \langle Z(\beta) \rangle_{g \geq 1} &= \frac{1}{\sqrt{2\pi}} \sum_{g=1}^{\infty} \sum_{d=0}^{3g-2} g_s^{2g-1} \frac{\beta^{d+\frac{1}{2}}}{(3g-2-d)!} \langle \kappa^{3g-2-d} \psi^d \rangle_g \\ &= \frac{1}{\sqrt{2\pi}} \sum_{g=1}^{\infty} \sum_{d=0}^{\infty} g_s^{2g-1} \beta^{d+\frac{1}{2}} \langle e^{\kappa} \psi^d \rangle_g, \end{aligned} \quad (2.65)$$

where we have used (2.64) to obtain the second equality. By using the generating functions (2.56) and (2.57), we have the following relations for $g \geq 1$

$$\begin{aligned} \sum_{g=1}^{\infty} g_s^{2g-2} \langle e^{\kappa} \psi^d \rangle_g &= \partial_d G(s=1, \{t_k=0\}) \\ &= \partial_d F(\{t_k=\gamma_k\}), \end{aligned} \quad (2.66)$$

where we define the derivative $\partial_d = \partial/\partial t_d$. Thus, the higher genus contribution of the partition function is given by

$$\langle Z(\beta) \rangle_{g \geq 1} = \frac{g_s}{\sqrt{2\pi}} \sum_{d=0}^{\infty} \beta^{d+\frac{1}{2}} \partial_d F(\{t_k = \gamma_k\}). \quad (2.67)$$

Finally, from the genus-zero part (2.61) and the higher genus part (2.67), the full partition function of JT gravity is given by

$$\langle Z(\beta) \rangle = \frac{g_s}{\sqrt{2\pi} \beta^{\frac{3}{2}}} \left(g_s^{-2} e^{\beta^{-1}} + \sum_{d=0}^{\infty} \beta^{d+2} \partial_d F(\{t_k = \gamma_k\}) \right). \quad (2.68)$$

Therefore the partition function of JT gravity is written in terms of the generating function of the topological gravity in a specific background $t_k = \gamma_k$ in (2.52). Here we comment on the differential operator

$$B(\beta) = \frac{g_s}{\sqrt{2\pi}} \sum_{d=0}^{\infty} \beta^{d+\frac{1}{2}} \partial_d, \quad (2.69)$$

which is acting on the generating function $F(\{t_k\})$ in (2.67). This is nothing but the boundary creation operator [45] which generates the connected correlator of multiple boundaries

$$\langle Z(\beta_1) \cdots Z(\beta_n) \rangle_{\text{conn.}} \simeq B(\beta_1) \cdots B(\beta_n) F(\{t_k\}). \quad (2.70)$$

The symbol “ \simeq ” means that this equation holds up to an additional non-universal part. Namely, we have to treat the disk (2.33) and the trumpet (2.31) contributions separately as discussed in the previous section.

2.2.2 Generalized partition function

Let us explore another expression of the partition function $\langle Z(\beta) \rangle$ for the use to obtain the leading order eigenvalue density of JT gravity in the next subsection. In the topological gravity, e^F with F in (2.57) is called the tau function for the KdV hierarchy. This means that a function

$$u = g_s^2 \partial_0^2 F \quad (2.71)$$

satisfies the (generalized) KdV equation

$$\partial_k u = \partial_0 \mathcal{R}_{k+1}, \quad \partial_k \equiv \partial/\partial t_k, \quad (2.72)$$

where \mathcal{R}_k is the Gelfand-Dikki differential polynomials of u . It is known that the Gelfand-Dikki polynomials satisfy the following recursion relation

$$(2k+1)D_0\mathcal{R}_{k+1} = \frac{1}{4}D_0^3\mathcal{R}_k + 2uD_0\mathcal{R}_k + (D_0u)R_k, \quad D_k \equiv g_s\partial_k \quad (2.73)$$

with the initial value $\mathcal{R}_0 = 1$. By integrating (2.72) over t_0 , we also have a constraint for F as

$$g_s^2\partial_k\partial_0F = \mathcal{R}_{k+1}. \quad (2.74)$$

Let us consider a two-parameter generalization of F from JT gravity background which is well-defined at least around $(t_0, t_1) = (0, 0)$ as

$$F(t_0, t_1) = F(t_0, t_1, \{t_k = \gamma_k\}). \quad (2.75)$$

Using this generalized function F , we also define a two-parameter deformation of the partition function (2.68) as

$$Z_{\text{JT}}(t_0, t_1) = \frac{g_s}{\sqrt{2\pi\beta^{\frac{3}{2}}}} \left(g_s^{-2}e^{\beta^{-1}} + g_s^{-2}\beta t_0 + \sum_{d=0}^{\infty} \beta^{d+2}\partial_d F(t_0, t_1) \right), \quad (2.76)$$

which reproduces the original one at $(t_0, t_1) = (0, 0)$, i.e., $Z_{\text{JT}}(0, 0) = \langle Z(\beta) \rangle$. Here we introduce some rescaled variables for later use

$$\hbar = \frac{1}{\sqrt{2}}g_s, \quad x = \hbar^{-1}t_0, \quad \tau = \hbar^{-1}t_1. \quad (2.77)$$

The derivative of (2.76) with respect to x gives the generating function of the Gelfand-Dikki polynomials as

$$\partial_x Z_{\text{JT}}(t_0, t_1) = \frac{1}{2\sqrt{\pi\beta}} \sum_{d=0}^{\infty} \beta^d \mathcal{R}_d \equiv W(\beta), \quad (2.78)$$

where we have used $\mathcal{R}_0 = 1$ and the constraint (2.74). Let us consider the Laplace transformation of $W(\beta)$ as

$$R(\eta) = \int_0^{\infty} d\beta e^{-\beta\eta} W(\beta). \quad (2.79)$$

If we expand $R(\eta)$ as

$$R(\eta) = \sum_{k=0}^{\infty} \eta^{-k-\frac{1}{2}} R_k, \quad (2.80)$$

the coefficients are also the Gelfand-Dikki polynomials

$$R_k = \frac{(2k-1)!!}{2^{k+1}} \mathcal{R}_k. \quad (2.81)$$

This is same as the original Gelfand-Dikki polynomials [46] and it is known that such $R(\eta)$ is the “resolvent” for the Schrödinger equation

$$Q\psi = \eta\psi, \quad Q \equiv \partial_x^2 + u. \quad (2.82)$$

The “resolvent” means that $R(\eta)$ satisfies

$$R(\eta) = \left\langle x \left| \frac{1}{\eta - Q} \right| x \right\rangle, \quad (2.83)$$

where $|x\rangle$ is the coordinate eigenstate. By taking the inverse Laplace transformation of (2.83) we obtain

$$W(\beta) = \langle x | e^{\beta Q} | x \rangle. \quad (2.84)$$

Thus, the partition function of JT gravity is given by integrating (2.78) with $W(\beta)$ in (2.84) as

$$Z_{\text{JT}} = \int_{-\infty}^x dx' \langle x' | e^{\beta Q} | x' \rangle. \quad (2.85)$$

If we introduce the projection operator

$$\Pi = \int_{-\infty}^x dx' |x'\rangle \langle x'|, \quad (2.86)$$

the partition function is also expressed as

$$Z_{\text{JT}} = \text{Tr}(e^{\beta Q} \Pi), \quad (2.87)$$

which is referred to as (the expectation value of) the macroscopic loop operator in the matrix model of the topological gravity. Thus, JT gravity is nothing but a specific example of the two-dimensional topological gravity.

2.2.3 Leading order eigenvalue density

Let us obtain the leading order (genus-zero) eigenvalue density $\rho_0(E)$ of JT gravity, which is defined by the Laplace transformation of the genus-zero part of the partition function

$$Z_{\text{JT}}^{(g=0)}(\beta) = \int_{E_0}^{\infty} dE e^{-\beta E} \rho_0(E). \quad (2.88)$$

Here E_0 is the threshold energy which we will determine later. The expression (2.85) for the partition function is useful to obtain $\rho_0(E)$. It is convenient to define a function with couplings $\{t_k\}$ of general topological gravity

$$f(u) = \sum_{k=0}^{\infty} (\delta_{k,1} - t_k) \frac{u^k}{k!}. \quad (2.89)$$

This function is also expressed as

$$f(u) = u - I_0(u, \{t_k\}), \quad (2.90)$$

where $I_n(u, \{t_k\})$ is the Itzykson-Zuber variable [47] defined by

$$I_n(u, \{t_k\}) = \sum_{k=0}^{\infty} t_{n+k} \frac{u^k}{k!}. \quad (2.91)$$

We also consider the expansion of u in (2.71) as

$$u = \sum_{g=0}^{\infty} g_s^{2g} u_g, \quad u_g \equiv \partial_0^2 F_g, \quad (2.92)$$

where F_g is defined by

$$F_g = \left\langle e^{\sum_{d=0}^{\infty} t_d \tau_d} \right\rangle_g, \quad (2.93)$$

in the genus expansion of F in (2.57). It is known that u_0 in (2.92) satisfies the genus-zero ‘‘string equation’’ $f(u_0) = 0$, or equivalently

$$u_0 - I_0(u_0, \{t_k\}) = 0. \quad (2.94)$$

This equation can be interpreted as the stationary condition $\partial F_0 / \partial u_0 = 0$ of the genus-zero free energy

$$F_0 = \frac{1}{2} \int_0^{u_0} dv (v - I_0(v, \{t_k\}))^2. \quad (2.95)$$

One can confirm that this expression of F_0 is consistent with u_0 defined in (2.92) by differentiating F_0 twice with respect to t_0 . Here not only $I_0(v, \{t_k\})$ but also u_0 in the upper limit of the integration implicitly depends on t_0 .

Let us consider the leading order (genus-zero) contribution of the partition function $Z_{JT}(\beta)$ in (2.85). By inserting the completeness relation for the

momentum basis states, the leading order partition function becomes

$$\begin{aligned}
Z_{\text{JT}}^{(g=0)}(\beta) &= \int_{-\infty}^x dx' \int_{-\infty}^{\infty} \frac{dp}{2\pi} e^{\beta(-p^2+u_0(x'))} \\
&= \frac{1}{2\sqrt{\pi\beta}} \int_{-\infty}^x dx' e^{\beta u_0(x')} \\
&= \frac{1}{2\sqrt{\pi\beta}} \int_{-\infty}^{u_0} du \frac{\partial x}{\partial u} e^{\beta u},
\end{aligned} \tag{2.96}$$

where we have used $Q = \partial_x^2 + u$ in (2.82) with $p = -i\partial_x$ in the first equality. Here x -dependence of u_0 is determined by the genus-zero string equation (2.94) with the definition of the rescaled variable $t_0 = \hbar x$ in (2.77). The genus-zero string equation (2.94) can be rewritten as

$$\hbar x = u_0 - \sum_{k=1}^{\infty} t_k \frac{u_0^k}{k!}. \tag{2.97}$$

From this relation we obtain

$$\frac{\partial x}{\partial u} = \frac{1}{\hbar} \frac{\partial f(u)}{\partial u}, \tag{2.98}$$

where $f(u)$ is the function defined in (2.89). Substituting this into (2.96) and changing the integration variable as $v = -u$, the leading order partition function becomes

$$Z_{\text{JT}}^{(g=0)}(\beta) = \frac{1}{2\hbar\sqrt{\pi\beta}} \int_{-u_0}^{\infty} dv \frac{\partial f(-v)}{\partial(-v)} e^{-\beta v}. \tag{2.99}$$

By using the following formula

$$\sqrt{\frac{\pi}{\beta}} e^{-\beta v} = \int_v^{\infty} dE \frac{e^{\beta E}}{\sqrt{E-v}}, \tag{2.100}$$

we obtain

$$Z_{\text{JT}}^{(g=0)}(\beta) = \int_{-u_0}^{\infty} dE e^{-\beta E} \rho_0(E), \tag{2.101}$$

where $\rho_0(E)$ can be identified as

$$\rho_0(E) = \frac{1}{\sqrt{2\pi g_s}} \int_{E_0}^E \frac{dv}{\sqrt{E-v}} \frac{\partial f(-v)}{\partial(-v)}, \tag{2.102}$$

with the threshold energy $E_0 = -u_0$. The threshold energy E_0 is also determined by $f(-E_0) = 0$ since u_0 is determined by the genus-zero string

equation $f(u_0) = 0$ or equivalently (2.94). In particular, if we set the parameters $t_k = \gamma_k$ of (2.52) for JT gravity, the threshold energy is determined as $E_0 = 0$ and the leading order eigenvalue density (2.102) reduces to

$$\rho_0^{\text{JT}}(E) = \frac{\sinh(2\sqrt{E})}{\sqrt{2\pi}g_s}. \quad (2.103)$$

One can obtain the disk partition function (2.61) by substituting the eigenvalue density (2.103) into (2.88).

2.3 JT gravity with dynamical branes

In this section, we review the leading order eigenvalue density of JT gravity with dynamical branes following [17]. The eigenvalue density is deformed from the original one (2.103) due to the back-reaction of the branes. Here we particularly focus on the Fateev-Zamolodchikov-Zamolodchikov-Teschner (FZZT) [18, 19] anti-branes which we consider to model an evaporating black hole in section 3.2 and 4.3. The FZZT anti-brane appears as a boundary condition of JT gravity [48] and corresponds to the determinant operator (2.104) in the matrix model. The insertion of FZZT anti-branes amounts to the shift of the couplings $\{t_k\}$ of the topological gravity, which can be obtained by considering the connected correlator of multiple boundaries. Finally, we obtain the deformed eigenvalue density (2.127) from (2.102) with the couplings shifted by the branes.

2.3.1 Correlator with FZZT anti-branes

In the matrix model, the FZZT anti-brane corresponds to the determinant operator $\det(\xi + H)^{-1}$, where H is the Hermitian random matrix variable and ξ is a formal parameter. The insertion of the FZZT anti-brane introduces the vector degrees of freedom in the matrix integral

$$\det(\xi + H)^{-1} = \int d\phi d\bar{\phi} e^{\bar{\phi}(\xi + H)\phi}, \quad (2.104)$$

where $\phi, \bar{\phi}$ are Grassmann-even (bosonic) vector variables. Let us prepare some useful formulas to treat the FZZT anti-branes in the matrix integral.

The determinant operator corresponds to the infinitely many single trace operator $-\text{Tr} \log(\xi + H)$ as

$$\det(\xi + H)^{-1} = e^{-\text{Tr} \log(\xi + H)} = \sum_{n=0}^{\infty} \frac{1}{n!} [-\text{Tr} \log(\xi + H)]^n. \quad (2.105)$$

The single trace operator $-\text{Tr} \log(\xi + H)$ can be represented by the integral transformation of the macroscopic loop operator $Z(\beta) = \text{Tr} e^{-\beta H}$ as

$$-\text{Tr} \log(\xi + H) = \int_{\epsilon}^{\infty} \frac{d\beta}{\beta} e^{-\xi\beta} Z(\beta) + \log \epsilon + \mathcal{O}(\epsilon^0), \quad (2.106)$$

where ϵ is a small regularization parameter. We can ignore the divergent term $\log \epsilon$ by taking an appropriate normalization.

Let us introduce $\mathcal{M}(b)$ by the integral transformation (2.106) of the trumpet partition function (2.31) as

$$\frac{1}{b} \mathcal{M}(b) = \int_0^{\infty} \frac{d\beta}{\beta} e^{-\xi\beta} Z_{\text{trumpet}}(\beta, b). \quad (2.107)$$

By using the integral representation of the Bessel function

$$K_{\frac{1}{2}}(x) = \frac{1}{2} \sqrt{\frac{x}{2}} \int_0^{\infty} dt t^{-\frac{3}{2}} e^{-t - \frac{t^2}{4x}} = \sqrt{\frac{\pi}{2x}} e^{-x}, \quad (2.108)$$

the factor $\mathcal{M}(b)$ in (2.107) is given by

$$\mathcal{M}(b) = e^{-zb}, \quad (2.109)$$

where z is related to ξ by

$$\xi = \frac{1}{2} z^2. \quad (2.110)$$

Note that the integral representation (2.108) is valid for $|\arg(x)| < \pi/4$. This implies that the equation (2.109) is valid only for $\text{Re}(\xi) > 0$.

Thus, the connected correlator with FZZT anti-brane is given by

$$\begin{aligned} & \left\langle \det(\xi + H)^{-1} \prod_{i=1}^m Z(\beta_i) \right\rangle_{\text{conn.}} \\ &= \sum_{n=0}^{\infty} \frac{1}{n!} \prod_{j=0}^n \int_0^{\infty} \frac{d\beta'_j}{\beta'_j} e^{-\xi\beta'_j} \left\langle \prod_{j=1}^n Z(\beta'_j) \prod_{i=1}^m Z(\beta_i) \right\rangle_{\text{conn.}} \end{aligned}$$

$$\begin{aligned}
&= \sum_{n=0}^{\infty} \frac{1}{n!} \prod_{j=0}^n \int_0^{\infty} \frac{d\beta'_j}{\beta'_j} e^{-\xi\beta'_j} \sum_{g=0}^{\infty} g_s^{2g-2+n+m} \tag{2.111} \\
&\quad \times \prod_{j=1}^n \int_0^{\infty} b'_j db'_j Z_{\text{trumpet}}(\beta'_j, b'_j) \prod_{i=1}^m \int_0^{\infty} b_i db_i Z_{\text{trumpet}}(\beta_i, b_i) V_{g,n+m}(\mathbf{b}', \mathbf{b}) \\
&= \sum_{g,n=0}^{\infty} \frac{g_s^{2g-2+n+m}}{n!} \prod_{j=1}^n \int_0^{\infty} db'_j \mathcal{M}(b'_j) \prod_{i=1}^m \int_0^{\infty} b_i db_i Z_{\text{trumpet}}(\beta_i, b_i) V_{g,n+m}(\mathbf{b}', \mathbf{b}),
\end{aligned}$$

where we have used (2.106) in the first equality and (2.107) in the last equality. Note that the factor b of the integration measure bdb is canceled out by $1/b$ in (2.107). To summarize, we can introduce the FZZT anti-brane by gluing the factor $\mathcal{M}(b)$ along the geodesic boundary of the WP volume and integrating over b with the integration measure db . The factor $\mathcal{M}(b)$ in (2.109) has the form

$$\mathcal{M}(b) = e^{-S_{\text{particle}}}, \tag{2.112}$$

where the ‘‘particle action’’ S_{particle} is given by

$$S_{\text{particle}} = zb = (\text{mass}) \times (\text{length of worldline}). \tag{2.113}$$

Namely, $\mathcal{M}(b)$ can be interpreted as the contribution of a particle with mass z running around the geodesic boundary with length b .

We can generalize the above formalisms to the multiple FZZT anti-branes. Let us consider the multiple FZZT anti-branes

$$\prod_i \det(\xi_i + H)^{-1} = \exp \left[\sum_i \int_0^{\infty} \frac{d\beta}{\beta} e^{-\xi_i \beta} Z(\beta) \right], \tag{2.114}$$

where we have used the integral transformation (2.106). The connected correlator with the multiple FZZT anti-branes are given by (2.111) with $\mathcal{M}(b)$ replaced by

$$\mathcal{M}(b) = \sum_i e^{-z_i b}, \tag{2.115}$$

where $\xi_i = z_i^2/2$. In particular, the connected correlator (2.111) with the end of the world (EOW) branes is obtained in [49], which is given by replacing $\mathcal{M}(b)$ by

$$\mathcal{M}(b) = \frac{e^{-\mu b}}{2 \sinh \frac{b}{2}} = \sum_{n=0}^{\infty} e^{-(\mu+n+\frac{1}{2})b}. \tag{2.116}$$

It can be interpreted as the insertion of infinitely many FZZT anti-branes with a particular set of parameters $z_n = \mu + n + \frac{1}{2}$ ($n \geq 0$). We will use this relation in section 3.1. Note that the EOW brane factor (2.116) diverges at $b = 0$ and a certain regularization is required to define the EOW brane. On the other hand, the factor of FZZT anti-brane (2.109) do not contain such a pole and $\mathcal{M}(b)$ for the FZZT anti-brane is well-defined.

2.3.2 Back-reaction of branes

In this subsection, we explore the effects of the insertion of the FZZT anti-branes in JT gravity. The insertion of FZZT anti-branes amounts to the shift of the couplings $\{t_k\}$ of the topological gravity. We call this effect the “back-reaction” of the branes. To see this, let us consider the connected correlator of the multiple FZZT anti-branes without macroscopic loops in (2.111)

$$\left\langle \prod_i \det(\xi_i + H) \right\rangle_{\text{conn.}} = \sum_{g,n=0}^{\infty} \frac{g_s^{2g-2+n}}{n!} \prod_{j=1}^n \int_0^{\infty} db_j \mathcal{M}(b_j) V_{g,n}(\mathbf{b}, \{t_k\}), \quad (2.117)$$

where $\mathcal{M}(b)$ is the brane factor in (2.115) and $V_{g,n}(\mathbf{b}, \{t_k\})$ is the generalized WP volume for general topological gravity. As discussed in [17], $V_{g,n}(\mathbf{b}, \{t_k\})$ can be obtained by

$$V_{g,n}(\mathbf{b}, \{t_k\}) = V(b_1) \cdots V(b_n) F(\{t_k\}), \quad (2.118)$$

where the volume operator $V(b)$ is defined by

$$V(b) = \sum_{k=0}^{\infty} \frac{b^{2k}}{2^k k!} \partial_k. \quad (2.119)$$

The volume operator $V(b)$ is related to the boundary creation operator $B(\beta)$ in (2.69) by the following integral transformation

$$B(\beta) = g_s \int_0^{\infty} b db Z_{\text{trumpet}}(\beta, b) V(b). \quad (2.120)$$

Here we have a relation

$$\int_0^{\infty} db \mathcal{M}(b) V(b) = \sum_{k=0}^{\infty} \sum_i (2k-1)!! z_i^{-2k-1} \partial_k, \quad (2.121)$$

which can be obtained by repeating the integration by parts. Using this formula, the connected correlator (2.117) becomes

$$\begin{aligned}
\left\langle \prod_i \det(\xi_i + H) \right\rangle_{\text{conn.}} &= \sum_{n=0}^{\infty} \frac{1}{n!} \left(\sum_{k=0}^{\infty} \sum_i g_s(2k-1)!! z_i^{-2k-1} \partial_k \right)^n F(\{t_k\}) \\
&= \exp \left(\sum_{k=0}^{\infty} \sum_i g_s(2k-1)!! z_i^{-2k-1} \partial_k \right) F(\{t_k\}) \\
&= F(\{\tilde{t}_k\}),
\end{aligned} \tag{2.122}$$

where the couplings \tilde{t}_k are defined by

$$\tilde{t}_k = t_k + g_s(2k-1)!! \sum_i z_i^{-2k-1}. \tag{2.123}$$

Thus, the insertion of FZZT anti-branes amounts to the shift of couplings $\{t_k\}$ of the topological gravity. In particular, if we consider K FZZT anti-branes with a common parameter $\xi_i = \xi$, the couplings in (2.123) become

$$\tilde{t}_k = t_k + t(2k-1)!!(2\xi)^{-k-\frac{1}{2}}, \tag{2.124}$$

where we have used the relation $\xi = \frac{1}{2}z^2$ and denote $t \equiv g_s K$ which we refer to as the 't Hooft coupling in later chapters. We will use this set of couplings (2.124) to obtain the eigenvalue density of JT gravity with FZZT anti-branes.

Deformation of eigenvalue density

We will see that the leading order eigenvalue density $\rho_0(E)$ in (2.102) is deformed from the original one in (2.103) due to the shift of the couplings (2.124). This deformation is crucial to obtain the late time decreasing behavior of the Page curve in section 3.2 and of the refined Rényi negativity in section 4.3. The function $f(u)$ in (2.89) for the shifted couplings (2.124) and for the JT gravity background $t_k = \gamma_k$ in (2.52) is given by

$$f(u) = \sqrt{u} J_1(2\sqrt{u}) - \frac{t}{\sqrt{2(\xi - u)}}, \tag{2.125}$$

where $J_\alpha(x)$ denotes the Bessel function and we have used the following expression

$$J_\alpha(x) = \sum_{k=0}^{\infty} \frac{(-1)^k}{k!(k+\alpha+1)!} \left(\frac{x}{2}\right)^{2k+\alpha}. \tag{2.126}$$

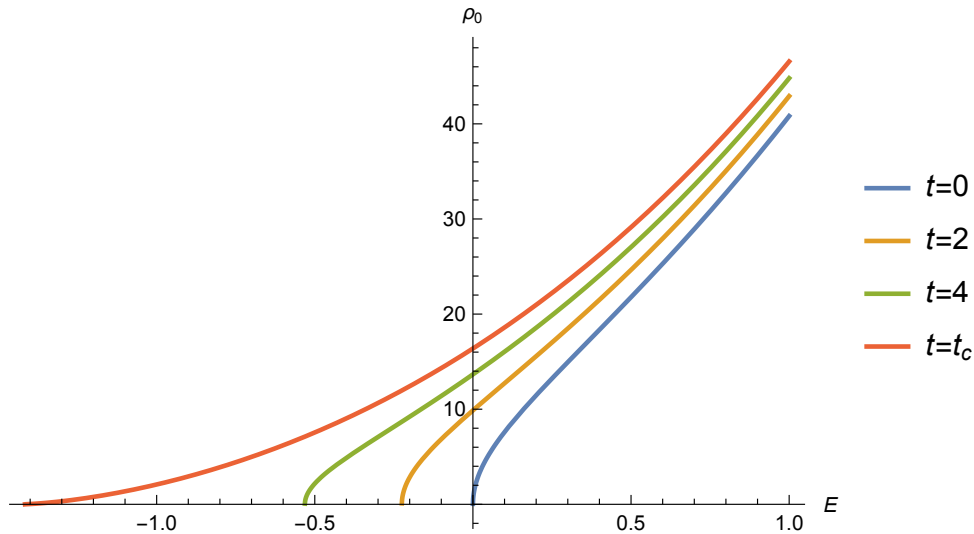


Figure 2.7: The eigenvalue density $\rho_0(E)$ in (2.127) for JT gravity with FZZT anti-branes. We set $g_s = 1/50$, $\xi = 50$ in this figure.

Plugging (2.125) into (2.102), the leading order eigenvalue density of JT gravity with FZZT anti-branes is given by

$$\rho_0(E) = \frac{1}{\sqrt{2\pi}g_s} \left(\int_{E_0}^E dv \frac{I_0(2\sqrt{v})}{\sqrt{E-v}} - \frac{t}{E+\xi} \sqrt{\frac{E-E_0}{2(E_0+\xi)}} \right), \quad (2.127)$$

where $I_k(x)$ is the modified Bessel function of the first kind. The threshold energy E_0 is determined by the genus-zero string equation $f(-E_0) = 0$, or equivalently

$$\sqrt{E_0} I_1(2\sqrt{E_0}) + \frac{t}{\sqrt{2(E_0+\xi)}} = 0. \quad (2.128)$$

The threshold energy is the minimal energy such that $\rho_0(E)$ is supported for $E \geq E_0$. Note that the eigenvalue density (2.127) reduces to the original one (2.103) at $t = 0$ which means that no branes are inserted. We show the eigenvalue density $\rho_0(E)$ in (2.127) for some values of t in Figure 2.7. From Figure 2.7, we can see that the threshold energy E_0 decreases as t increases and the support of $\rho_0(E)$ is shifted to the left. In particular, the original eigenvalue density (2.103) is shown by the curve for $t = 0$ with the threshold energy $E_0 = 0$.

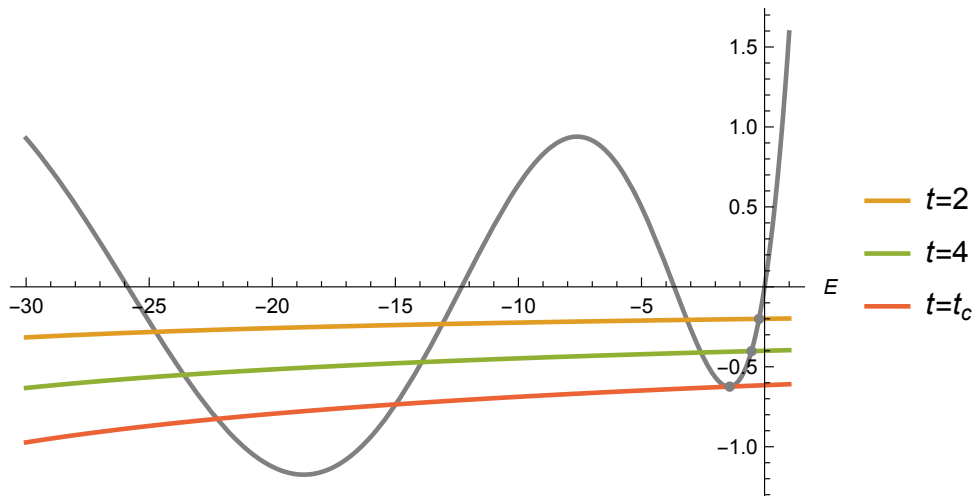


Figure 2.8: The threshold energy E_0 determined by the genus-zero string equation (2.128). We define E_0 as the largest negative solution so that it is continuously deformed from $E_0 = 0$ for $t = 0$. We set $g_s = 1/50, \xi = 50$ in this figure. There is a critical value t_c beyond which the equation (2.128) no longer has any solution.

Phase transition

The threshold energy E_0 is determined by the genus-zero string equation (2.128). Here we show the functions in the equation (2.128) for some values of t in Figure 2.8. The function $\sqrt{E}I_1(2\sqrt{E})$ oscillates for $E < 0$ and monotonically increases for $E > 0$. The function $-t/\sqrt{2(E + \xi)}$ is always negative for $t > 0$. We define E_0 as the largest negative solution of (2.128) so that it is continuously deformed from $E_0 = 0$ for $t = 0$. Then there is a critical value t_c beyond which the equation (2.128) no longer has any solution. It implies a phase transition at $t = t_c$. As discussed in [20], the critical value t_c corresponds to the value beyond which the corresponding dilaton gravity theory no longer has any black hole solution. Thus, the phase transition at $t = t_c$ can be viewed as the end of the black hole evaporation in the model of an evaporating black hole which we review in section 3.2.

Chapter 3

Black hole information paradox

In this chapter, we review the recent progress in the black hole information paradox. It is formulated by calculating the entanglement entropy of the Hawking radiation. The aim of this chapter is to explain the applications of the matrix model of JT gravity to the literature and to prepare the model setup which we use in chapter 4. In particular, we focus on a toy model of an evaporating black hole in JT gravity with end of the world (EOW) branes proposed by Penington, Shenker, Stanford, and Yang (PSSY) [14]. The entanglement entropy of the Hawking radiation follows the unitary Page curve in the PSSY model. Several types of “replica wormholes” contribute to the entropy, and the exchange of dominance of different types of replica wormholes plays the essential role to obtain the Page curve. However, the entanglement entropy approaches a constant value at late time of the black hole evaporation in contrast to the decreasing behavior as shown in Figure 1.2. This result indicates that the back-reaction of the Hawking radiation is not considered in the PSSY model. On the other hand, the late time decreasing behavior of the Page curve is reproduced in another toy model in JT gravity with dynamical FZZT anti-branes, proposed by Okuyama and Sakai [20]. The late time decreasing behavior comes from the deformed eigenvalue density (2.127) due to the back-reaction of branes.

This chapter is organized as follows. Before exploring the applications of the matrix model of JT gravity, we briefly review the entanglement entropy and its Rényi generalizations. In section 3.1, we review the PSSY model and the replica wormholes. In section 3.2, we review the Page curve in the matrix model of JT gravity with dynamical FZZT anti-branes.

Entanglement entropy

For later use we recall the definitions of the entanglement entropy and its Rényi generalizations. For a bipartite quantum system with the Hilbert space $\mathcal{H} = \mathcal{H}_A \otimes \mathcal{H}_B$, the reduced density matrix on the subsystem A is defined by

$$\rho_A = \text{Tr}_B \rho, \quad (3.1)$$

where ρ is the density matrix on the total system AB. The entanglement entropy of the subsystem A is defined by the von Neumann entropy of ρ_A as

$$S_A = -\text{Tr} \rho_A \log \rho_A. \quad (3.2)$$

The entanglement entropy is hard to handle since it includes the logarithm of the density matrix. It is useful to compute the entanglement entropy by using the following replica trick

$$S_A = \lim_{n \rightarrow 1} \frac{1}{1-n} \log (\text{Tr} \rho_A^n) = \lim_{n \rightarrow 1} n^2 \partial_n \left[-\frac{1}{n} \log (\text{Tr} \rho_A^n) \right], \quad (3.3)$$

where the parameter n is called the replica number. Thus, the problem boils down to compute $\text{Tr} \rho_A^n$ in the replica trick. From the middle quantity in (3.3), the Rényi entropy [50, 51] is defined by

$$S_A^{(n)} = \frac{1}{1-n} \log (\text{Tr} \rho_A^n). \quad (3.4)$$

Similarly, the refined Rényi entropy [52] is defined by

$$\tilde{S}_A^{(n)} = n^2 \partial_n \left[-\frac{1}{n} \log (\text{Tr} \rho_A^n) \right] = (1 - n \partial_n) \log (\text{Tr} \rho_A^n). \quad (3.5)$$

Note that there is an analogy between the refined Rényi entropy $\tilde{S}_A^{(n)}$ and the thermodynamic entropy in statistical mechanics by identifying the replica number n with the inverse temperature β . Using this analogy, the capacity of entanglement [53] is defined by

$$\tilde{C}_A^{(n)} = -n \partial_n \tilde{S}_A^{(n)} = n^2 \partial_n^2 \log (\text{Tr} \rho_A^n), \quad (3.6)$$

which is an analogue of the heat capacity. The analogy with statistical mechanics is viewed in Table 4.1. We will define the ‘‘capacity of negativity’’ as an analogue of the capacity of entanglement in section 4.1.

3.1 PSSY model

In this section, we review the relation between the Page curve and the replica wormholes in the matrix model of JT gravity with end of the world (EOW) branes proposed by Penington, Shenker, Stanford, and Yang (PSSY) [14]. We identify the degrees of freedom of the Hawking radiation with the EOW branes. The transition of the Page curve can be understood as the exchange of dominance between the disconnected and the totally connected saddles in the gravitational path integral. The connected saddles are referred to as the “replica wormholes.” However, several types of replica wormholes can contribute around the Page time. Thus, we have to sum over the replica wormholes to investigate the entire Page curve. As we review in subsection 3.1.3 and 3.1.4, the sum over the replica wormholes can be efficiently computed by solving the Schwinger-Dyson equation (3.53). This method is generalized in the case of negativities as we discuss in chapter 4.

3.1.1 Semiclassical description

We first review the semiclassical description of the PSSY model since it is useful to explore which saddles dominate in the calculation of the entanglement entropy. We will see that the disconnected saddle dominates at early time while the totally connected replica wormhole dominates at late time. The exchange of dominance of these saddles leads to the unitary Page curve.

Euclidean action

The PSSY model is defined by JT gravity with EOW branes. We identify the degrees of freedom of the Hawking radiation with the EOW branes. The EOW branes can be regarded as particles of mass μ and the Euclidean action of the PSSY model is defined by

$$I = I_{\text{JT}} + \mu \int_{\text{brane}} ds, \quad (3.7)$$

where the action of JT gravity I_{JT} is given by

$$I_{\text{JT}} = -\frac{S_0}{2\pi} \left(\frac{1}{2} \int_{\Sigma} \sqrt{g} R + \int_{\partial\Sigma} \sqrt{\bar{h}} \tilde{K} \right) - \left(\frac{1}{2} \int_{\Sigma} \sqrt{g} \phi (R + 2) + \int_{\partial\Sigma} \sqrt{\bar{h}} \phi \tilde{K} \right). \quad (3.8)$$

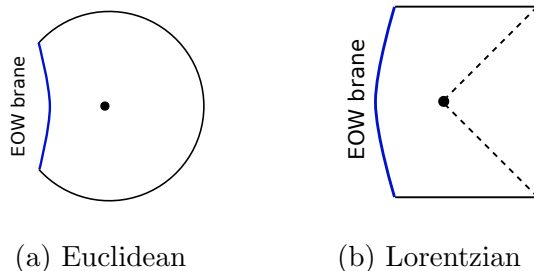


Figure 3.1: The disk geometry with EOW branes in (a) Euclidean and (b) Lorentzian signatures [14].

The first term of (3.8) is equal to $-S_0\chi(\Sigma)$ as we discussed in chapter 2. As we will see later, we consider the gravitational path integral in the calculation of the entanglement entropy. The contributions of surfaces in the gravitational path integral are suppressed by e^{-2S_0} for each additional genus. Thus, the disk geometry gives the dominant contribution. We show the disk geometry with the EOW brane in Figure 3.1. The black and blue curves correspond to the asymptotic boundary and the EOW brane, respectively. We impose different boundary conditions for the asymptotic boundary and the EOW brane, respectively. For the asymptotic boundary of length β , we impose

$$ds^2|_{\partial\Sigma} = \frac{1}{\epsilon^2}d\tau^2, \quad \phi|_{\partial\Sigma} = \frac{1}{\epsilon}, \quad \epsilon \rightarrow 0. \quad (3.9)$$

Here τ is the imaginary time coordinate on the boundary. For the EOW brane, we impose

$$\partial_n\phi = \mu, \quad \tilde{K} = 0, \quad \mu \geq 0, \quad (3.10)$$

where we denote the derivative normal to the EOW branes by ∂_n .

Reduced density matrix

To model the Hawking radiation, we consider a bipartite quantum system with the Hilbert space $\mathcal{H} = \mathcal{H}_{\text{BH}} \otimes \mathcal{H}_{\text{R}}$. The dimensions of the subsystems are defined by

$$\dim \mathcal{H}_{\text{BH}} = e^{S_0}, \quad \dim \mathcal{H}_{\text{R}} = K, \quad (3.11)$$

where we define $\dim \mathcal{H}_{\text{BH}}$ so that $S_0 = \log(\dim \mathcal{H}_{\text{BH}})$. Here \mathcal{H}_{R} corresponds to the auxiliary “radiation” system which is maximally entangled with the

EOW branes. We will regard K as “time” since more Hawking radiation are emitted as time goes. We are particularly interested in the entanglement structure for large dimensions of the subsystems with the ratio $t \equiv Ke^{-S_0}$ fixed. We take the planar approximation in this limit. That is, we will ignore the all higher-order corrections in e^{-S_0} and K^{-1} .

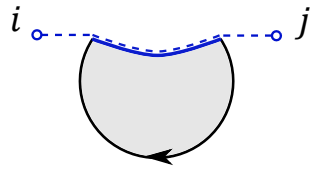
We assume that the interior and the exterior partners of the early Hawking radiation are maximally entangled. Thus, the state of the total system is defined by the following pure state

$$|\Psi\rangle = \mathcal{N} \sum_{i=1}^K |\psi_i\rangle_{\text{BH}} \otimes |i\rangle_{\text{R}}, \quad (3.12)$$

where $|\psi_i\rangle_{\text{BH}}$ is regarded as the black hole microstate with the EOW brane in state i , and $\{|i\rangle_{\text{R}}\}_{i=1}^K$ forms a orthonormal basis of \mathcal{H}_{R} . The normalization factor \mathcal{N} is determined so that the norm $\langle\Psi|\Psi\rangle = 1$. The reduced density matrix $\rho_{\text{R}} = \text{Tr}_{\text{BH}}|\Psi\rangle\langle\Psi|$ on the radiation system is given by

$$\rho_{\text{R}} = \sum_{i=1}^K |j\rangle\langle i|_{\text{R}} \langle\psi_i|\psi_j\rangle_{\text{BH}}. \quad (3.13)$$

Here we have included the normalization factor \mathcal{N} in the definition of $|\psi_i\rangle_{\text{BH}}$ for notational simplicity. The amplitude $\langle\psi_i|\psi_j\rangle_{\text{BH}}$ can be calculated by the gravitational path integral. As discussed above, the leading contributions are given by the disk geometries. Thus, the amplitude $\langle\psi_i|\psi_j\rangle_{\text{BH}}$ at leading order is represented by the following diagram [14],



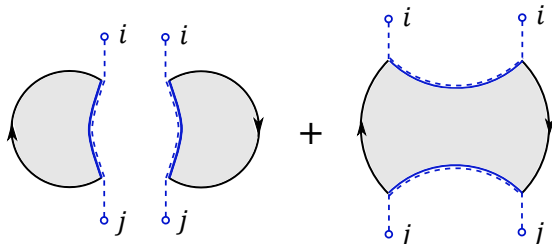
where the black thick curve corresponds to the asymptotic boundary of the two-dimensional spacetime with the length β , while the blue thick curve corresponds to the EOW brane. The amplitude is proportional to δ_{ij} since the same EOW brane links the two indices i and j which are associated with the orthonormal basis of \mathcal{H}_{R} .

Dominant saddles

We are particularly interested in the n -th moment $\text{Tr}(\rho_{\text{R}}^n)$ to calculate the entanglement entropy by using the replica trick (3.3). First let us consider the second moment $\text{Tr}(\rho_{\text{R}}^2)$ called “purity” as an example,

$$\text{Tr}(\rho_{\text{R}}^2) = \sum_{i,j=1}^K |\langle \psi_i | \psi_j \rangle_{\text{BH}}|^2. \quad (3.15)$$

In this case, there are two leading saddles which satisfy the boundary conditions. As with (3.14), we can diagrammatically represent the leading saddles of $|\langle \psi_i | \psi_j \rangle_{\text{BH}}|^2$ by the following diagrams [14],



$$(3.16)$$

where we call the first term “disconnected” saddle and the second term “connected” saddle, respectively. The connected saddle is a kind of replica wormholes. Here the disconnected saddle gives $\delta_{ij}\delta_{ij} = \delta_{ij}$ while the connected one gives $\delta_{ii}\delta_{jj} = 1$ from the linking by the EOW branes. Thus, the disconnected and the connected saddles give K and K^2 contributions in (3.15), respectively. This can be diagrammatically represented by drawing the loops of the blue dashed curves in (3.16). Each of the index loops gives K contribution. Now the purity (3.15) is given by

$$\text{Tr}(\rho_{\text{R}}^2) = \frac{KZ_1^2 + K^2Z_2}{(KZ_1)^2} = \frac{1}{K} + \frac{Z_2}{Z_1^2}, \quad (3.17)$$

where Z_n denotes the contribution of the disk surrounded by n asymptotic boundaries and n EOW branes. Here we have restored the normalization factor. We can roughly estimate the path integral $Z_n \sim e^{S_0}$ since the topology of Z_n is the disk. Then the purity (3.17) can be estimated by

$$\text{Tr}(\rho_{\text{R}}^2) \sim \frac{1}{K} + e^{-S_0}. \quad (3.18)$$

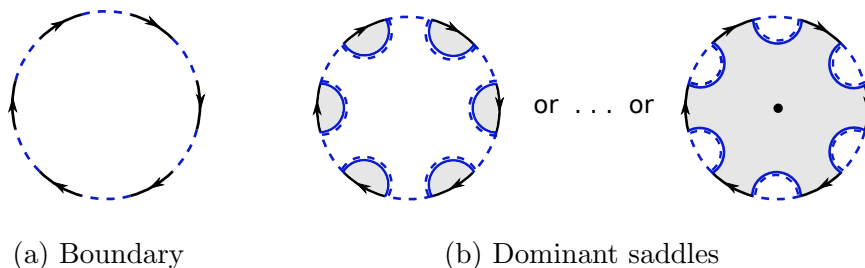


Figure 3.2: (a) The boundary condition and (b) the dominant saddles for the n -th moment $\text{Tr}(\rho_{\text{R}}^n)$ with $n = 6$ as an example [14]. We only show the completely disconnected and connected saddles here.

Thus, the disconnected saddle dominates for $K \ll e^{S_0}$ while the connected one dominates $K \gg e^{S_0}$. This exchange of dominance between the disconnected and the connected saddles is essential to obtain the Page curve.

Next we consider the general n -th moment $\text{Tr}(\rho_{\text{R}}^n)$. There are several types of geometries which satisfies the boundary conditions. Here we show the boundary condition and relevant saddles for $\text{Tr}(\rho_{\text{R}}^n)$ in Figure 3.2. The circular diagrams in Figure 3.2 come from the trace over the index associated to the radiation system. As with the purity, the completely disconnected saddle dominates for $K \ll e^{S_0}$. The contribution is given by n disks of Z_1 and single index loop K as

$$\text{Tr}(\rho_{\text{R}}^n)|_{\text{disconn.}} = \frac{K Z_1^n}{(K Z_1)^n} = \frac{1}{K^{n-1}}. \quad (3.19)$$

On the other hand, the totally connected saddle dominates for $K \gg e^{S_0}$. The contribution is given by single disk of Z_n and n index loops K^n as

$$\text{Tr}(\rho_{\text{R}}^n)|_{\text{totally conn.}} = \frac{K^n Z_n}{(K Z_1)^n} = \frac{Z_n}{Z_1^n}. \quad (3.20)$$

Here (3.20) is purely gravitational and it gives the thermodynamic entropy of the black hole. The entanglement entropy can be calculated by using the replica trick (3.3) in these extreme limits as

$$S_{\text{R}} = \begin{cases} \log K & (K \ll e^{S_0}), \\ S_{\text{BH}} & (K \gg e^{S_0}), \end{cases} \quad (3.21)$$

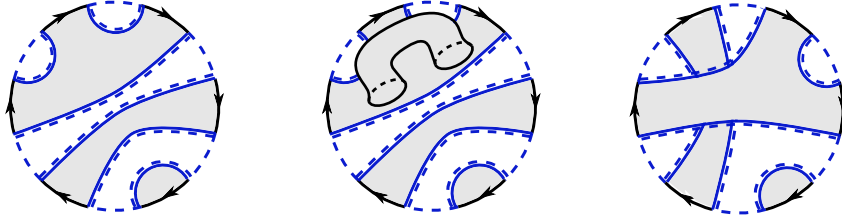


Figure 3.3: Possible geometries which satisfy the boundary condition 3.2a [14]. We will consider only the left diagram in the planar limit.

where we define the thermodynamic entropy of the black hole by

$$S_{\text{BH}} \equiv \lim_{n \rightarrow 1} \left(\frac{1}{1-n} \log \frac{Z_n}{Z_1^n} \right). \quad (3.22)$$

Thus, we conclude that the Page curve comes from the exchange of dominance between the completely disconnected saddle and the totally connected replica wormhole in the path integral of JT gravity.

Other possible geometries

We have considered the dominant saddles only in the extreme limits $K \ll e^{S_0}$ and $K \gg e^{S_0}$. However, several partially connected replica wormholes can dominate in the intermediate regime between $K \ll e^{S_0}$ and $K \gg e^{S_0}$. In the planar limit, we ignore the all higher order corrections in e^{-S_0} and K^{-1} . Then the possible geometries are represented by the planar diagrams. To verify this claim, we show some examples which satisfy the boundary condition in Figure 3.3. These are examples of $n = 6$ including Z_1, Z_2, Z_3 configurations. As discussed above, the middle diagram has an extra handle and the contribution is suppressed by e^{-2S_0} compared to the left one. The crossing in the right diagram reduces the index loops, and the contribution is suppressed by K^{-2} compared to the left one. Thus, we only consider the planar diagrams at leading order in the planar limit.

Actually, we have to sum over all planar diagrams since all of them can contribute in the intermediate regime between $K \ll e^{S_0}$ and $K \gg e^{S_0}$. We can perform the sum efficiently by using the resolvent trick reviewed in subsection 3.1.3. In the next subsection, we describe the PSSY model in terms of the matrix model of JT gravity. We will see that the sum over the replica wormholes comes from the ensemble average of the matrix integral.

3.1.2 Matrix model description

In this subsection, we describe the PSSY model in terms of the matrix model of JT gravity. As discussed in chapter 2, the path integral of JT gravity corresponds to the matrix integral. We will see that the sum over the replica wormholes comes from the ensemble average of the matrix integral. As we discussed in section 2.3, the EOW brane corresponds to infinitely many FZZT anti-branes with a particular set of parameters $\xi_n = \frac{1}{2}(\mu + n + \frac{1}{2})^2$ ($n \geq 0$). Thus, the matrix integral with K EOW branes is defined by

$$\begin{aligned} Z &= \int dH e^{-\text{Tr}V(H)} \left[\prod_{n=0}^{\infty} \det(\xi_n + H)^{-1} \right]^K \\ &= \int dH dQ dQ^\dagger e^{-\text{Tr}V(H) - \text{Tr}Q^\dagger [\prod_{n=0}^{\infty} (\xi_n + H)] Q}, \end{aligned} \quad (3.23)$$

where H and Q are $N \times N$ Hermitian and $N \times K$ complex matrices, respectively. We can introduce the genus counting parameter g_s by rescaling the matrix potential as

$$\frac{1}{g_s} V(H), \quad (3.24)$$

so that the genus expansion is manifest. We consider the double-scaling limit of this matrix integral. We further take the following 't Hooft limit

$$K \rightarrow \infty, \quad g_s \rightarrow 0 \quad \text{with } t \equiv g_s K \text{ fixed.} \quad (3.25)$$

In this limit, we compute all quantities in the planar approximation. That is, we will ignore all higher-order corrections in g_s and K^{-1} .

Black hole microstates

Following the appendix D of [14], we define the microstates of the black hole. We consider a bipartite quantum system of the black hole and the Hawking radiation with the Hilbert space $\mathcal{H} = \mathcal{H}_{\text{BH}} \otimes \mathcal{H}_{\text{R}}$ with the dimensions of

$$\dim \mathcal{H}_{\text{BH}} = N, \quad \dim \mathcal{H}_{\text{R}} = K. \quad (3.26)$$

We assume that the total system is in a pure state $|\Psi\rangle$ in which the black hole microstates $|\psi_i\rangle$ and the radiation states $|i\rangle$ are maximally entangled

$$|\Psi\rangle = \frac{1}{\sqrt{\text{Tr}W}} \sum_{i=1}^K |\psi_i\rangle \otimes |i\rangle. \quad (3.27)$$

We omit the label BH and R of the states for notational simplicity. Here we denote the “flavor” degrees of freedom for the interior partners of the early Hawking radiation by the label $i, j = 1, \dots, K$, and $\{|i\rangle\}_{i=1}^K$ forms the orthonormal basis of \mathcal{H}_R . The matrix W is defined by the overlap of the black hole microstates

$$W_{ij} \equiv \langle \psi_i | \psi_j \rangle. \quad (3.28)$$

Note that $|\Psi\rangle$ is normalized as $\langle \Psi | \Psi \rangle = 1$. The reduced density matrix $\rho = \text{Tr}_{\text{BH}} |\Psi\rangle\langle \Psi|$ of the Hawking radiation is defined by

$$\rho = \frac{1}{\text{Tr} W} \sum_{i,j=1}^K |i\rangle\langle j| \langle \psi_j | \psi_i \rangle. \quad (3.29)$$

Then the matrix elements can be read off as

$$\rho_{ij} = \frac{W_{ji}}{\text{Tr} W}. \quad (3.30)$$

The microstates of the black hole can be approximated by the canonical thermal pure quantum state [54, 55]

$$|\psi_i\rangle = \sum_a e^{-\frac{1}{2}\beta H} |a\rangle Q_{ai} = \sum_{a,b} |b\rangle \left(e^{-\frac{1}{2}\beta H} \right)_{ba} Q_{ai}, \quad (3.31)$$

where the inverse temperature β is identified with the length of the asymptotic boundary of JT gravity. We define the matrix element H_{ab} as

$$H_{ab} = \langle a | H | b \rangle, \quad (3.32)$$

where we denote the “color” degrees of freedom for the bulk gravity by the label $a, b = 1, \dots, N$, and $\{|a\rangle\}_{a=1}^N$ forms the orthonormal basis of \mathcal{H}_{BH} .

Ensemble average

Here we explain the ensemble average in the matrix integral (3.23). We will see that the sum over replica wormholes comes from the ensemble average. It is convenient to change the random variables Q as

$$Q_{ai} = \left[\prod_{n=0}^{\infty} (\xi_n + H) \right]^{-\frac{1}{2}} C_{ai} = \Gamma(\mu - \frac{1}{2} + i\sqrt{2H}) C_{ai}, \quad (3.33)$$

so that the new random variable C obeys the Gaussian distribution. The Gamma function comes from the infinite product of the brane factor with an appropriate regularization. Then the matrix integral (3.23) becomes

$$Z = \int dH dC dC^\dagger J(H) e^{-\text{Tr}V(H) - \text{Tr}C^\dagger C}, \quad (3.34)$$

where $J(H)$ comes from the integration measure associated with the transformation (3.33) as

$$J(H) = \left[|\Gamma(\mu - \frac{1}{2} + i\sqrt{2H})|^2 \right]^K. \quad (3.35)$$

The ensemble average of an operator \mathcal{O} is defined by

$$\langle \overline{\mathcal{O}} \rangle = \frac{1}{Z} \int dH dC dC^\dagger J(H) e^{-\text{Tr}V(H) - \text{Tr}C^\dagger C} \mathcal{O}, \quad (3.36)$$

where the angle bracket $\langle \mathcal{O} \rangle$ represents the averaging over the color degrees of freedom while the overline $\overline{\mathcal{O}}$ represents the averaging over the flavor degrees of freedom. In particular, the averaging over the flavor degrees of freedom can be computed by the Wick contraction since C obeys the Gaussian distribution. In the PSSY model, we take the ‘‘probe brane’’ approximation such that we ignore $J(H)$ in the matrix integral as

$$Z = \int dH dC dC^\dagger e^{-\text{Tr}V(H) - \text{Tr}C^\dagger C}. \quad (3.37)$$

On the other hand, the black hole microstates (3.31) also change by the transformation (3.33) as

$$|\psi_i\rangle = \sum_{a,b} |b\rangle \left[e^{-\frac{1}{2}\beta H} \Gamma(\mu - \frac{1}{2} + i\sqrt{2H}) \right]_{ba} C_{ai} = \sum_{a,b} |b\rangle (\sqrt{A})_{ba} C_{ai}, \quad (3.38)$$

where $A(H)$ is defined by

$$A(H) = e^{-\beta H} |\Gamma(\mu - \frac{1}{2} + i\sqrt{2H})|^2. \quad (3.39)$$

Let us consider the overlaps such as

$$\begin{aligned} \langle \psi_i | \psi_j \rangle &= \sum_{a,b} A_{ab} C_{ai}^* C_{bj}, \\ |\langle \psi_i | \psi_j \rangle|^2 &= \sum_{a,b,a',b'} A_{ab} A_{b'a'} C_{ai}^* C_{bj} C_{a'i} C_{b'j}^*. \end{aligned} \quad (3.40)$$

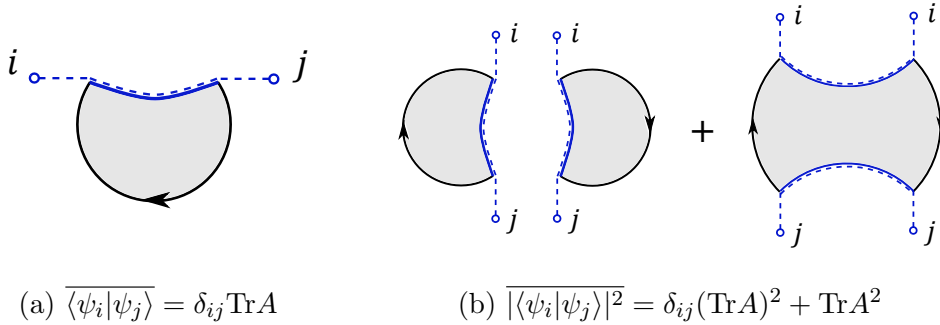


Figure 3.4: Diagrammatic representations of the averaged overlaps in (3.42). (a) and (b) correspond to $\overline{\langle \psi_i | \psi_j \rangle}$ and $\overline{|\langle \psi_i | \psi_j \rangle|^2}$, respectively.

The averaging over C can be computed by the Wick contraction

$$\begin{aligned} \overline{C_{ai}^* C_{bj}} &= \delta_{ab} \delta_{ij}, \\ \overline{C_{ai}^* C_{bj} C_{a'i} C_{b'j}^*} &= \delta_{ab} \delta_{a'b'} \delta_{ij} + \delta_{aa'} \delta_{bb'}. \end{aligned} \quad (3.41)$$

By using these formulas, the average of the overlaps (3.40) are given by

$$\begin{aligned} \overline{\langle \psi_i | \psi_j \rangle} &= \delta_{ij} \text{Tr} A, \\ \overline{|\langle \psi_i | \psi_j \rangle|^2} &= \delta_{ij} (\text{Tr} A)^2 + \text{Tr} A^2. \end{aligned} \quad (3.42)$$

As discussed in [14], one can visualize the above computations by drawing diagrams. For instance, the overlap $\langle \psi_i | \psi_j \rangle$ in (3.40) can be represented by the following diagram

$$\langle \psi_i | \psi_j \rangle = (C^\dagger A C)_{ij} = \begin{array}{c} i \quad (C^\dagger)_{ia} \quad \xrightarrow{A_{ab}} \quad C_{bj} \quad j \\ \text{---} \text{---} \text{---} \end{array} \quad (3.43)$$

The black thick curve labeled by the color matrix A_{ab} corresponds to the asymptotic boundary of the two-dimensional spacetime while the blue dashed curve labeled by the flavor matrix C_{ia} corresponds to the flavor degrees of freedom. The averaged overlaps in (3.42) are represented by the diagrams in Figure 3.4. The blue thick curves correspond to the EOW branes connecting the same flavor indices. The gray disks correspond to $\text{Tr} A^n$ which are surrounded by n asymptotic boundaries and n EOW branes. As seen from equation (3.42) and Figure 3.4b, the sum over replica wormholes comes from the ensemble average in the matrix integral.

3.1.3 Resolvent trick

We consider $\langle \overline{\text{Tr} \rho^n} \rangle$ to compute the entanglement entropy by using the replica trick. The reduced density matrix of the Hawking radiation is given by (3.30). In the planar limit, we can take the average of the numerator and the denominator independently

$$\overline{\text{Tr} \rho^n} \approx \frac{\overline{\text{Tr} W^n}}{(\overline{\text{Tr} W})^n} = \frac{\overline{\text{Tr} W^n}}{(K \text{Tr} A)^n}. \quad (3.44)$$

The numerator can be computed by the Wick contraction, and it boils down to the sum over the all combinations of C^\dagger and C . In the diagrammatic representation, this corresponds to connecting the all combinations of the flavor indices by the EOW branes. To compute this sum efficiently we can use the resolvent trick [14]. First let us define the resolvent matrix by

$$R_{ij}(\lambda) = \left(\frac{1}{\lambda \mathbf{1} - \rho} \right)_{ij} = \frac{1}{\lambda} \delta_{ij} + \sum_{n=1}^{\infty} \frac{1}{\lambda^{n+1}} (\rho^n)_{ij}. \quad (3.45)$$

We also define the resolvent by the trace of the resolvent matrix

$$R(\lambda) = \text{Tr} R_{ij}(\lambda) = \frac{K}{\lambda} + \sum_{n=1}^{\infty} \frac{1}{\lambda^{n+1}} \text{Tr} \rho^n. \quad (3.46)$$

By above definition $R(\lambda)$ is a generating function of the moment $\text{Tr} \rho^n$. Using the diagrammatic representation (3.43), $R_{ij}(\lambda)$ is represented by [14]

$$\text{---} \circlearrowleft \text{---} = \text{---} + \text{---} \leftarrow \text{---} + \text{---} \leftarrow \leftarrow \text{---} + \dots \quad (3.47)$$

Here each dashed blue line is weighted by $1/\lambda$ and carries the flavor index. The average over the flavor degrees of freedom in the planar approximation leads to the following Schwinger-Dyson equation [14]:

$$\text{---} \circlearrowleft \text{---} = \text{---} + \text{---} \leftarrow \text{---} \circlearrowleft \text{---} + \text{---} \leftarrow \leftarrow \text{---} \circlearrowleft \text{---} \leftarrow \text{---} \circlearrowleft \text{---} + \dots \quad (3.48)$$

Each dashed blue loop associated to the flavor index gives $K = \text{Tr}\delta_{ij}$ contribution. The gray disk surrounded by n asymptotic boundaries and n EOW branes gives $\text{Tr}A^n$ contribution. Thus, the diagrammatic equation (3.48) is equivalent to

$$R_{ij}(\lambda) = \frac{1}{\lambda}\delta_{ij} + \frac{1}{\lambda} \sum_{n=1}^{\infty} \frac{\text{Tr}A^n}{(K\text{Tr}A)^n} R(\lambda)^{n-1} R_{ij}(\lambda). \quad (3.49)$$

Here we omit the overline which denotes the flavor average for simplicity. Taking the trace, we get the Schwinger-Dyson equation for the resolvent

$$\lambda R(\lambda) = K + \sum_{n=1}^{\infty} \frac{R(\lambda)^n \text{Tr}A^n}{(K\text{Tr}A)^n}. \quad (3.50)$$

Further we take the average over the color degrees of freedom. In the planar approximation, we can take the average of the numerator and the denominator independently. The Schwinger-Dyson equation (3.50) becomes

$$\lambda R(\lambda) = K + \sum_{n=1}^{\infty} \frac{R(\lambda)^n Z_n}{(K Z_1)^n}, \quad (3.51)$$

where we define Z_n by

$$Z_n \equiv \langle \text{Tr}A^n \rangle = \int_0^{\infty} dE \rho_0^{\text{JT}}(E) A(E)^n. \quad (3.52)$$

Here $\rho_0^{\text{JT}}(E)$ is the original leading order eigenvalue density (2.103). Plugging this into (3.51), we get

$$\begin{aligned} \lambda R(\lambda) &= K + \sum_{n=1}^{\infty} \frac{R(\lambda)^n}{(K Z_1)^n} \int_0^{\infty} dE \rho_0^{\text{JT}}(E) A(E)^n \\ &= K + \int_0^{\infty} dE \rho_0^{\text{JT}}(E) \sum_{n=1}^{\infty} \left[\frac{R(\lambda) A(E)}{K Z_1} \right]^n \\ &= K + \int_0^{\infty} dE \rho_0^{\text{JT}}(E) \frac{w(E) R(\lambda)}{K - w(E) R(\lambda)}, \end{aligned} \quad (3.53)$$

where $w(E)$ is defined by

$$w(E) = \frac{A(E)}{Z_1}. \quad (3.54)$$

To summarize, the resolvent $R(\lambda)$ is a generating function of $\text{Tr}\rho^n$ and obeys the Schwinger-Dyson equation (3.53). Thus, we can compute the entanglement entropy by solving (3.53) as we discuss in the next subsection.

3.1.4 Entanglement spectrum

We compute the entanglement entropy by solving the Schwinger-Dyson equation (3.53) approximately. We define the eigenvalue density of ρ by

$$D(\lambda) = \sum_i \delta(\lambda - \lambda_i), \quad (3.55)$$

where λ_i 's are the eigenvalues of ρ . $D(\lambda)$ is also referred to as the entanglement spectrum. Using $D(\lambda)$, the entanglement entropy is computed by

$$S = - \int_0^\infty d\lambda D(\lambda) \lambda \log \lambda. \quad (3.56)$$

As one can immediately check, $D(\lambda)$ can be computed from $R(\lambda)$ by taking the discontinuity across the real axis

$$D(\lambda) = \lim_{\epsilon \rightarrow 0} \frac{R(\lambda - i\epsilon) - R(\lambda + i\epsilon)}{2\pi i}. \quad (3.57)$$

Following [14], let us solve the Schwinger-Dyson equation (3.53) approximately. First we approximate the integral in (3.53) as

$$\lambda R(\lambda) \approx K + \int_0^{E_K} dE \rho_0^{\text{JT}}(E) \frac{w(E)R(\lambda)}{K - w(E)R(\lambda)} + \lambda_0 R(\lambda), \quad (3.58)$$

where λ_0 and E_K are defined by

$$\lambda_0 = \frac{1}{K} \int_{E_K}^\infty dE \rho_0^{\text{JT}}(E) w(E), \quad (3.59)$$

$$K = \int_0^{E_K} dE \rho_0^{\text{JT}}(E). \quad (3.60)$$

In the approximation, we have assumed $K \geq |w(E)R(\lambda)|$ for $E \geq E_K$ since $w(E)$ is a decreasing function of E . Rewriting (3.58) as

$$R(\lambda) = \frac{K}{\lambda - \lambda_0} + \frac{1}{\lambda - \lambda_0} \int_0^{E_K} dE \rho_0^{\text{JT}}(E) \frac{w(E)R(\lambda)}{K - w(E)R(\lambda)}, \quad (3.61)$$

we can solve $R(\lambda)$ by using the iteration starting from

$$R(\lambda) = \frac{K}{\lambda - \lambda_0}. \quad (3.62)$$

Plugging this into $R(\lambda)$ in (3.61) and using (3.60), we obtain

$$\begin{aligned} R(\lambda) &= \frac{1}{\lambda - \lambda_0} \left[\int_0^{E_K} dE \rho_0^{\text{JT}}(E) + \int_0^{E_K} dE \rho_0^{\text{JT}}(E) \frac{w(E)}{\lambda - \lambda_0 - w(E)} \right] \\ &= \int_0^{E_K} dE \rho_0^{\text{JT}}(E) \frac{1}{\lambda - \lambda_0 - w(E)}. \end{aligned} \quad (3.63)$$

By taking the discontinuity (3.57), the entanglement spectrum is given by

$$D(\lambda) = \int_0^{E_K} dE \rho_0^{\text{JT}}(E) \delta(\lambda - \lambda_0 - w(E)). \quad (3.64)$$

Note that $D(\lambda)$ obeys the correct normalization conditions

$$\int_0^\infty d\lambda D(\lambda) = \int_0^{E_K} dE \rho_0^{\text{JT}}(E) = K, \quad (3.65)$$

$$\int_0^\infty d\lambda D(\lambda) \lambda = \int_0^{E_K} dE \rho_0^{\text{JT}}(E) (\lambda_0 + w(E)) = 1, \quad (3.66)$$

where we have used (3.59) and (3.60). The latter condition (3.66) corresponds to $\text{Tr} \rho = 1$. Finally, the entanglement entropy (3.56) can be computed by

$$S = - \int_0^{E_K} dE \rho_0^{\text{JT}}(E) (\lambda_0 + w(E)) \log(\lambda_0 + w(E)). \quad (3.67)$$

We can numerically compute the entanglement entropy as a function of K by using this result. One can find that the entanglement entropy follows the Page curve by regarding K as “time.” See also Figure 7 of [14] for the original result. However, it approaches a constant value at late time of the black hole evaporation in contrast to the decreasing behavior in Figure 1.2. This result indicates that the back-reaction of the Hawking radiation is not considered in the PSSY model. In the next section, we review a slightly generalized model in JT gravity with dynamical FZZT anti-branes, in which the late time decreasing behavior of the Page curve is reproduced by including the back-reaction of branes based on the formalisms discussed in section 2.3.

3.2 Page curve from dynamical branes

In this section, we review a generalized model in the matrix model of JT gravity with dynamical FZZT anti-branes [20]. As we discussed in section

2.3, the eigenvalue density of JT gravity is deformed by the the back-reaction of branes. Then, the entanglement entropy monotonically decreases at late time of the black hole evaporation in contrast to the PSSY model.

3.2.1 Matrix integral with FZZT anti-branes

We consider the matrix integral with K FZZT anti-branes instead of the EOW branes of (3.23) in the PSSY model such as

$$\begin{aligned} Z &= \int dH e^{-\text{Tr}V(H)} \det(\xi + H)^{-K} \\ &= \int dH dQ dQ^\dagger e^{-\text{Tr}V(H) - \text{Tr}Q^\dagger(\xi + H)Q}, \end{aligned} \quad (3.68)$$

where we set the parameter ξ to be common to all K branes for simplicity. We also describe the black hole microstates by (3.31), but change the random variable Q differently from (3.33) as

$$Q = (\xi + H)^{-\frac{1}{2}} C. \quad (3.69)$$

Then the matrix integral (3.68) becomes

$$Z = \int dH dC dC^\dagger \det(\xi + H)^{-K} e^{-\text{Tr}V(H) - \text{Tr}C^\dagger C}, \quad (3.70)$$

where the determinant factor comes from the integration measure associated with the transformation (3.69). The ensemble average over C can be computed by using the Wick contraction since C obeys the Gaussian distribution. In this case, the black hole microstates (3.31) become

$$|\psi_i\rangle = \sum_{a,b} |b\rangle \left[e^{-\frac{1}{2}\beta H} (\xi + H)^{-\frac{1}{2}} \right]_{ba} C_{ai} = \sum_{a,b} |b\rangle (\sqrt{A})_{ba} C_{ai}, \quad (3.71)$$

where $A(H)$ is defined by

$$A(H) = \frac{e^{-\beta H}}{\xi + H}. \quad (3.72)$$

As in section 3.1, we can compute the entanglement spectrum by using the resolvent trick. The resolvent obeys almost the same Schwinger-Dyson equation as (3.53) in the PSSY model. The essential difference from the

PSSY model is to consider the back-reaction of branes instead of the probe brane approximation (3.37). Namely, Z_n is defined by the full matrix integral (3.70) which includes the determinant factor as

$$Z_n \equiv \langle \text{Tr} A^n \rangle = \int dH \det(\xi + H)^{-K} e^{-\text{Tr} V(H)} \text{Tr} A^n. \quad (3.73)$$

In the planar approximation, Z_n can be computed by using the deformed eigenvalue density $\rho_0(E)$ in (2.127) as

$$Z_n = \int_{E_0}^{\infty} dE \rho_0(E) A(E)^n, \quad (3.74)$$

where E_0 is the threshold energy determined by the genus-zero string equation (2.128). Thus, the Schwinger-Dyson equation (3.53) becomes

$$\lambda R(\lambda) = K + \int_{E_0}^{\infty} dE \rho_0(E) \frac{w(E)R(\lambda)}{K - w(E)R(\lambda)}, \quad (3.75)$$

where $w(E) \equiv A(E)/Z_1$ for (3.72) and (3.74). In a similar manner as in section 3.1, we can solve this Schwinger-Dyson equation by using iteration. The results are summarized as follows:

$$R(\lambda) = \int_{E_0}^{E_K} dE \rho_0(E) \frac{1}{\lambda - \lambda_0 - w(E)}, \quad (3.76)$$

$$D(\lambda) = \int_{E_0}^{E_K} dE \rho_0(E) \delta(\lambda - \lambda_0 - w(E)), \quad (3.77)$$

$$S = - \int_{E_0}^{E_K} dE \rho_0(E) (\lambda_0 + w(E)) \log(\lambda_0 + w(E)), \quad (3.78)$$

where λ_0 and E_K are defined instead of (3.59) and (3.60) by

$$\lambda_0 = \frac{1}{K} \int_{E_K}^{\infty} dE \rho_0(E) w(E), \quad (3.79)$$

$$K = \int_{E_0}^{E_K} dE \rho_0(E). \quad (3.80)$$

We can also take the probe brane approximation in this model. In that case we just set $E_0 = 0$ and use the original eigenvalue density $\rho_0^{\text{JT}}(E)$. We can numerically compute the Page curve by using the above results. One can find that the entanglement entropy monotonically decreases at late time in

the dynamical treatment of the branes while it approaches a constant value in the probe brane approximation. See also Figure 3 of [20] for the original results. Thus, we conclude that this is a useful model to investigate the back-reaction of the Hawking radiation. In section 4.3, we will apply this model to investigate the effect of the back-reaction to the refined Rényi negativity for a bipartite Hawking radiation system.

3.2.2 Analytic proof of monotonicity

As with the entanglement entropy, the Rényi entropies for general $n > 1$ also monotonically decrease at late time. We review the analytic proof of the monotonicity in the large ξ limit following [20]. To prove the monotonicity, we consider only the totally connected replica wormhole which dominates at late time. We define the “black hole Rényi entropy” by

$$S_{\text{BH}}^{(n)} = \frac{1}{1-n} \log \frac{Z_n}{Z_1^n}. \quad (3.81)$$

This is the Rényi entropy (3.4) with $\text{Tr}\rho_{\text{R}}^n$ given by the totally connected contribution (3.20). We also define the “thermodynamic entropy” by

$$S_{\text{thrm}}^{(n)} = n^2 \partial_n \left(-\frac{1}{n} \log \frac{Z_n}{Z_1^n} \right). \quad (3.82)$$

This is the refined Rényi entropy (3.5) with $\text{Tr}\rho_{\text{R}}^n$ given by (3.20). Note that these quantities are equivalent at $n = 1$ limit,

$$\lim_{n \rightarrow 1} S_{\text{BH}}^{(n)} = \lim_{n \rightarrow 1} S_{\text{thrm}}^{(n)}. \quad (3.83)$$

We want to prove the monotonicity with respect to the 't Hooft coupling

$$\partial_t S_{\text{BH}}^{(n)} < 0 \quad \text{for } n > 1, \quad 0 < t < t_c, \quad (3.84)$$

where t_c is the critical value discussed in the last part of subsection 2.3.2. From the definition (3.81) it is sufficient to prove

$$\frac{\partial_t Z_n}{n Z_n} > \frac{\partial_t Z_1}{Z_1} \quad \text{for } n > 1, \quad (3.85)$$

or equivalently,

$$\partial_n \frac{\partial_t Z_n}{n Z_n} > 0 \quad \text{for } n > 1. \quad (3.86)$$

Note that the derivative of the thermodynamic entropy (3.82) with respect to the 't Hooft coupling is given by

$$\partial_t S_{\text{thermo}} = -n^2 \partial_n \frac{\partial_t Z_n}{n Z_n}. \quad (3.87)$$

Thus, the thermodynamic entropy (3.82) also monotonically decreases if the condition (3.86) holds. We now prove (3.86) in the large ξ limit.

First let us evaluate $\partial_t Z_n$ in (3.86) as

$$\partial_t Z_n = \int_{E_0}^{\infty} dE \partial_t \rho_0(E) A(E)^n, \quad (3.88)$$

where E_0 and $\rho_0(E)$ depend on t , and we have used $\rho_0(E_0) = 0$. To evaluate $\partial_t \rho_0(E)$, it is convenient to use the Itzykson-Zuber variables $\mathcal{I}_n(u) \equiv I_n(u, \{t_k\})$ in (2.91). In terms of $\mathcal{I}_n(u)$, the leading eigenvalue density of the topological gravity (2.102) becomes

$$\rho_0(E) = \frac{1}{\sqrt{2\pi g_s}} \int_{E_0}^E dv \frac{1 - \mathcal{I}_1(-v)}{\sqrt{E - v}}. \quad (3.89)$$

Note that the derivative $\partial_t \mathcal{I}_n(u)$ is independent of what kind of topological gravity $\{t_k\}$ we consider, since t -dependence in (2.124) is not related to t_k . It is explicitly calculated as

$$\partial_t \mathcal{I}_n(u) = \frac{(2n - 1)!!}{(2\xi - 2u)^{n + \frac{1}{2}}}. \quad (3.90)$$

From the genus-zero string equation (2.94), we obtain

$$(\partial_t E_0)(\mathcal{I}_1(-E_0) - 1) - \frac{1}{\sqrt{2(\xi + E_0)}} = 0. \quad (3.91)$$

By using (3.90) and (3.91), we can calculate $\partial_t \rho_0(E)$ as

$$\begin{aligned} \partial_t \rho_0(E) &= (\partial_t E_0) \partial_{E_0} \rho_0(E) - \frac{1}{\sqrt{2\pi g_s}} \int_{E_0}^E dv \frac{\partial_t \mathcal{I}_1(-v)}{\sqrt{E - v}} \\ &= \frac{\partial_t E_0}{\sqrt{2\pi g_s}} \frac{\mathcal{I}_1(-E_0) - 1}{\sqrt{E - E_0}} - \frac{1}{\sqrt{2\pi g_s}} \int_{E_0}^E dv \frac{\partial_t \mathcal{I}_1(-v)}{\sqrt{E - v}} \\ &= \frac{1}{2\pi g_s (\xi + E)} \sqrt{\frac{\xi + E_0}{E - E_0}}. \end{aligned} \quad (3.92)$$

Now we know all the dependence of ξ in $\partial_t Z_n$. Plugging (3.92) into (3.88), $\partial_t Z_n$ can be evaluated in the large ξ limit as

$$\partial_t Z_n = \frac{e^{-n\beta E_0}}{2\sqrt{n\pi}\beta g_s} \xi^{-n-\frac{1}{2}} + O(\xi^{-n-\frac{3}{2}}). \quad (3.93)$$

Next we evaluate (3.86) in the large ξ limit. By using (2.127) in which the dependence of ξ is manifest, Z_n can be evaluated as

$$Z_n = \frac{\xi^{-n}}{\sqrt{2n\pi}\beta g_s} \int_{E_0}^{\infty} dv I_0(2\sqrt{v}) e^{-n\beta v} + O(\xi^{-n-1}). \quad (3.94)$$

Thus, we obtain

$$\frac{\partial_t Z_n}{nZ_n} = \frac{e^{-n\beta E_0}}{n\sqrt{2\xi} \int_{E_0}^{\infty} dv I_0(2\sqrt{v}) e^{-n\beta v}} + O(\xi^{-\frac{3}{2}}). \quad (3.95)$$

Note that $\partial_t Z_n/nZ_n$ is positive since $I_0(2\sqrt{v})$ in the denominator is always positive for $v > E_0 \geq E_0^c$. Here we define the minimal threshold energy E_0^c determined by (2.128) at the critical point $t = t_c$. We can see the positivity of $I_0(2\sqrt{v})$ in Figure 2.8 as the slope of the oscillating function for $v > E_0$, which comes from the derivative $I_0(2\sqrt{v}) = \partial_v[\sqrt{v}I_1(2\sqrt{v})]$. Since $\partial_t Z_n/nZ_n > 0$, to prove (3.86) is equivalent to prove

$$\partial_n \log \frac{\partial_t Z_n}{nZ_n} > 0 \quad \text{for } n > 1. \quad (3.96)$$

The left hand side is calculated as

$$\partial_n \log \frac{\partial_t Z_n}{nZ_n} = \frac{\int_{E_0}^{\infty} dv I_0(2\sqrt{v}) [n\beta(v - E_0) - 1] e^{-n\beta v}}{\int_{E_0}^{\infty} dv I_0(2\sqrt{v}) e^{-n\beta v}}. \quad (3.97)$$

The denominator is positive as discussed above. The numerator can be calculated by changing the variable $u = v - E_0$ and integrating by part,

$$(\text{numerator}) = \int_0^{\infty} du \frac{I_1(2\sqrt{u + E_0})}{\sqrt{u + E_0}} u e^{-n\beta u}. \quad (3.98)$$

Here the integrand is always positive for any E_0 satisfying $E_0^c < E_0 < 0$ as seen from the graph of $\sqrt{v}I_1(2\sqrt{v}) = (I_1(2\sqrt{v})/\sqrt{v}) \times v$ in Figure 2.8. Thus, we have proved (3.96). Hence, the monotonicity (3.84) has been proved in the large ξ limit. As discussed above, the monotonicity of the thermodynamic entropy (3.82) has also been proved.

Chapter 4

Negativity in JT gravity

In this chapter, we investigate the refined Rényi negativity and the capacity of negativity in JT gravity with dynamical FZZT anti-branes. The aim of this chapter is to discuss our results [21]. The entanglement negativity was previously studied in the PSSY model by Dong, McBride, and Weng [15], and it was found that the entanglement negativity can probe more elaborate entanglement structure than the entanglement entropy. However, the back-reaction of the Hawking radiation was not considered. We explore the back-reaction effects to the negativity by treating the branes as dynamical objects. We find that the refined Rényi negativity monotonically decreases at late time due to the back-reaction of branes. We also find that the capacity of negativity exhibits two peaks as a function of time, which comes from the exchange of dominance of different types of replica wormholes. Thus, we conclude that the capacity of negativity is a valuable indicator of the phase transitions of the entanglement structure.

This chapter is organized as follows. In section 4.1, we review the basics of the entanglement negativity and its Rényi generalizations. By using the analogy with the capacity of entanglement (3.6), we define a novel quantity, the “capacity of negativity.” The relation is summarized in Table 4.1. In section 4.2, we review the negativity spectrum which is analogous to the entanglement spectrum discussed in subsection 3.1.4. All quantities considered are computed by the negativity spectrum. In section 4.3, we investigate the refined Rényi negativity and find the late time monotonically decreasing behavior. In section 4.4, we explore the capacity of negativity and find that the capacity of negativity exhibits two peaks as a function of time.

4.1 Basics of entanglement negativity

In this section, we briefly review the entanglement negativity and its Rényi generalizations. The entanglement negativity is computed from the eigenvalues of a partially transposed density matrix. In particular, we focus on the refined Rényi negativity as an analogue of the refined Rényi entropy (3.5). We also define a novel quantity, which we call “capacity of negativity,” as an analogue of the capacity of entanglement (3.6). The relations among the statistical mechanical quantities, the refined Rényi entropies, and the refined Rényi negativities, are summarized in Table 4.1.

4.1.1 Partial transpose

The entanglement negativity [56] is a measure of entanglement in general mixed states, which is computed from a partially transposed density matrix [57, 58] of a bipartite quantum system with the Hilbert space $\mathcal{H} = \mathcal{H}_A \otimes \mathcal{H}_B$. For a given density matrix ρ_{AB} of the total system AB, the partially transposed density matrix $\rho_{AB}^{\text{T}_B}$ is defined by

$$\langle a, b | \rho_{AB}^{\text{T}_B} | a', b' \rangle = \langle a, b' | \rho_{AB} | a', b \rangle, \quad (4.1)$$

where T_B denotes the transposition only on the subsystem B. Recall that a quantum state is said to be separable if the density matrix factorizes as

$$\rho_{AB} = \sum_m p_m \rho_A^{(m)} \otimes \rho_B^{(m)}, \quad \sum_m p_m = 1, \quad p_m \geq 0. \quad (4.2)$$

In this case, all eigenvalues of $\rho_{AB}^{\text{T}_B} = \sum_m p_m \rho_A^{(m)} \otimes (\rho_B^{(m)})^{\text{T}}$ are non-negative since every $(\rho_B^{(m)})^{\text{T}}$ is non-negative by definition of the density matrix $\rho_B^{(m)}$.¹ However, $\rho_{AB}^{\text{T}_B}$ can have negative eigenvalues for entangled states. For example, it has eigenvalues $\{\frac{1}{2}, \frac{1}{2}, \frac{1}{2}, -\frac{1}{2}\}$ for Bell states. This fact suggests that one can define useful measures of entanglement from the eigenvalues of $\rho_{AB}^{\text{T}_B}$. For instance, the entanglement negativity is defined by the sum over the absolute values of the negative eigenvalues of the partially transposed density

¹As proven in [58], for 2×2 and 2×3 matrices, the non-negativity of $\rho_{AB}^{\text{T}_B}$ is both necessary and sufficient condition for the state to be separable. However it is not sufficient for more larger matrices.

matrix as

$$\mathcal{N} = \sum_i \frac{|\lambda_i| - \lambda_i}{2} = \sum_{\lambda_i < 0} |\lambda_i|, \quad (4.3)$$

where λ_i 's are the eigenvalues of $\rho_{AB}^{\text{T}_B}$. Similarly, the logarithmic negativity is defined by

$$\mathcal{E} = \log \left(\sum_i |\lambda_i| \right) = \log(2\mathcal{N} + 1). \quad (4.4)$$

In the last equation we have used the relation

$$\sum_i \lambda_i = \text{Tr} \rho_{AB}^{\text{T}_B} = \text{Tr} \rho_{AB} = 1. \quad (4.5)$$

Note that \mathcal{N} and \mathcal{E} vanish if all λ_i 's are non-negative. In particular, for a separable state $\mathcal{N} = \mathcal{E} = 0$. This implies that when \mathcal{N} and \mathcal{E} are non-zero the system is not in a separable state. Thus, we can definitely say that the system A and the system B are entangled when \mathcal{N} and \mathcal{E} are non-zero.

4.1.2 Rényi generalization

Let us consider the Rényi generalizations of the entanglement negativity. The refined Rényi negativity and the capacity of negativity are defined as analogues of the refined Rényi entropy (3.5) and the capacity of entanglement (3.6), respectively. First the n -th Rényi negativity is defined by

$$Z^{\text{T}_B(n)} = \text{Tr} \left[(\rho_{AB}^{\text{T}_B})^n \right] = \sum_i (\lambda_i)^n. \quad (4.6)$$

Since the entanglement negativity \mathcal{N} in (4.3) and the logarithmic negativity \mathcal{E} in (4.4) are defined by the absolute values of the eigenvalues, we take different analytic continuations for even and odd replica number n

$$Z^{\text{T}_B(2m, \text{even})} = \sum_i |\lambda_i|^{2m}, \quad (4.7)$$

$$Z^{\text{T}_B(2m-1, \text{odd})} = \sum_i \text{sgn}(\lambda_i) |\lambda_i|^{2m-1}. \quad (4.8)$$

Then the logarithmic negativity (4.4) is obtained by the following limit

$$\mathcal{E} = \lim_{m \rightarrow \frac{1}{2}} \log Z^{\text{T}_B(2m, \text{even})}. \quad (4.9)$$

Stat. Mechanics	Rényi Entropy	Rényi Negativity
β	n	n
H	$H_A = -\log \rho_A$	$H^{\text{T}_B} = -\log \rho_{AB}^{\text{T}_B}$
$Z(\beta) = \text{Tr} [e^{-\beta H}]$	$Z_A^{(n)} = \text{Tr}_A [e^{-n H_A}]$	$Z^{\text{T}_B(n)} = \text{Tr} [e^{-n H^{\text{T}_B}}]$
$F(\beta) = -\beta^{-1} \log Z(\beta)$	$F_A^{(n)} = -n^{-1} \log Z(n)$	$F^{\text{T}_B(n)} = -n^{-1} \log Z^{\text{T}_B(n)}$
$E(\beta) = -\partial_\beta \log Z(\beta)$	$E_A^{(n)} = -\partial_n \log Z(n)$	$E^{\text{T}_B(n)} = -\partial_n \log Z^{\text{T}_B(n)}$
$S(\beta) = \beta^2 \partial_\beta F(\beta)$	$\tilde{S}_A^{(n)} = n^2 \partial_n F_A^{(n)}$	$S^{\text{T}_B(n)} = n^2 \partial_n F^{\text{T}_B(n)}$
$C(\beta) = -\beta \partial_\beta S(\beta)$	$\tilde{C}_A^{(n)} = -n \partial_n \tilde{S}_A^{(n)}$	$C^{\text{T}_B(n)} = -n \partial_n S^{\text{T}_B(n)}$

Table 4.1: The correspondence among the statistical mechanical quantities, the Rényi entropic quantities, and the Rényi negativities. Here β is the inverse temperature, and n is the replica number, ρ_A is the reduced density matrix and H_A is the modular Hamiltonian. In the third column, H^{T_B} denotes the partially transposed version of the modular Hamiltonian and we ignored the difference between even n and odd n for simplicity.

In this paper, we focus on the refined Rényi negativities² [15]

$$S^{\text{T}_B(n,\text{even})} = -n^2 \partial_n \left(\frac{1}{n} \log Z^{\text{T}_B(n,\text{even})} \right), \quad (4.10)$$

$$S^{\text{T}_B(n,\text{odd})} = -n^2 \partial_n \left(\frac{1}{n} \log Z^{\text{T}_B(n,\text{odd})} \right), \quad (4.11)$$

which are defined in analogy with the refined Rényi entropy (3.5). In section 4.3, we consider the refined Rényi negativities in JT gravity and study the effect of the back-reaction of branes to these quantities.

Note that there is a natural correspondence among the statistical mechanical quantities, the Rényi entropic quantities, and the Rényi negativities under the appropriate identifications [52, 53, 61] (see Table 4.1). By using the correspondence in Table 4.1, we define novel quantities which we call the

²Note that $S^{\text{T}_B} = \lim_{m \rightarrow 1} S^{\text{T}_B(2m-1,\text{odd})}$ is called the “odd entanglement entropy” or the “partially transposed entropy” [59, 60] since its definition is the same as the von Neumann entropy with ρ_{AB} replaced by $\rho_{AB}^{\text{T}_B}$.

“capacity of negativities” as analogues of the capacity of entanglement

$$C^{\text{TB}(n,\text{even})} = -n\partial_n S^{\text{TB}(n,\text{even})}, \quad (4.12)$$

$$C^{\text{TB}(n,\text{odd})} = -n\partial_n S^{\text{TB}(n,\text{odd})}, \quad (4.13)$$

As shown in [62, 63], the capacity of entanglement exhibits a peak around the Page time, which comes from the exchange of dominance between the disconnected saddle and the totally connected replica wormhole. Around the Page time, several types of replica wormholes including partially connected ones can also contribute. The capacity of entanglement is sensitive to these contributions, which is the physical origin of the peak. On the other hand, there is another dominant saddle which breaks the replica symmetry in the case of the entanglement negativity [15], as we review later. Thus, we expect that the capacity of negativity exhibits several peaks around each phase transition. In section 4.4 we will see that this is indeed the case.

Before closing this section, we present the explicit forms of the refined Rényi negativity and the capacity of negativity for later use:

$$S^{\text{TB}(n)} = -\sum_i \frac{(\lambda_i)^n}{Z^{\text{TB}(n)}} \log \frac{|\lambda_i|^n}{Z^{\text{TB}(n)}}, \quad (4.14)$$

$$C^{\text{TB}(n)} = \sum_i \frac{(\lambda_i)^n}{Z^{\text{TB}(n)}} \left(\log \frac{|\lambda_i|^n}{Z^{\text{TB}(n)}} \right)^2 - (S^{\text{TB}(n)})^2. \quad (4.15)$$

Note that these formulas are valid for both even and odd n . By using the eigenvalue density $D(\lambda)$ of $\rho_{\text{AB}}^{\text{TB}}$ (also known as the negativity spectrum), the sum in the above equations can be replaced by the integral $\int d\lambda D(\lambda)$. In section 4.3 and 4.4, we will study the refined Rényi negativity in the canonical ensemble and the capacity of negativity in the microcanonical ensemble using the negativity spectrum, respectively.

4.2 Negativity spectrum in JT gravity

In this section, we investigate the entanglement negativity in a toy model of an evaporating black hole. In particular, we consider the entanglement negativity between a bipartite Hawking radiation system. The Hilbert space is given by $\mathcal{H} = \mathcal{H}_{\text{BH}} \otimes \mathcal{H}_{\text{R}}$ where the radiation subspace is further divided

into two pieces $\mathcal{H}_R = \mathcal{H}_1 \otimes \mathcal{H}_2$. The entanglement negativity between \mathcal{H}_1 and \mathcal{H}_2 is computed from the partially transposed reduced density matrix $\rho_R^{\text{T}_2}$ on the radiation system:

$$\rho = |\Psi\rangle\langle\Psi| \xrightarrow{\text{partial trace}} \rho_R = \text{Tr}_{\text{BH}}\rho \xrightarrow{\text{partial transpose}} \rho_R^{\text{T}_2}, \quad (4.16)$$

where the state of the total system $|\Psi\rangle \in \mathcal{H}$ is defined by

$$|\Psi\rangle = \mathcal{N} \sum_{i_1=1}^{K_1} \sum_{i_2=1}^{K_2} |\psi_{i_1 i_2}\rangle_{\text{BH}} \otimes |i_1, i_2\rangle_{\text{R}}. \quad (4.17)$$

We denote the dimensions of the radiation subsystems by $K_1 = \dim \mathcal{H}_1$ and $K_2 = \dim \mathcal{H}_2$, respectively. The dimension of the total radiation system is given by $K = K_1 K_2$. The normalization factor \mathcal{N} is determined so that the norm $\langle\Psi|\Psi\rangle = 1$. The aim of this section is to obtain the negativity spectrum in JT gravity with dynamical FZZT anti-branes. Most computations are parallel to those of the previous study in the PSSY model [15]. The essential difference is that we use the deformed eigenvalue density (2.127) to calculate the path integral of JT gravity.

4.2.1 Dominant saddles

Before calculating the negativity spectrum, we review the dominant saddles which contribute to the entanglement negativity following [15]. The entanglement negativity has more elaborate phase structure than that of the entanglement entropy. See also appendix A of [15] for more details. First the reduced density matrix ρ_R is calculated from the state (4.17) as

$$\rho_R = \sum_{i_1, j_1=1}^{K_1} \sum_{i_2, j_2=1}^{K_2} |j_1, j_2\rangle\langle i_1, i_2|_{\text{R}} \langle\psi_{i_1 i_2}|\psi_{j_1 j_2}\rangle_{\text{BH}}, \quad (4.18)$$

where we have included the normalization factor \mathcal{N} in the definition of $|\psi_{i_1 i_2}\rangle_{\text{BH}}$ for notational simplicity. From the reduced density matrix, we take the partial transpose on the second subsystem \mathcal{H}_2 as

$$\rho_R^{\text{T}_2} = \sum_{i_1, j_1=1}^{K_1} \sum_{i_2, j_2=1}^{K_2} |j_1, i_2\rangle\langle i_1, j_2|_{\text{R}} \langle\psi_{i_1 i_2}|\psi_{j_1 j_2}\rangle_{\text{BH}}. \quad (4.19)$$

The amplitude $\langle \psi_{i_1 i_2} | \psi_{j_1 j_2} \rangle_{\text{BH}}$ will be calculated by the gravitational path integral. As with the case of the entanglement entropy, the n -th moment $\text{Tr}(\rho_{\text{R}}^{\text{T}_2})^n$ is given by the sum over all possible configurations which satisfy the appropriate boundary conditions. Following [15], the n -th moment $\text{Tr}(\rho_{\text{R}}^{\text{T}_2})^n$ is expressed as the sum over the permutation group S_n

$$\text{Tr}(\rho_{\text{R}}^{\text{T}_2})^n = \frac{1}{(K Z_1)^n} \sum_{g \in S_n} \left(\prod_{i=1}^{\chi(g)} Z_{|c_i(g)|} \right) K_1^{\chi(g^{-1}X)} K_2^{\chi(g^{-1}X^{-1})}, \quad (4.20)$$

where $\chi(g)$ is the number of disjoint cycles of the permutation g , $|c_i(g)|$ is the length of the i -th disjoint cycle of g , $X(X^{-1})$ is the (anti-)cyclic permutation of length n , and Z_n is the disk partition function of JT gravity surrounded by n asymptotic boundaries and n branes as in chapter 3.

To find the dominant saddles, we approximate $Z_n \sim e^{S_0}$ and take the planar approximation in the large parameter regime $e^{S_0}, K \gg 1$. There are four types of dominant saddles each of which corresponds to a certain element of the permutation group:

$$\begin{aligned} g = \mathbb{1} & \quad \text{for } e^{S_0} \gg K_1 K_2, \\ g = X & \quad \text{for } K_1 \gg K_2 e^{S_0}, \\ g = X^{-1} & \quad \text{for } K_2 \gg K_1 e^{S_0}, \\ g = \tau & \quad \text{for } K_1 K_2 \gg e^{S_0}, e^{-S_0} \ll K_1/K_2 \ll e^{S_0}, \end{aligned} \quad (4.21)$$

where τ denotes the non-crossing pairings. A non-crossing pairing consists of a certain set of transpositions. The ‘‘crossing’’ or ‘‘non-crossing’’ for an element of S_n is defined by drawing a corresponding diagram. For example, let us consider the $n = 6$ case. An element $(13)(24)(56) \in S_6$ is a crossing pairing represented by the following diagram

$$\begin{array}{cccccc} 1 & 2 & 3 & 4 & 5 & 6, \\ \hline & \diagdown & \diagup & & \diagdown & \diagup \end{array}, \quad (4.22)$$

where each pair of numbers transposed is connected by each line. This is a crossing pairing since the diagram includes a crossing of lines. On the other hand, an element $(12)(36)(45) \in S_6$ is a non-crossing pairing represented by the following diagram

$$\begin{array}{cccccc} 1 & 2 & 3 & 4 & 5 & 6. \\ \hline & \diagdown & & \diagup & & \diagdown \end{array}. \quad (4.23)$$

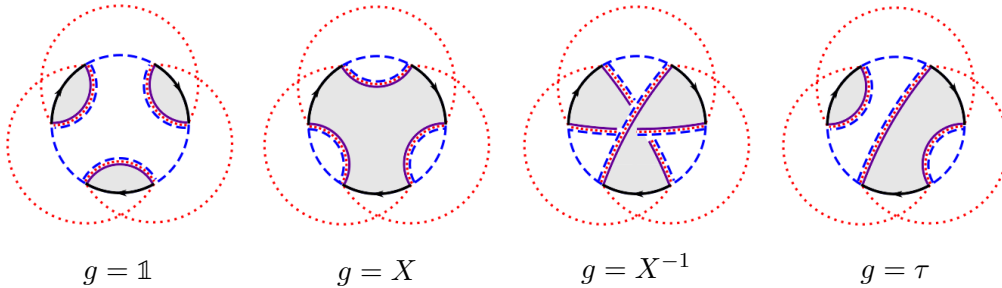


Figure 4.1: The four dominant saddles [15]. These are the examples of $n = 3$. The sums over the first and second flavor indices correspond to the blue dashed and red dotted loops, respectively. The gravitational path integral Z_n is represented by the gray shaded disks.

This is a non-crossing pairing since the diagram does not include any crossing of lines. Note that the “crossing” or “non-crossing” is also defined for odd n , but a pairing for odd n includes a remnant. In general, it is known that the number of non-crossing pairings in S_n is given by

$$\begin{cases} C_m & \text{for } n = 2m, \\ (2m - 1)C_{m-1} & \text{for } n = 2m - 1, \end{cases} \quad (4.24)$$

where C_m is the Catalan number

$$C_m = \frac{1}{m+1} \binom{2m}{m}. \quad (4.25)$$

As with the Rényi entropy discussed in chapter 3, the n -th moment $\text{Tr}(\rho_{\text{R}}^{\text{T}_2})^n$ can be represented by drawing diagrams as in Figure 4.1. Each element of the permutation group in (4.20) corresponds to the way to connect the asymptotic boundaries with the branes, while K_1 and K_2 correspond to the index loops. The four dominant saddles $g = \mathbb{1}, X, X^{-1}, \tau$ are referred to as disconnected, cyclically connected, anti-cyclically connected, pairwise connected saddles, respectively. As seen from Figure 4.1, the pairwise connected saddles are not invariant under the exchange of the replicas while the other dominant saddles are invariant. Thus, the pairwise connected saddles spontaneously break the replica symmetry. This is an interesting property not seen in the case of the entanglement entropy.

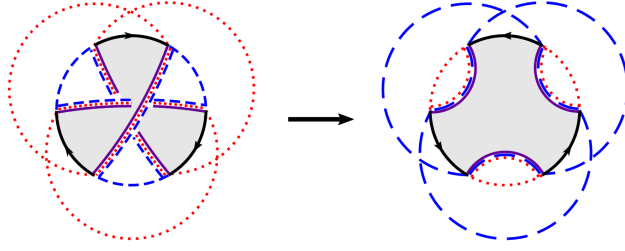


Figure 4.2: Anti-cyclically connected saddle X^{-1} becomes a planar diagram by reversing the orientation of the asymptotic boundaries [15].

The contributions of the four saddles for (4.20) before divided by $(KZ_1)^n$ are schematically evaluated as

$$\begin{aligned}
 g = \mathbb{1} &\quad \rightarrow \quad (e^{S_0})^n K, \\
 g = X &\quad \rightarrow \quad e^{S_0} K_1^n K_2^{f(n)}, \\
 g = X^{-1} &\quad \rightarrow \quad e^{S_0} K_1^{f(n)} K_2^n, \\
 g = \tau &\quad \rightarrow \quad (e^{S_0})^{\lceil \frac{n}{2} \rceil} K^{\lfloor \frac{n}{2} \rfloor + 1},
 \end{aligned} \tag{4.26}$$

where $\lceil \frac{n}{2} \rceil$ and $\lfloor \frac{n}{2} \rfloor$ are ceiling and floor function, and $f(n)$ is defined by

$$f(n) \equiv \chi(X^{-2}) = \begin{cases} 1, & n \text{ odd}, \\ 2, & n \text{ even}. \end{cases} \tag{4.27}$$

As seen from Figure 4.1, the anti-cyclically connected saddle $g = X^{-1}$ looks like a non-planar diagram but it becomes a planar diagram by reversing the orientation of the asymptotic boundaries (see Figure 4.2). Thus, it does dominate in a certain parameter regime.

We show a schematic phase diagram among the four dominant saddles in Figure 4.3. In our study, we particularly focus on a parameter regime $K_2 < e^{S_0}$ where K_2 and S_0 are fixed. This regime corresponds to a horizontal line with $\log K_2 < S_0$ in Figure 4.3. Thus, we expect two phase transitions as varying K_1 along the horizontal line. First, a phase transition occurs between the disconnected and pairwise connected saddles, and next a transition occurs between the pairwise connected to cyclically connected saddles. Note that several types of planar diagrams other than the dominant ones can contribute around the phase transitions. As summarized in (4.20), these contributions can also be described by certain elements of S_n .

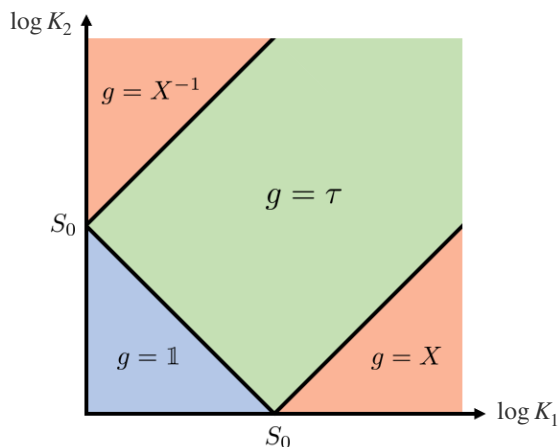


Figure 4.3: The phase diagram of the entanglement structure probed by the entanglement negativity [15].

In particular, elements on the “geodesic” between $\mathbb{1}$ and X contribute in the parameter regime which we consider here. It is known that there is a one-to-one correspondence between such elements and the all planar diagrams. See also appendix A of [15] and [64] for more details.

4.2.2 Ensemble average

We study the negativity spectrum in the matrix model of JT gravity with dynamical FZZT anti-branes. The sum over the replica wormholes comes from the ensemble average in the matrix integral. The matrix integral is again given by (3.68)

$$\begin{aligned}
 Z &= \int dH e^{-\text{Tr}V(H)} \det(\xi + H)^{-K} \\
 &= \int dH dQ dQ^\dagger e^{-\text{Tr}V(H) - \text{Tr}Q^\dagger(\xi + H)Q}.
 \end{aligned}
 \tag{4.28}$$

To study the entanglement negativity we divide K into two parts: $K = K_1 K_2$. In other words, we consider a bipartite system of the Hilbert space $\mathcal{H}_R = \mathcal{H}_1 \otimes \mathcal{H}_2$ with

$$\dim \mathcal{H}_1 = K_1, \quad \dim \mathcal{H}_2 = K_2.
 \tag{4.29}$$

We denote the components of H, Q by $H_{ab}, Q_{ai_1 i_2}$, where $a, b = 1, \dots, N$ are color indices and $i_1, j_1 = 1, \dots, K_1, i_2, j_2 = 1, \dots, K_2$ are flavor indices. The

subscript of the flavor indices 1 and 2 correspond to \mathcal{H}_1 and \mathcal{H}_2 , respectively. As in chapter 3, the black hole microstates are given by the canonical thermal pure states

$$|\psi_{i_1 i_2}\rangle = \sum_a e^{-\frac{1}{2}\beta H} |a\rangle Q_{ai_1 i_2} = \sum_{a,b} |b\rangle \left(e^{-\frac{1}{2}\beta H} \right)_{ba} Q_{ai_1 i_2}. \quad (4.30)$$

By changing the variable $Q = (\xi + H)^{-\frac{1}{2}} C$, the matrix integral becomes

$$Z = \int dH dC dC^\dagger \det(\xi + H)^{-K} e^{-\text{Tr}V(H) - \text{Tr}C^\dagger C}. \quad (4.31)$$

Again we can calculate the average over C by using the Wick contraction. The black hole microstates (4.30) becomes

$$|\psi_{i_1 i_2}\rangle = \sum_{a,b} |b\rangle \left(\sqrt{A} \right)_{ba} C_{ai_1 i_2}, \quad (4.32)$$

where $A(H)$ is defined by (3.72). The reduced density matrix is defined by the overlap $\langle \psi_{i_1 i_2} | \psi_{j_1 j_2} \rangle$ which is given by

$$W_{i_1 i_2, j_1 j_2} \equiv \langle \psi_{i_1 i_2} | \psi_{j_1 j_2} \rangle = \sum_{a,b} A_{ab} C_{ai_1 i_2}^* C_{bj_1 j_2}. \quad (4.33)$$

To consider the partially transposed density matrix, we take the partial transpose T_2 of W on the second flavor factor \mathcal{H}_2

$$(W^{T_2})_{i_1 i_2, j_1 j_2} = W_{i_1 j_2, j_1 i_2} = \sum_{a,b} A_{ab} C_{ai_1 j_2}^* C_{bj_1 i_2}. \quad (4.34)$$

By using the Wick contraction, the average over the flavor degrees of freedom can be computed as

$$\overline{W_{i_1 i_2, j_1 j_2}} = \delta_{i_1 j_1} \delta_{i_2 j_2} \text{Tr} A, \quad (4.35)$$

$$\overline{(W^{T_2})_{i_1 i_2, j_1 j_2}} = \delta_{i_1 j_1} \delta_{i_2 j_2} \text{Tr} A. \quad (4.36)$$

Note that the flavor average of W^{T_2} is equal to that of W . As discussed in [15], one can visualize the above computation by the following diagrams:

$$W_{i_1 i_2, j_1 j_2} = (C^\dagger A C)_{i_1 i_2, j_1 j_2} = \begin{array}{c} \begin{array}{ccc} (C^\dagger)_{i_1 i_2 a} & A_{ab} & C_{bj_1 j_2} \\ i_1 \text{---} & \longleftarrow & \text{---} j_1 \\ i_2 \text{---} & & \text{---} j_2 \end{array} \\ \text{---} \end{array}, \quad (4.37)$$

$$(W^{\text{T}_2})_{i_1 i_2, j_1 j_2} = (C^\dagger A C)_{i_1 j_2, j_1 i_2} = \begin{array}{c} (C^\dagger)_{i_1 j_2 a} \quad A_{ab} \quad C_{b j_1 i_2} \\ \begin{array}{ccc} i_1 & \xrightarrow{\text{blue dashed}} & j_1 \\ i_2 & \xrightarrow{\text{red dotted}} & j_2 \end{array} \\ \text{black thick curve} \end{array} . \quad (4.38)$$

Here the black thick curve corresponds to the asymptotic boundary. The blue dashed curves and the red dotted curves carry the first and the second flavor indices, respectively. The reduced density matrix of the radiation system is again given by (3.30) as

$$\rho_{i_1 i_2, j_1 j_2} = \frac{W_{j_1 j_2, i_1 i_2}}{\text{Tr} W} . \quad (4.39)$$

Thus, the partially transposed density matrix is written as

$$(\rho^{\text{T}_2})_{i_1 i_2, j_1 j_2} = \frac{(W^{\text{T}_2})_{j_1 j_2, i_1 i_2}}{\text{Tr} W} . \quad (4.40)$$

To compute the negativities, we consider the n -th moment $\text{Tr} (\rho^{\text{T}_2})^n$. In the planar approximation, we can take the average of the numerator and the denominator independently

$$\overline{\text{Tr} (\rho^{\text{T}_2})^n} \approx \frac{\overline{\text{Tr} (W^{\text{T}_2})^n}}{(\overline{\text{Tr} W})^n} . \quad (4.41)$$

The numerator can be computed by using the Wick contraction, and it boils down to the sum over the all possible combinations of C^\dagger and C . Finally $\overline{\text{Tr} (\rho^{\text{T}_2})^n}$ is expressed as a sum over the permutation group in (4.20)

$$\overline{\text{Tr} (\rho^{\text{T}_2})^n} \approx \frac{1}{(K \overline{\text{Tr} A})^n} \sum_{g \in S_n} \left(\prod_{i=1}^{\chi(g)} \text{Tr} A^{|c_i(g)|} \right) K_1^{\chi(g^{-1}X)} K_2^{\chi(g^{-1}X^{-1})} . \quad (4.42)$$

We also take the average over the color degrees of freedom. Again, in the planar approximation, we can take the average of the numerator and denominator independently

$$\langle \overline{\text{Tr} (\rho^{\text{T}_2})^n} \rangle \approx \frac{1}{(K \langle \text{Tr} A \rangle)^n} \sum_{g \in S_n} \left(\prod_{i=1}^{\chi(g)} \langle \text{Tr} A^{|c_i(g)|} \rangle \right) K_1^{\chi(g^{-1}X)} K_2^{\chi(g^{-1}X^{-1})} , \quad (4.43)$$

where $\langle \text{Tr} A^n \rangle$ is defined by

$$\langle \text{Tr} A^n \rangle = \int dH \det(\xi + H)^{-K} e^{-\text{Tr} V(H)} \text{Tr} A(H)^n . \quad (4.44)$$

g	$\mathbb{1}$	τ	X	X^{-1}
$Z^{\text{T}_2(2m,\text{even})}$	$\frac{1}{K^{2m-1}}$	$\frac{C_m Z_2^m}{K^{m-1} Z_1^{2m}}$	$\frac{Z_{2m}}{K_2^{2m-2} Z_1^{2m}}$	$\frac{Z_{2m}}{K_1^{2m-2} Z_1^{2m}}$
$Z^{\text{T}_2(2m-1,\text{odd})}$	$\frac{1}{K^{2m-2}}$	$\frac{(2m-1)C_{m-1} Z_2^{m-1}}{K^{m-1} Z_1^{2m-2}}$	$\frac{Z_{2m-1}}{K_2^{2m-2} Z_1^{2m-1}}$	$\frac{Z_{2m-1}}{K_1^{2m-2} Z_1^{2m-1}}$

Table 4.2: The values of Rényi negativities in each dominant saddle [15]. Here C_m is the Catalan number (4.25) which comes from the number of non-crossing pairings.

In the planar approximation, it is given by Z_n in (3.74). If we further take the probe brane approximation, it is given by (3.52). The values of the Rényi negativities in each dominant saddle are summarized in Table 4.2. Around the phase transitions, several types of replica wormholes other than the dominant ones can contribute to the negativities. Thus, we need to sum over all possible geometries to study negativities beyond the dominant phases. However, the sum over the permutation group (4.43) is not useful to handle. In the next subsection, we invoke the resolvent method which is useful to sum over the possible geometries in the palanar approximation.

4.2.3 Resolvent trick

To compute the sum (4.43) efficiently in the planar approximation, we use the resolvent trick discussed in [15]. Let us define the resolvent matrix for the partially transposed density matrix by

$$\begin{aligned}
R_{i_2 j_2}^{i_1 j_1}(\lambda) &= \left(\frac{1}{\lambda \mathbf{1} - \rho^{\text{T}_2}} \right)_{i_2 j_2}^{i_1 j_1} \\
&= \frac{1}{\lambda} \delta^{i_1 j_1} \delta_{i_2 j_2} + \sum_{n=1}^{\infty} \frac{1}{\lambda^{n+1}} ((\rho^{\text{T}_2})^n)_{i_2 j_2}^{i_1 j_1}.
\end{aligned} \tag{4.45}$$

We denote the flavor indices associated to \mathcal{H}_1 as the upper indices and those associated to \mathcal{H}_2 as the lower indices for later diagrammatic representations. We also define the resolvent by

$$R(\lambda) = \text{Tr} R_{i_2 j_2}^{i_1 j_1}(\lambda) = \frac{K}{\lambda} + \sum_{n=1}^{\infty} \frac{1}{\lambda^{n+1}} \text{Tr} (\rho^{\text{T}_2})^n, \tag{4.46}$$

where we have traced over the both radiation systems \mathcal{H}_1 and \mathcal{H}_2 . As with the entanglement spectrum, we can obtain the negativity spectrum $D(\lambda)$ by taking the discontinuity of $R(\lambda)$ across the real axis (3.57). From the negativity spectrum $D(\lambda)$, the Rényi negativities in (4.6) are computed by

$$Z^{\text{T}_2(n)} = \text{Tr}(\rho^{\text{T}_2})^n = \int_{-\infty}^{\infty} d\lambda D(\lambda) \lambda^n. \quad (4.47)$$

Similarly, the refined Rényi negativity $S^{\text{T}_2(n)}$ in (4.14) and the capacity of negativity $C^{\text{T}_2(n)}$ in (4.15) are computed by

$$S^{\text{T}_2(n)} = - \int_{-\infty}^{\infty} d\lambda D(\lambda) \frac{\lambda^n}{Z^{\text{T}_2(n)}} \log \frac{|\lambda|^n}{Z^{\text{T}_2(n)}}, \quad (4.48)$$

$$C^{\text{T}_2(n)} = \int_{-\infty}^{\infty} d\lambda D(\lambda) \frac{\lambda^n}{Z^{\text{T}_2(n)}} \left(\log \frac{|\lambda|^n}{Z^{\text{T}_2(n)}} \right)^2 - (S^{\text{T}_2(n)})^2. \quad (4.49)$$

Thus, the problem boils down to obtain the negativity spectrum $D(\lambda)$ from the resolvent $R(\lambda)$. To this end, we will write down the Schwinger-Dyson equation for $R(\lambda)$ and solve it approximately. Using the diagrammatic representation (4.38), $R_{i_2 j_2}^{i_1 j_1}(\lambda)$ in (4.45) is represented by [15]

$$\textcircled{\text{R}} = \text{---} + \text{---} + \text{---} + \dots, \quad (4.50)$$

where each pair of dashed blue line and dotted red line is weighted by $1/\lambda$ and carries the flavor indices. Averaging over the flavor degrees of freedom leads to the following Schwinger-Dyson equation [15]:

$$\begin{aligned} \textcircled{\text{R}} &= \text{---} + \text{---} + \text{---} + \dots \\ &+ \text{---} + \text{---} + \text{---} + \dots \end{aligned} \quad (4.51)$$

Here the blue thick curve represents the FZZT anti-branes (EOW branes in the case of the PSSY model). Each dashed blue loop associated to the flavor index of \mathcal{H}_1 gives $K_1 = \text{Tr} \delta_{i_1 j_1}$ contribution, and each dotted red loop associated to the flavor index of \mathcal{H}_2 gives $K_2 = \text{Tr} \delta_{i_2 j_2}$ contribution. The

gray disk surrounded by n asymptotic boundaries and n branes gives Z_n contribution. For instance, we write down the first few terms of (4.51) in terms of the powers of R as

$$\begin{aligned}
R_{i_2 j_2}^{i_1 j_1} &= \frac{1}{\lambda} \delta^{i_1 j_1} \delta_{i_2 j_2} + \frac{1}{\lambda} \frac{Z_1}{K Z_1} R_{i_2 j_2}^{i_1 j_1} + \frac{1}{\lambda} \frac{Z_2}{(K Z_1)^2} \sum_{k=1}^{K_2} \tilde{R}_{kk} R_{i_2 j_2}^{i_1 j_1} \\
&+ \frac{1}{\lambda} \frac{Z_3}{(K Z_1)^3} \sum_{k_1, k_2=1}^{K_2} \tilde{R}_{k_2 k_1} \tilde{R}_{i_2 k_2} R_{k_1 j_2}^{i_1 j_1} + \dots,
\end{aligned} \tag{4.52}$$

where the matrix \tilde{R}_{kl} is defined by the partial trace over the flavor degrees of freedom associated to \mathcal{H}_1 as

$$\tilde{R}_{kl} \equiv \sum_{i=1}^{K_1} R_{kl}^{ii}. \tag{4.53}$$

In general, the Schwinger-Dyson equation (4.52) is expressed as

$$R_{i_2 j_2}^{i_1 j_1} = \frac{1}{\lambda} \delta^{i_1 j_1} \delta_{i_2 j_2} + \frac{1}{\lambda} \sum_{n=1}^{\infty} \frac{Z_n}{(K Z_1)^n} \tilde{R}_{k_{n-1} k_1} \tilde{R}_{i_2 k_2} \tilde{R}_{k_1 k_3} \cdots \tilde{R}_{k_{n-3} k_{n-1}} R_{k_{n-2} j_2}^{i_1 j_1}, \tag{4.54}$$

where we omit the sum associated to the products of \tilde{R}_{kl} 's for notational simplicity. As seen from (4.51) or (4.54), the flavor indices associated to \mathcal{H}_1 are simply self-contracted while the indices associated to \mathcal{H}_2 are contracted between the skipped pairs except for the both ends of \tilde{R} . As discussed in [15], the complicated contractions of the second flavor indices are simplified by using the iteration starting from $R_{i_2 j_2}^{i_1 j_1} \propto \delta^{i_1 j_1} \delta_{i_2 j_2} / \lambda$. Plugging this into (4.54), one can find that $R_{i_2 j_2}^{i_1 j_1}$ is proportional to $\delta^{i_1 j_1} \delta_{i_2 j_2}$ to all orders in $1/\lambda$. Thus, $R_{i_2 j_2}^{i_1 j_1}$ can be expressed as

$$R_{i_2 j_2}^{i_1 j_1} = \frac{R(\lambda)}{K} \delta^{i_1 j_1} \delta_{i_2 j_2}, \tag{4.55}$$

where $R(\lambda)$ denotes the trace of the resolvent matrix over the both flavor indices. By using this expression, the products of the resolvent matrices in (4.54) becomes

$$\tilde{R}_{k_{n-1} k_1} \tilde{R}_{i_2 k_2} \tilde{R}_{k_1 k_3} \cdots \tilde{R}_{k_{n-3} k_{n-1}} R_{k_{n-2} j_2}^{i_1 j_1} = \begin{cases} \left(\frac{R}{K_2}\right)^{n-1} R_{i_2 j_2}^{i_1 j_1}, & n \text{ odd,} \\ K_2 \left(\frac{R}{K_2}\right)^{n-1} R_{i_2 j_2}^{i_1 j_1}, & n \text{ even.} \end{cases} \tag{4.56}$$

The factor K_2 for even n comes from an extra flavor loop associated to \mathcal{H}_2 . By using this and taking the trace over the both flavor indices, the Schwinger-Dyson equation (4.54) becomes

$$\lambda R = K + K_2 \sum_{m=1}^{\infty} \frac{Z_{2m-1}}{(KK_2Z_1)^{2m-1}} R^{2m-1} + K_2^2 \sum_{m=1}^{\infty} \frac{Z_{2m}}{(KK_2Z_1)^{2m}} R^{2m}. \quad (4.57)$$

Plugging Z_n in (3.74) into this equation leads to geometric series, and the resulting Schwinger-Dyson equation is given by

$$\lambda R(\lambda) = K + K_2^2 \int_{E_0}^{\infty} dE \rho_0(E) \frac{w(E)R(\lambda)(K + w(E)R(\lambda))}{K^2K_2^2 - w(E)^2R(\lambda)^2}, \quad (4.58)$$

where E_0 and $w(E)$ are defined by (2.128) and (3.54), respectively. Note that this equation reduces to (3.75) at $K_2 = 1$, which corresponds to the horizontal axis of the phase diagram in Figure 4.3. This equation is valid for the parameter regime $K_2 \ll K_1 e^{S_0}$ in which three types of saddles $g = \mathbb{1}, \tau, X$ can dominate. See also [15] for other parameter regime $K_1 \ll K_2 e^{S_0}$ in which other three types of saddles $g = \mathbb{1}, \tau, X^{-1}$ can dominate. The Schwinger-Dyson equations for the two parameter regimes are equivalent by exchanging K_1 and K_2 . In this thesis, we only focus on the former parameter regime $K_2 \ll K_1 e^{S_0}$. In the next subsection, we obtain the negativity spectrum by solving (4.58) approximately.

4.2.4 Negativity spectrum

In a similar manner as in section 3.1, we compute the negativity spectrum $D(\lambda)$ by solving the Schwinger-Dyson equation (4.58). Let us approximate the integral in (4.58) as

$$\lambda R(\lambda) \approx K + K_2^2 \int_{E_0}^{E_K} dE \rho_0(E) \frac{w(E)R(\lambda)(K + w(E)R(\lambda))}{K^2K_2^2 - w(E)^2R(\lambda)^2} + \lambda_0 R(\lambda), \quad (4.59)$$

where E_K and λ_0 are defined by

$$K = K_2^2 \int_{E_0}^{E_K} dE \rho_0(E), \quad (4.60)$$

$$\lambda_0 = \frac{1}{K} \int_{E_K}^{\infty} dE \rho_0(E) w(E). \quad (4.61)$$

In the approximation, we have assumed $KK_2 \geq |w(E)R(\lambda)|$ for $E \geq E_K$ since $w(E)$ is a decreasing function of E . Rewriting (4.59) as

$$R(\lambda) = \frac{K}{\lambda - \lambda_0} + \frac{K_2^2}{\lambda - \lambda_0} \int_{E_0}^{E_K} dE \rho_0(E) \frac{w(E)R(\lambda)(K + w(E)R(\lambda))}{K^2K_2^2 - w(E)^2R(\lambda)^2}, \quad (4.62)$$

we can solve $R(\lambda)$ by using the iteration starting from

$$R(\lambda) = \frac{K}{\lambda - \lambda_0}. \quad (4.63)$$

Plugging this into (4.62) and using (4.60), we obtain

$$\begin{aligned} R(\lambda) &\approx \frac{1}{\lambda - \lambda_0} \left[K_2^2 \int_{E_0}^{E_K} dE \rho_0(E) + \int_{E_0}^{E_K} dE \rho_0(E) \frac{w(E)(\lambda - \lambda_0 + w(E))}{(\lambda - \lambda_0)^2 - \left(\frac{w(E)}{K_2}\right)^2} \right] \\ &= \int_{E_0}^{E_K} dE \rho_0(E) \left[\frac{K_2(K_2 + 1)}{2 \left(\lambda - \lambda_0 - \frac{w(E)}{K_2}\right)} + \frac{K_2(K_2 - 1)}{2 \left(\lambda - \lambda_0 + \frac{w(E)}{K_2}\right)} \right]. \end{aligned} \quad (4.64)$$

Note that this solution is consistent with the large λ behavior of the resolvent $R(\lambda) = K/\lambda + O(\lambda^{-2})$. By taking the discontinuity (3.57), the negativity spectrum is given by

$$D(\lambda) = \int_{E_0}^{E_K} dE \rho_0(E) \left[\frac{K_2(K_2 + 1)}{2} \delta_1(\lambda, E) + \frac{K_2(K_2 - 1)}{2} \delta_2(\lambda, E) \right], \quad (4.65)$$

where we define $\delta_1(\lambda, E)$ and $\delta_2(\lambda, E)$ by

$$\delta_1(\lambda, E) = \delta \left(\lambda - \lambda_0 - \frac{w(E)}{K_2} \right), \quad (4.66)$$

$$\delta_2(\lambda, E) = \delta \left(\lambda - \lambda_0 + \frac{w(E)}{K_2} \right). \quad (4.67)$$

One can check that the negativity spectrum $D(\lambda)$ satisfies the correct normalization conditions

$$\int_{-\infty}^{\infty} d\lambda D(\lambda) = K, \quad \int_{-\infty}^{\infty} d\lambda D(\lambda) \lambda = 1, \quad (4.68)$$

which correspond to $\text{Tr}1 = K$ and $\text{Tr}(\rho^{\text{T}2}) = 1$, respectively. In the next section, we will numerically study the refined Rényi negativity by using the negativity spectrum (4.65).

4.3 Refined Rényi negativity

In this section we study the refined Rényi negativity $S^{\text{T}_2(n)}$ by including the back-reaction of branes. We discuss one of the main results of our study [21]. We consider $S^{\text{T}_2(n)}$ as a function of K_1 with fixed K_2 and g_s . We particularly focus on the parameter regime $\log K_2 < g_s^{-1}$. This regime corresponds to a horizontal line of the phase diagram with $\log K_2 < S_0$ in Figure 4.3. We expect the phase transitions between different saddles labeled by $g = \mathbb{1}, \tau, X$. We find numerically that $S^{\text{T}_2(n)}$ decreases monotonically at late time of the black hole evaporation. It turns out that this decreasing behavior of $S^{\text{T}_2(n)}$ can be proved analytically in the large ξ limit by using the relation (4.70) with the refined Rényi entropy.

Let us study the behavior of $S^{\text{T}_2(n)}$ for $n = 2$ as a typical example. By using (4.47) and (4.48) with (4.65), we can compute the refined Rényi negativity $S^{\text{T}_2(n)}$ numerically. Here we use the deformed eigenvalue density (2.127) to consider the back-reaction of branes. As a comparison, we also compute $S^{\text{T}_2(n)}$ with the original eigenvalue density (2.103) in the probe brane approximation. The results are shown in Figure 4.4. As we can see from Figure 4.4, in the dynamical brane case (orange curve) $S^{\text{T}_2(n)}$ exhibits a monotonically decreasing behavior at late time of the black hole evaporation, while $S^{\text{T}_2(n)}$ approaches a constant value in the probe brane approximation (blue curve).

As advertised above, we can analytically prove the decreasing behavior of $S^{\text{T}_2(n)}$ in the large ξ limit by using the result of section 3.2. To capture the late time behavior, we define the “thermodynamic negativity” by the cyclically connected saddle $g = X$ since it gives a dominant contribution to $S^{\text{T}_2(n)}$ at late time. As shown in Table 4.2, the cyclically connected part of $Z^{\text{T}_2(n)}$ is given by

$$Z^{\text{T}_2(n)}|_{g=X} = \frac{Z_n}{K_2^{n-f(n)}(Z_1)^n}, \quad f(n) \equiv \begin{cases} 1, & n \text{ odd}, \\ 2, & n \text{ even}. \end{cases} \quad (4.69)$$

Thus, by using the definitions (4.10) and (4.11), the thermodynamic negativity is given by

$$S_{\text{thermo}}^{\text{T}_2(n)} = S_{\text{thermo}}^{(n)} + f(n) \log K_2, \quad (4.70)$$

where $S_{\text{thermo}}^{(n)}$ is the “thermodynamic entropy” in (3.82). As analytically

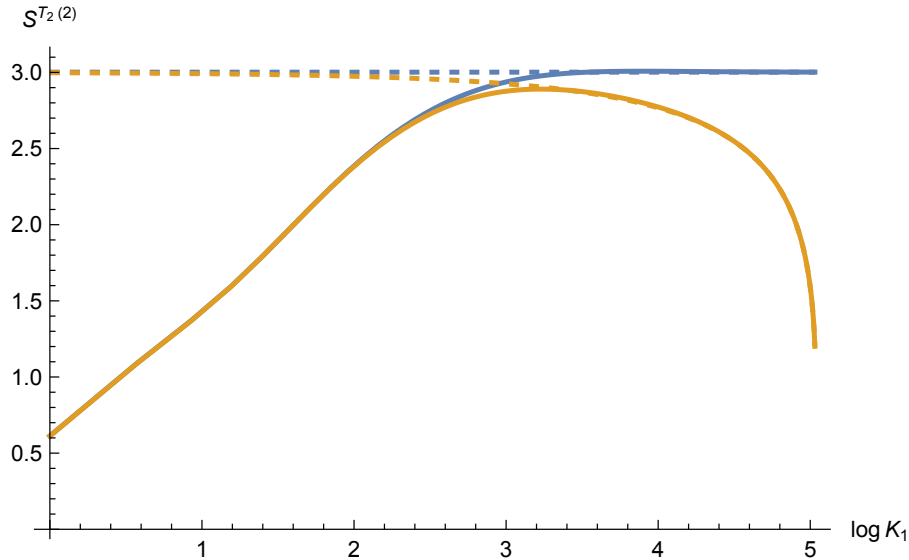


Figure 4.4: Plot of the refined Rényi negativity (4.48) for $n = 2$ as a function of $\log K_1$. The solid orange and blue curves are dynamical and probe brane cases, respectively. We set $\xi = 50, \beta = 4, g_s = 1/50, K_2 = 2$ in this figure. The “thermodynamic negativity” (4.70) for the dynamical and the probe brane cases are represented by the orange and the blue dashed curves, respectively.

proved in section 3.2, $S_{\text{thermo}}^{(n)}$ monotonically decreases as a function of $t = g_s K$ in the large ξ limit. From (4.70), this immediately implies that $S_{\text{thermo}}^{T_2(n)}$ monotonically decreases as a function of K_1 with fixed K_2 and g_s . Thus, we conclude that $S^{T_2(n)}$ monotonically decreases at late time since $S_{\text{thermo}}^{T_2(n)}$ gives the dominant contribution at late time. In Figure 4.4, the thermodynamic negativity $S_{\text{thermo}}^{T_2(n)}$ is plotted by the dashed orange curve, which clearly approaches $S^{T_2(n)}$ (solid orange curve) at late time.

We comment on an interesting observation about (4.70) related to the bulk entanglement wedge cross section [65, 66] which is defined by the minimal cross section of the entanglement wedge in the semiclassical picture.³ As

³In two-dimensional gravities such as JT gravity, the area of the entanglement wedge cross section is not well defined since a constant time-slice of the bulk is one-dimensional and the entanglement wedge cross section becomes a point. In JT gravity, the area of a point is replaced by the value of dilaton at that point.

discussed in [59], a quantity defined by

$$\mathcal{E}_W = S^{\text{T}_2}(\rho_{\text{AB}}) - S_{\text{vN}}(\rho_{\text{AB}}) \quad (4.71)$$

can be identified with the bulk entanglement wedge cross section E_W in the semiclassical limit. Here $S^{\text{T}_2}(\rho_{\text{AB}})$ and $S_{\text{vN}}(\rho_{\text{AB}})$ denote the $n \rightarrow 1$ limit of the refined Rényi negativity and the von Neumann entropy, respectively. It is known that the entanglement wedge cross section E_W and the entanglement entropies S_A, S_B satisfy the following inequalities [65]

$$E_W(\rho_{\text{AB}}) \leq \min\{S_A, S_B\} \leq \log \min\{\dim \mathcal{H}_A, \dim \mathcal{H}_B\}. \quad (4.72)$$

In our case we consider a bipartite radiation system $\mathcal{H}_R = \mathcal{H}_1 \otimes \mathcal{H}_2$. At late time the cyclically connected part of \mathcal{E}_W is dominant and it is given by the $n \rightarrow 1$ limit of (4.70)

$$\mathcal{E}_W|_{g=X} = \lim_{n \rightarrow 1} \left[S_{\text{thermo}}^{\text{T}_2(n)} - S_{\text{thermo}}^{(n)} \right] = \log K_2, \quad (4.73)$$

which saturates the bound in (4.72). This means that the radiation system $\mathcal{H}_R = \mathcal{H}_1 \otimes \mathcal{H}_2$ is maximally entangled at late time. We have obtained this result in a toy model of JT gravity with branes. However, we speculate that this is a general feature of black holes in arbitrary dimensions: Hawking quanta becomes maximally entangled at late time of the evaporation.

As we can see from Figure 4.4, the refined Rényi negativity does not exhibit clear signal of the phase transitions between different saddles labeled by $g = \mathbb{1}, \tau, X$. It turns out that the capacity of negativity is a better indicator of the phase transitions, as we will see in the next section.

4.4 Capacity of negativity

In this section we study the capacity of negativity $C^{\text{T}_2(n)}$ in the microcanonical ensemble. We discuss another main result of our study [21]. We find that the capacity of negativity exhibits two peaks around the phase transitions as a function of K_1 with fixed K_2 .⁴

⁴The capacity of negativity does not exhibit any peaks in the approximation (4.65). Here we instead consider the microcanonical ensemble in which the Schwinger-Dyson equation (4.58) for the resolvent can be solved analytically.

4.4.1 Microcanonical ensemble

To compute the capacity of negativity (4.49), we first review the negativity spectrum $D(\lambda)$ and its phase transitions in the microcanonical ensemble [15]. We focus on some small energy window $[E, E + \Delta E]$ and introduce the microcanonical variables as

$$e^{\mathbf{S}} = \rho(E)\Delta E, \quad \mathbf{Z}_n = \rho(E)A(E)^n \Delta E, \quad \mathbf{w}(E) = \frac{A(E)}{\mathbf{Z}_1} = e^{-\mathbf{S}}. \quad (4.74)$$

This corresponds to consider \mathcal{H}_{BH} with $\dim \mathcal{H}_{\text{BH}} = e^{\mathbf{S}}$. Then the Schwinger-Dyson equation (4.58) reduces to a cubic equation

$$R^3 + \left(\frac{e^{\mathbf{S}} K_2^2 - K}{\lambda} \right) R^2 + e^{2\mathbf{S}} K K_2^2 \left(\frac{1}{\lambda} - K \right) R + \frac{e^{2\mathbf{S}} K^3 K_2^2}{\lambda} = 0. \quad (4.75)$$

This equation can be simplified as

$$zG(z)^3 + (\beta - 1)G(z)^2 + (\alpha - z)G(z) + 1 = 0, \quad (4.76)$$

where we define the rescaled variables,

$$z = K_2 e^{\mathbf{S}} \lambda, \quad G(z) = \frac{e^{-\mathbf{S}} R(\lambda)}{K K_2}, \quad \alpha = \frac{e^{\mathbf{S}}}{K_1}, \quad \beta = \frac{e^{\mathbf{S}} K_2}{K_1}. \quad (4.77)$$

This cubic equation can be solved analytically [67]

$$G(z) = \frac{e^{-i\theta} Q_1(z)}{\left(Q_2(z) + \sqrt{P(z)} \right)^{1/3}} - e^{i\theta} \left(Q_2(z) + \sqrt{P(z)} \right)^{1/3} + \frac{1 - \beta}{3z}, \quad (4.78)$$

where $\theta = \pi/3$ and,

$$Q_1(z) = \frac{3z(\alpha - z) - (\beta - 1)^2}{9z^2}, \quad (4.79)$$

$$Q_2(z) = \frac{9z(\beta - 1)(\alpha - z) - 27z^2 - 2(\beta - 1)^3}{54z^3}, \quad (4.80)$$

$$P(z) = Q_1(z)^3 + Q_2(z)^2. \quad (4.81)$$

From the solution of $G(z)$ in (4.78), we can compute the negativity spectrum $D(\lambda)$ by taking the discontinuity of $G(z)$ as in (3.57). In what follows, we will consider $D(\lambda)$ as a function of K_1 with fixed K_2 and \mathbf{S} . As we vary

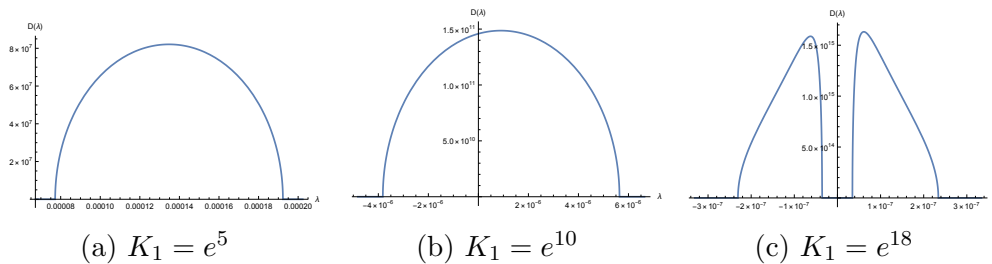


Figure 4.5: Plot of the negativity spectrum obtained from the discontinuity of $G(z)$ in (4.78). Here we set the parameters $\mathbf{S} = 12, K_2 = 50$. (a), (b), (c) correspond to the dominant saddles $g = \mathbb{1}, \tau, X$, respectively.

K_1 , there appear three phases for $D(\lambda)$ corresponding to three saddles labeled by $g = \mathbb{1}, \tau, X$ [15]. Let us take a closer look at the behavior of $D(\lambda)$ in each phase. As shown in Figure 4.5a, when the saddle labeled by $g = \mathbb{1}$ is dominant, $D(\lambda)$ has a support on the positive λ axis. In the phase where the $g = \tau$ saddle is dominant (see Figure 4.5b), $D(\lambda)$ has a support on the negative λ axis as well. This means that the partially transposed density matrix $\rho^{\text{T}2}$ has negative eigenvalues and the two systems \mathcal{H}_1 and \mathcal{H}_2 become entangled. If we further increase K_1 , we land on the phase where the $g = X$ saddle is dominant (see Figure 4.5c). In this case, the support of $D(\lambda)$ is a disjoint union of a negative λ region and a positive λ region.

Now let us consider the conditions to determine the support of $D(\lambda)$ and its phase transition points. The negativity spectrum $D(\lambda)$ behaves as a fractional power in λ near the edges of the support and hence its derivative diverges there. Thus, we can determine the edges of the support of $D(\lambda)$ from singularities of $dR/d\lambda$, since $D(\lambda)$ is obtained from the discontinuity (3.57) of $R(\lambda)$. From (4.78), we find the support of $D(\lambda)$ is determined by the condition $P(z) \geq 0$, and the zeros of $P(z)$ correspond to the edges of $D(\lambda)$. To find the transition points, it is convenient to define the polynomial part of $P(z)$ by $f(z) = z^4 P(z)$. The transition between $g = \mathbb{1}$ and $g = \tau$ occurs when the left edge of the support of $D(\lambda)$ approaches $\lambda = 0$. This condition is given by $f(0) = 0$, from which K_1 is determined as

$$K_1 = \frac{e^{\mathbf{S}} \left(K_2 - \sqrt{K_2^2 - 1} \right)}{2}. \quad (4.82)$$

The transition between $g = \tau$ and $g = X$ corresponds to a point where the

support of $D(\lambda)$ starts to split into two disjoint regions. This is determined by the condition that $f(z)$ has a double root. In other words, the discriminant of $f(z)$ becomes zero at this transition point. From the discriminant of $f(z)$, we find that the critical value of K_1 is determined by the following cubic equation

$$64K_1^3 - 48e^{\mathbf{S}}K_2K_1^2 - (15K_2^2 - 27)e^{2\mathbf{S}}K_1 - e^{3\mathbf{S}}K_2^2 = 0. \quad (4.83)$$

In the next subsection, we compute the capacity of negativity and show that it exhibits two peaks around these transition points.

4.4.2 Capacity of negativity

Let us consider the capacity of negativity $C^{\text{T}_2(n)}$ in the microcanonical ensemble using the result of $D(\lambda)$ in the previous subsection. First we evaluate $C^{\text{T}_2(n)}$ in each dominant saddle. From the definition of $C^{\text{T}_2(n)}$ in the third column of Table 4.1, one can show that $C^{\text{T}_2(n)}$ is written as

$$C^{\text{T}_2(n)} = n^2 \partial_n^2 \log Z^{\text{T}_2(n)}. \quad (4.84)$$

This is valid for both even and odd n . In each phase, we can replace $Z^{\text{T}_2(n)}$ by each saddle-point value summarized in Table 4.2. In general, the saddle-point values of $Z^{\text{T}_2(n)}$ in Table 4.2 take the form

$$Z^{\text{T}_2(n)} = a(n)b^{n+c}, \quad (4.85)$$

where b and c are n -independent constants. Plugging (4.85) into (4.84), we find

$$C^{\text{T}_2(n)} = n^2 \partial_n^2 \log a(n). \quad (4.86)$$

Namely, b and c in (4.85) do not contribute to $C^{\text{T}_2(n)}$.

From the first column of Table 4.2, $Z^{\text{T}_2(n)} = 1/K^{n-1}$ for the disconnected saddle $g = \mathbb{1}$, which implies that $C^{\text{T}_2(n)}$ vanishes when the disconnected saddle $g = \mathbb{1}$ is dominant. From the second column of Table 4.2, $C^{\text{T}_2(n)}$ for the pairwise connected saddle $g = \tau$ is given by

$$C^{\text{T}_2(n,\text{even})} = \frac{n^2}{4} \left[\psi^{(1)} \left(\frac{n+1}{2} \right) - \psi^{(1)} \left(\frac{n}{2} + 2 \right) \right], \quad (4.87)$$

$$C^{\text{T}_2(n,\text{odd})} = -1 + \frac{n^2}{4} \left[\psi^{(1)} \left(\frac{n}{2} \right) - \psi^{(1)} \left(\frac{n+3}{2} \right) \right], \quad (4.88)$$

where $\psi^{(m)}(z)$ is the polygamma function of order m , which comes from the derivative of the Catalan number C_m or C_{m-1} . The first term -1 in (4.88) comes from the derivatives of the factor $(2m-1)$ in $Z^{\text{T}_2(2m-1, \text{odd})}$. Interestingly, the values of $C^{\text{T}_2(n)}$ in (4.87) and (4.88) depend only on the replica number n and they are independent of the other parameters K_1 , K_2 and \mathbf{S} . This property comes from the fact that the parameter dependence is contained in the factor b^{n+c} in (4.85) which does not contribute to $C^{\text{T}_2(n)}$ as we saw in (4.86). From the third column of Table 4.2, $C^{\text{T}_2(n)}$ for the cyclically connected saddle $g = X$ is given by

$$C^{\text{T}_2(n)} = n^2 \partial_n^2 \log Z_n. \quad (4.89)$$

In the microcanonical ensemble, $C^{\text{T}_2(n)}$ in (4.89) vanishes since Z_n in (4.74) takes the form of b^{n+c} . Thus, the capacity of negativity takes a nontrivial values only in the phase where the saddle $g = \tau$ is dominant.

Now let us compute the capacity of negativity $C^{\text{T}_2(n)}$ in the microcanonical ensemble using the definitions in (4.47), (4.48) and (4.49) with the negativity spectrum calculated by the discontinuity of $G(z)$ in (4.78). In Figure 4.6 we show the plot of $C^{\text{T}_2(n)}$ for $n = 1$ as a function of K_1 with fixed K_2 and \mathbf{S} . As we see from Figure 4.6, the capacity of negativity (blue curve) exhibits two peaks around the transition points determined by the conditions (4.82) and (4.83) (dashed vertical lines). Between the two peaks, $C^{\text{T}_2(n)}$ approaches a saddle-point value for $g = \tau$ (dashed orange line) given by (4.88). The locations of peaks do not exactly match the transition points of $D(\lambda)$ determined by the conditions (4.82) and (4.83) since the capacity of negativity $C^{\text{T}_2(n)}$ is an integrated function of $D(\lambda)$. However, we have checked that (4.82) and (4.83) give a qualitatively good approximation of the locations of peaks for various values of K_2 , \mathbf{S} and n . From Figure 4.6, we also observe that $C^{\text{T}_2(n)}$ approaches zero in the small and large K_1 limits. This is consistent with the fact that the saddle-point values of $C^{\text{T}_2(n)}$ vanish for $g = \mathbb{1}$ and $g = X$.

Near the transition points, the saddle-point approximation breaks down and we cannot ignore the sub-leading corrections in (4.43) coming from the general elements g in the permutation group S_n other than the dominant saddles $g = \mathbb{1}, \tau, X$. This is the physical origin of the peaks of $C^{\text{T}_2(n)}$ we observed in Figure 4.6. This is in contrast to the behavior of the refined Rényi negativity $S^{\text{T}_2(n)}$ (see Figure 4.4) which does not exhibit a clear signal of the

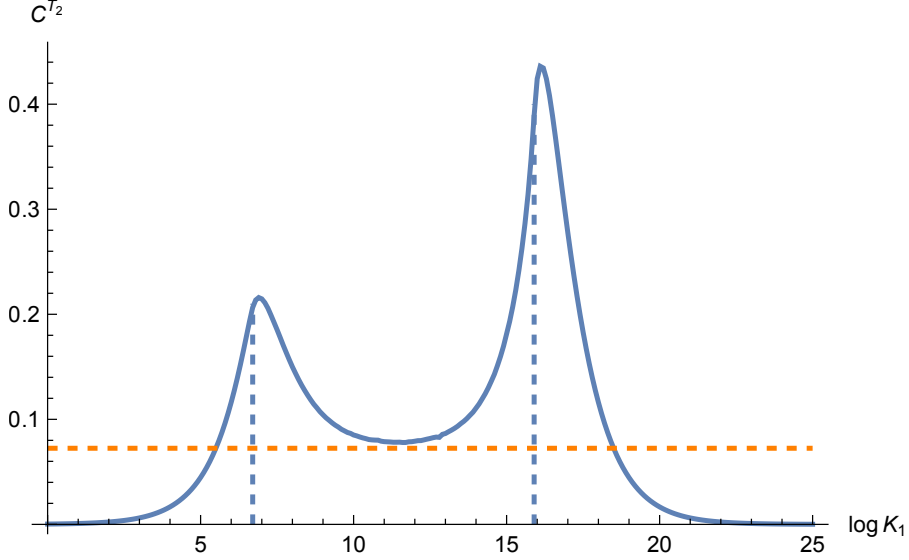


Figure 4.6: Plot of the capacity of negativity (4.49) for $n = 1$ as a function of $\log K_1$. We set $K_2 = 50$, $\mathcal{S} = 12$ in this figure. The two vertical dashed blue lines are the transition points determined by (4.82) and (4.83). The horizontal dashed orange line is the value of (4.88) at $n = 1$.

phase transitions. In $C^{\text{T}_2(n)}$ the phase transitions manifest itself as two peaks, which suggests that $C^{\text{T}_2(n)}$ is a better indicator of the phase transitions than $S^{\text{T}_2(n)}$. Indeed, in many physical systems it is useful to consider the susceptibility defined by a second derivative of the free energy with respect to an external field in order to search for possible phase transitions. In our case, the capacity of negativity $C^{\text{T}_2(n)}$ plays the role of the susceptibility of entanglement in the bipartite system $\mathcal{H}_1 \otimes \mathcal{H}_2$. In fact, $C^{\text{T}_2(n)}$ in (4.84) represents the variance of the partially transposed modular Hamiltonian $H^{\text{T}_2} = -\log \rho^{\text{T}_2}$

$$\begin{aligned} \frac{1}{n^2} C^{\text{T}_2(n)} &= \langle (H^{\text{T}_2})^2 \rangle_n - \langle H^{\text{T}_2} \rangle_n^2 \\ &= \langle (H^{\text{T}_2} - \langle H^{\text{T}_2} \rangle_n)^2 \rangle_n, \end{aligned} \quad (4.90)$$

where $\langle \mathcal{O} \rangle_n$ is defined by

$$\langle \mathcal{O} \rangle_n = \frac{\text{Tr}(\mathcal{O} e^{-nH^{\text{T}_2}})}{\text{Tr}(e^{-nH^{\text{T}_2})}. \quad (4.91)$$

Near the phase transition the fluctuation of H^{T_2} becomes large, which is observed as the peak of $C^{\text{T}_2(n)}$.

Chapter 5

Discussion

In this chapter, we summarize our results and discuss open questions. We studied the refined Rényi negativity and the capacity of negativity in JT gravity with dynamical FZZT anti-branes, which serves as a toy model of an evaporating black hole. The new original results are summarized by the plots in Figure 4.4 and Figure 4.6.

First, we considered the refined Rényi negativity with dynamical FZZT anti-branes. The deformation of the eigenvalue density of JT gravity by the branes played the essential role in the computation. As seen from Figure 4.4, we find that the refined Rényi negativity monotonically decreases at late time of the evaporation due to the back-reaction of branes, while it approaches a constant value in the probe brane approximation. We can easily understand the decreasing behavior by using the relation (4.70) between the totally connected part of the refined Rényi negativity and the refined Rényi entropy. The $n \rightarrow 1$ limit of the refined Rényi negativity is related to the bulk entanglement wedge cross section in the semiclassical picture, which saturates the inequality (4.72) at late time of the evaporation. This means that the Hawking quanta become maximally entangled at late time of the black hole evaporation.

Next, we considered the capacity of negativity in the microcanonical ensemble, in which the Schwinger-Dyson equation can be exactly solved. As seen from Figure 4.6, we find that the capacity of negativity exhibits two peaks around the phase transitions, reflecting the fact that the entanglement negativity can probe more elaborate entanglement structure than the entanglement entropy. Moreover, in the pairwise connected phase which arises

in-between the two peaks, the capacity of negativity approaches a universal constant value which only depends on the replica number. We conclude that the capacity of negativity is an valuable indicator of the phase transitions among the different entanglement phases in general mixed states.

Open questions

There are many interesting open questions. We studied the refined Rényi negativity and the capacity of negativity in the planar approximation. However, near the end of the evaporation the black hole becomes very small and we cannot ignore the quantum corrections. It would be interesting to study the higher genus corrections to the entanglement negativities in JT gravity. To this end we need to develop a method of computing the non-planar corrections to the resolvent of ρ^{T^2} . Moreover, it would be very interesting to compute the entanglement negativities non-perturbatively in g_s .

It would be interesting to study the capacity of negativity in the canonical ensemble. We expect that the qualitative feature will also hold in the canonical ensemble: the capacity of negativity exhibits two peaks around the phase transitions. The main difference between the microcanonical and canonical ensembles is the late time behavior (4.70). One of the advantages of the canonical ensemble is that we can study the quantities using the density of states in JT gravity with the effect of the backreaction of branes.

Actually we tried to compute the capacity of negativity in the canonical ensemble. However, it does not exhibit any peaks around the phase transitions by using the negativity spectrum (4.65). On the other hand, there is a trick to find a peak of the capacity of entanglement in the canonical ensemble [62]. Namely, we need to determine the minimal eigenvalue λ_0 of the entanglement spectrum by solving the derivative of the Schwinger-Dyson equation $d\lambda/dR = 0$ numerically. We studied the capacity of negativity in a similar manner. However, it was difficult to find a solution of $d\lambda/dR = 0$ because the Schwinger-Dyson equation for the negativity resolvent is more complicated than that of the entanglement entropy. We leave the computation of the capacity of negativity in the canonical ensemble as an interesting future problem.

We introduced the capacity of negativity as a natural analogue of the capacity of entanglement. The authors of [61] studied the capacity of entan-

glement in a two-dimensional dilaton gravity coupled to conformal matter with a large central charge. This is a useful model where the island formula [9, 10, 11] for the entanglement entropy of the Hawking radiation was explicitly tested for the first time. Also, the island contributions to the entanglement negativity was studied in [68]. It would be interesting to consider the capacity of negativity in such a model and to study the contributions of the island along the line of these studies.

It is also interesting to consider the holographic dual of the capacity of negativity. As discussed in [69, 70], the holographic dual of the capacity of entanglement is described by the graviton fluctuation around the minimal surface associated with holographic refined Rényi entropy. As we mentioned in section 4.3, the refined Rényi negativity is related to the bulk entanglement wedge cross section which is the minimal cross section of the entanglement wedge in the semiclassical picture. We speculate that the holographic dual of the capacity of negativity is described by the graviton fluctuation around the entanglement wedge cross section. Furthermore, the entanglement wedge cross section is also related to the reflected entropy [71]. It would be interesting to consider “refined Rényi reflected entropy” and its capacity. We expect that we can extract more detailed information about the entanglement structure by using these generalization of quantum information quantities.

Bibliography

- [1] A. Almheiri, T. Hartman, J. Maldacena, E. Shaghoulian, and A. Tajdini, “The entropy of Hawking radiation,” *Rev. Mod. Phys.* **93** (2021) 035002, [arXiv:2006.06872 \[hep-th\]](#).
- [2] J. R. Oppenheimer and H. Snyder, “On Continued gravitational contraction,” *Phys. Rev.* **56** (1939) 455–459.
- [3] S. W. Hawking, “Black holes in general relativity,” *Commun. Math. Phys.* **25** (1972) 152–166.
- [4] S. W. Hawking, “Particle Creation by Black Holes,” *Commun. Math. Phys.* **43** (1975) 199–220. [Erratum: *Commun.Math.Phys.* 46, 206 (1976)].
- [5] S. W. Hawking, “Breakdown of Predictability in Gravitational Collapse,” *Phys. Rev. D* **14** (1976) 2460–2473.
- [6] D. N. Page, “Average entropy of a subsystem,” *Phys. Rev. Lett.* **71** (1993) 1291–1294, [arXiv:gr-qc/9305007](#).
- [7] D. N. Page, “Information in black hole radiation,” *Phys. Rev. Lett.* **71** (1993) 3743–3746, [arXiv:hep-th/9306083](#).
- [8] J. D. Bekenstein, “Black holes and entropy,” *Phys. Rev. D* **7** (1973) 2333–2346.
- [9] G. Penington, “Entanglement Wedge Reconstruction and the Information Paradox,” *JHEP* **09** (2020) 002, [arXiv:1905.08255 \[hep-th\]](#).

- [10] A. Almheiri, N. Engelhardt, D. Marolf, and H. Maxfield, “The entropy of bulk quantum fields and the entanglement wedge of an evaporating black hole,” *JHEP* **12** (2019) 063, [arXiv:1905.08762 \[hep-th\]](#).
- [11] A. Almheiri, R. Mahajan, J. Maldacena, and Y. Zhao, “The Page curve of Hawking radiation from semiclassical geometry,” *JHEP* **03** (2020) 149, [arXiv:1908.10996 \[hep-th\]](#).
- [12] A. Lewkowycz and J. Maldacena, “Generalized gravitational entropy,” *JHEP* **08** (2013) 090, [arXiv:1304.4926 \[hep-th\]](#).
- [13] A. Almheiri, T. Hartman, J. Maldacena, E. Shaghoulian, and A. Tajdini, “Replica Wormholes and the Entropy of Hawking Radiation,” *JHEP* **05** (2020) 013, [arXiv:1911.12333 \[hep-th\]](#).
- [14] G. Penington, S. H. Shenker, D. Stanford, and Z. Yang, “Replica wormholes and the black hole interior,” *JHEP* **03** (2022) 205, [arXiv:1911.11977 \[hep-th\]](#).
- [15] X. Dong, S. McBride, and W. W. Weng, “Replica wormholes and holographic entanglement negativity,” *JHEP* **06** (2022) 094, [arXiv:2110.11947 \[hep-th\]](#).
- [16] P. Saad, S. H. Shenker, and D. Stanford, “JT gravity as a matrix integral,” [arXiv:1903.11115 \[hep-th\]](#).
- [17] K. Okuyama and K. Sakai, “FZZT branes in JT gravity and topological gravity,” *JHEP* **09** (2021) 191, [arXiv:2108.03876 \[hep-th\]](#).
- [18] V. Fateev, A. B. Zamolodchikov, and A. B. Zamolodchikov, “Boundary Liouville field theory. 1. Boundary state and boundary two point function,” [arXiv:hep-th/0001012](#).
- [19] J. Teschner, “Remarks on Liouville theory with boundary,” *PoS tnr2000* (2000) 041, [arXiv:hep-th/0009138](#).
- [20] K. Okuyama and K. Sakai, “Page curve from dynamical branes in JT gravity,” *JHEP* **02** (2022) 087, [arXiv:2111.09551 \[hep-th\]](#).

- [21] K. Okuyama and T. Tachibana, “Negativity and its capacity in JT gravity,” *JHEP* **02** (2024) 183, [arXiv:2312.11860 \[hep-th\]](#).
- [22] T. G. Mertens and G. J. Turiaci, “Solvable models of quantum black holes: a review on Jackiw–Teitelboim gravity,” *Living Rev. Rel.* **26** (2023) 4, [arXiv:2210.10846 \[hep-th\]](#).
- [23] C. Teitelboim, “Gravitation and Hamiltonian Structure in Two Space-Time Dimensions,” *Phys. Lett. B* **126** (1983) 41–45.
- [24] R. Jackiw, “Lower Dimensional Gravity,” *Nucl. Phys. B* **252** (1985) 343–356.
- [25] A. Almheiri and J. Polchinski, “Models of AdS₂ backreaction and holography,” *JHEP* **11** (2015) 014, [arXiv:1402.6334 \[hep-th\]](#).
- [26] G. W. Gibbons and S. W. Hawking, “Action Integrals and Partition Functions in Quantum Gravity,” *Phys. Rev. D* **15** (1977) 2752–2756.
- [27] J. W. York, Jr., “Role of conformal three geometry in the dynamics of gravitation,” *Phys. Rev. Lett.* **28** (1972) 1082–1085.
- [28] J. Maldacena, D. Stanford, and Z. Yang, “Conformal symmetry and its breaking in two dimensional Nearly Anti-de-Sitter space,” *PTEP* **2016** (2016) 12C104, [arXiv:1606.01857 \[hep-th\]](#).
- [29] M. Mirzakhani, “Simple geodesics and Weil-Petersson volumes of moduli spaces of bordered Riemann surfaces,” *Invent. Math.* **167** (2006) 179–222.
- [30] K. Okuyama and K. Sakai, “JT gravity, KdV equations and macroscopic loop operators,” *JHEP* **01** (2020) 156, [arXiv:1911.01659 \[hep-th\]](#).
- [31] P. Zograf, “On the large genus asymptotics of Weil-Petersson volumes,” [arXiv:0812.0544 \[math.AG\]](#).
- [32] J. Wishart, “The Generalised Product Moment Distribution in Samples from a Normal Multivariate Population,” *Biometrika* **20A** (1928) 32–52.

- [33] E. P. Wigner, “On the statistical distribution of the widths and spacings of nuclear resonance levels,” *Mathematical Proceedings of the Cambridge Philosophical Society* **47** (1951) 790–798.
- [34] P. H. Ginsparg and G. W. Moore, “Lectures on 2-D gravity and 2-D string theory,” in *Theoretical Advanced Study Institute (TASI 92): From Black Holes and Strings to Particles*, pp. 277–469. 10, 1993. [arXiv:hep-th/9304011](#).
- [35] P. Di Francesco, P. H. Ginsparg, and J. Zinn-Justin, “2-D Gravity and random matrices,” *Phys. Rept.* **254** (1995) 1–133, [arXiv:hep-th/9306153](#).
- [36] B. Eynard, T. Kimura, and S. Ribault, “Random matrices,” [arXiv:1510.04430 \[math-ph\]](#).
- [37] B. Eynard, “Topological expansion for the 1-Hermitian matrix model correlation functions,” *JHEP* **11** (2004) 031, [arXiv:hep-th/0407261](#).
- [38] B. Eynard and N. Orantin, “Invariants of algebraic curves and topological expansion,” *Commun. Num. Theor. Phys.* **1** (2007) 347–452, [arXiv:math-ph/0702045](#).
- [39] B. Eynard and N. Orantin, “Weil-Petersson volume of moduli spaces, Mirzakhani’s recursion and matrix models,” [arXiv:0705.3600 \[math-ph\]](#).
- [40] G. ’t Hooft, “A Planar Diagram Theory for Strong Interactions,” *Nucl. Phys. B* **72** (1974) 461.
- [41] E. Witten, “Two-dimensional gravity and intersection theory on moduli space,” *Surveys Diff. Geom.* **1** (1991) 243–310.
- [42] M. Kontsevich, “Intersection theory on the moduli space of curves and the matrix Airy function,” *Commun. Math. Phys.* **147** (1992) 1–23.
- [43] R. Dijkgraaf and E. Witten, “Developments in Topological Gravity,” *Int. J. Mod. Phys. A* **33** (2018) 1830029, [arXiv:1804.03275 \[hep-th\]](#).

- [44] M. Mulase and B. Safnuk, “Mirzakhani’s recursion relations, Virasoro constraints and the KdV hierarchy,” [arXiv:math/0601194](#).
- [45] K. Okuyama and K. Sakai, “Multi-boundary correlators in JT gravity,” *JHEP* **08** (2020) 126, [arXiv:2004.07555 \[hep-th\]](#).
- [46] I. M. Gelfand and L. A. Dikii, “Asymptotic behavior of the resolvent of Sturm-Liouville equations and the algebra of the Korteweg-De Vries equations,” *Russ. Math. Surveys* **30** (1975) 77–113.
- [47] C. Itzykson and J. B. Zuber, “Combinatorics of the modular group. 2. The Kontsevich integrals,” *Int. J. Mod. Phys. A* **7** (1992) 5661–5705, [arXiv:hep-th/9201001](#).
- [48] A. Goel, L. V. Iliesiu, J. Kruthoff, and Z. Yang, “Classifying boundary conditions in JT gravity: from energy-branes to α -branes,” *JHEP* **04** (2021) 069, [arXiv:2010.12592 \[hep-th\]](#).
- [49] P. Gao, D. L. Jafferis, and D. K. Kolchmeyer, “An effective matrix model for dynamical end of the world branes in Jackiw-Teitelboim gravity,” *JHEP* **01** (2022) 038, [arXiv:2104.01184 \[hep-th\]](#).
- [50] A. Rényi, “On measures of entropy and information,” in Proceedings of the fourth Berkeley symposium on mathematical statistics and probability, volume 1: contributions to the theory of statistics, vol. 4, pp. 547–562, University of California Press. 1961.
- [51] A. Rényi, “On the foundations of information theory,” *Revue de l’Institut International de Statistique* (1965) 1–14.
- [52] X. Dong, “The Gravity Dual of Renyi Entropy,” *Nature Commun.* **7** (2016) 12472, [arXiv:1601.06788 \[hep-th\]](#).
- [53] H. Yao and X.-L. Qi, “Entanglement entropy and entanglement spectrum of the Kitaev model,” *Phys. Rev. Lett.* **105** (2010) 080501, [arXiv:1001.1165 \[cond-mat.str-el\]](#).
- [54] S. Sugiura and A. Shimizu, “Canonical Thermal Pure Quantum State,” *Phys. Rev. Lett.* **111** (2013) 010401, [arXiv:1302.3138 \[cond-mat.stat-mech\]](#).

- [55] K. Goto, Y. Kusuki, K. Tamaoka, and T. Ugajin, “Product of random states and spatial (half-)wormholes,” *JHEP* **10** (2021) 205, [arXiv:2108.08308 \[hep-th\]](#).
- [56] G. Vidal and R. F. Werner, “Computable measure of entanglement,” *Phys. Rev. A* **65** (2002) 032314, [arXiv:quant-ph/0102117](#).
- [57] A. Peres, “Separability criterion for density matrices,” *Phys. Rev. Lett.* **77** (1996) 1413–1415, [arXiv:quant-ph/9604005](#).
- [58] M. Horodecki, P. Horodecki, and R. Horodecki, “On the necessary and sufficient conditions for separability of mixed quantum states,” *Phys. Lett. A* **223** (1996) 1, [arXiv:quant-ph/9605038](#).
- [59] K. Tamaoka, “Entanglement Wedge Cross Section from the Dual Density Matrix,” *Phys. Rev. Lett.* **122** (2019) 141601, [arXiv:1809.09109 \[hep-th\]](#).
- [60] X. Dong, X.-L. Qi, and M. Walter, “Holographic entanglement negativity and replica symmetry breaking,” *JHEP* **06** (2021) 024, [arXiv:2101.11029 \[hep-th\]](#).
- [61] K. Kawabata, T. Nishioka, Y. Okuyama, and K. Watanabe, “Replica wormholes and capacity of entanglement,” *JHEP* **10** (2021) 227, [arXiv:2105.08396 \[hep-th\]](#).
- [62] K. Kawabata, T. Nishioka, Y. Okuyama, and K. Watanabe, “Probing Hawking radiation through capacity of entanglement,” *JHEP* **05** (2021) 062, [arXiv:2102.02425 \[hep-th\]](#).
- [63] K. Okuyama, “Capacity of entanglement in random pure state,” *Phys. Lett. B* **820** (2021) 136600, [arXiv:2103.08909 \[hep-th\]](#).
- [64] A. Nica and R. Speicher, *Lectures on the Combinatorics of Free Probability*. London Mathematical Society Lecture Note Series. Cambridge University Press, 2006.
- [65] T. Takayanagi and K. Umemoto, “Entanglement of purification through holographic duality,” *Nature Phys.* **14** (2018) 573–577, [arXiv:1708.09393 \[hep-th\]](#).

- [66] P. Nguyen, T. Devakul, M. G. Halbasch, M. P. Zaletel, and B. Swingle, “Entanglement of purification: from spin chains to holography,” *JHEP* **01** (2018) 098, [arXiv:1709.07424 \[hep-th\]](#).
- [67] H. Shapourian, S. Liu, J. Kudler-Flam, and A. Vishwanath, “Entanglement Negativity Spectrum of Random Mixed States: A Diagrammatic Approach,” *PRXQuantum* **2** (2021) 030347, [arXiv:2011.01277 \[cond-mat.str-el\]](#).
- [68] J. Kumar Basak, D. Basu, V. Malvimat, H. Parihar, and G. Sengupta, “Islands for entanglement negativity,” *SciPost Phys.* **12** (2022) 003, [arXiv:2012.03983 \[hep-th\]](#).
- [69] Y. Nakaguchi and T. Nishioka, “A holographic proof of Rényi entropic inequalities,” *JHEP* **12** (2016) 129, [arXiv:1606.08443 \[hep-th\]](#).
- [70] J. De Boer, J. Järvelä, and E. Keski-Vakkuri, “Aspects of capacity of entanglement,” *Phys. Rev. D* **99** (2019) 066012, [arXiv:1807.07357 \[hep-th\]](#).
- [71] C. Akers, T. Faulkner, S. Lin, and P. Rath, “The Page curve for reflected entropy,” *JHEP* **06** (2022) 089, [arXiv:2201.11730 \[hep-th\]](#).